TECHNISCHE UNIVERSITÄT WIEN

Reviewed by

_____ _____ _____
B. Lendl   C. Huck   G. Friedbacher

Near- and Far-Field Mid-Infrared Spectroscopy and Spectroscopic Imaging for Biomedical Applications

A thesis submitted for the degree of
Doctor of Technical Sciences
at
Technische Universität Wien
Faculty of Technical Chemistry
Institute of Chemical Technologies and Analytics

under supervision of
Univ. Prof. Dr. Bernhard Lendl

defended by
Anna Balbekova

Mat.Nr.1329826
Laxenburger Strasse 59, 12, A-1100 Vienna

_____   _____
Place and Date   Anna Balbekova

Abstract

Mid-Infrared (IR) spectroscopy allows for non-destructive and label free analysis providing molecular specific information. This technique can thus be successfully applied in microbiological and biomedical research. IR spectroscopic imaging is an advantageous complimentary tool to established histological analysis. However, IR spectroscopy has certain limitations: the spatial resolution of IR microscopic imaging cannot be better than a few micrometers due to the diffraction limit in far-field microscopy and IR spectroscopy cannot provide information on an elemental level.

The first limitation can be solved through the application of recently developed near-field imaging techniques such as phothermal induced resonance (PTIR). The second limitation can be overcome when an additional technique complementary to IR spectroscopy is used too and the combined data-sets are jointly analysed.

The first experimental part of this thesis is devoted to the characterization of a custom made PTIR system and its application to the measurements of various biological samples. The second experimental part is devoted to the combined image analysis of histological samples using commercially available techniques such as Fourier transform Infrared (FTIR) spectroscopy and laser ablation inductively coupled mass spectrometry (LA-ICP-MS).

In the first part of the work time-resolved PTIR spectroscopic measurements are reported for the first time on the example of a biopolymer (poly-L-lysine, PLL) 200 nm thick film. PLL films can adopt different secondary structures depending on its water content, which can be adjusted through temperature in an atmosphere of controlled humidity. A controlled temperature ramp of the sample caused changes in the amide I band of the PLL. Those changes were detected using PTIR time resolved measurements. The achieved acquisition time of one PTIR spectrum is 15 s. Control analysis using a commercial FTIR microscope corroborated the spectroscopic results.

Further, the PTIR performance was characterized regarding AFM tip aging during prolonged measurements of the polymer polystyrene (PS) and biological samples (cells and tissues). It was shown, that after the prolonged measurements of PS have no notable affect on the PTIR performance. However, a notable decrease in PTIR sensitivity was observed after several measurements of biological samples. A method for in-situ controlling aging if the AFM tip was proposed. The AFM tip aging was judged by following the signal intensity of a band δ_s(Si-CH$_3$) associated with stable impurities of the gold coated tip. The proposed method was successfully employed during the measurements of biological samples (cells and tissues).

PTIR spectroscopic and imaging measurements of individual *E. Coli* bacteria consisting of aggregated proteins (horseradish peroxidase) as inclusion bodies (IBs) were performed. The average secondary structure of the IBs found to be different from the host bacteria. A method for the quantitative analysis of the present IBs was proposed.

PTIR and FTIR spectra of dead (apoptotic) and viable regions in a histological tumor section were acquired and analysed. The results of the near-field analysis agree with the far-field micro-spectroscopic measurements. In particular, changes in protein secondary structure

and nonlinear properties in the absorption of IR radiation by condensed nucleic acids were observed.

Further using the PTIR technique individual dead (apoptotic) and viable mammalian cells were characterized. Two types of apoptotic cells were discriminated. For some cells protein secondary structure at nuclei and cytoplasm regions appeared to be different. Other cells had no notable differences in the overall protein conformation. In both kinds of apoptotic cells the decay of the band related to nucleic acids (C-N-C stretch of ribose-phosphate skeletal vibrations in nucleic acids) was observed. Viable (control) cells demonstrated no significant alterations in the overall protein secondary structure at nuclei and cytoplasm regions. Additionally, the overall protein conformation in nuclei region for apoptotic and control cells were found to be different.

In the second part of the work combined image analysis for discrimination and characterization of biological tissues (tumor and ischemic brain) was performed. Combined analysis of the tumor demonstrated statistical correlations between elemental and molecular chemical maps. Additionally, the combination of data from the two techniques (FTIR and LA-ICP-MS) facilitated an improved cluster analysis and allowed discrimination of different stages of apoptosis within a tumor tissue. Besides, the combined (multi-sensor) analysis helped to characterize different degrees of cellular death within different tumor samples.

During the multi-sensor analysis of thin cuts of ischemic rat brain partial least squares discriminant analysis (PLS-DA) and random decision forest (RDF) classification algorithms were applied and their performance was compared. As a result, different tissue types were distinguished. The performance of classification models built on the combined dataset was compared with the classification results based on the individual datasets. Multi-sensor analysis again improved classification. Here different tissue types such as white and gray matter, as well as stroke region and its surroundings could be differentiated more efficiently. Furthermore RDF classification appeared to me more precise than PLS-DA.

The results, presented in this thesis demonstrate the capabilities and advances of near- and far-field IR spectroscopy and spectroscopic imaging applied to analysis of biological samples. Further, the results demonstrate that the multi-sensor combined analysis incorporating FTIR and LA-ICP-MS imaging facilitates an improved multivariate analysis and thus deeper understanding of biochemical processes.

Kurzfassung

Die Spektroskopie im mittleren Infrarot (IR) ist eine markierungs- und zerstörungsfreie Technik um molekülspezifische Information zu erhalten. Diese Technik kann auch in der mikrobiologischen und biomedizinischen Forschung angewendet werden. Insbesondere im Bereich der bildgebenden Analyse mittels IR Mikroskopie können zur klassischen histologischen Untersuchung komplementäre sowie ergänzende Informationen gewonnen werden. Allerdings weist die IR Mikrospektroskopie eigene Limitierungen auf: erstens kann bei Verwendung von klassischen Fernfeldmikroskopie Systemen die räumliche Auflösung nicht besser als einige Mikrometer sein, zweitens kann die IR Spektroskopie keine Information bezüglich der Elementzusammensetzung der Probe liefern.

Die erste Beschränkung kann durch die Anwendung einer neuen, im Nahfeld arbeitenden, bildgebenden Methode basierend auf der photothermisch induzierten Resonanz (PTIR) gelöst werden. Die zweite Beschränkung kann durch Anwendung einer zweiten, komplementären, Messtechnik und anschließender gemeinsamer Analyse der vereinten Datensätze aufgehoben werden.

Der erste experimentelle Teil dieser Dissertation beschreibt die Charakterisierung eines selbstgebauten PTIR Systems und dessen Anwendung zur Analyse von verschiedenen biologischen Proben. Die Arbeit beinhaltet die weltweit erste zeitaufgelöste PTIR Untersuchung am Beispiel einer induzierten Sekundärstrukturänderung einer 200 nm dünnen Schicht aus poly-L-lysine (PLL). PLL liegt in Abhängigkeit seines Wassergehaltes in verschiedenen Sekundärstrukturen vor. Der Wassergehalt des PLL Films und somit dessen angenommene Sekundärstruktur kann bei konstanter Luftfeuchtigkeit über die Temperatur eingestellt werden. Ein kontrollierter Temperaturanstieg der Probe führt somit zu Änderungen in der Amide I Bande von PLL. Diese Veränderung konnte mit zeitaufgelöster PTIR verfolgt werden. Die erreichte PTIR Aufnahmezeit war 15 s. Kontrollanalysen mit einem kommerziellen FTIR Mikroskope bestätigten die spektroskopischen Erkenntnisse.

Des Weiteren wurde die Alterung der AFM Spitze des PTIR Systems während fortlaufender Messungen eines Polymeres (Polystyrol, PS) und biologischer Proben (Zellen und Gewebe) untersucht. Es wurde gezeigt, dass lang andauernde Messungen von PS keinen Einfluss auf die Leistungsfähigkeit des PTIR Systems haben. Allerdings ließ die PTIR Empfindlichkeit bereits nach nur einigen Messungen von biologischen Proben merkbar nach. Eine Methode zur in-situ Kontrolle der Alterung und damit der Einsatzfähigkeit der AFM-Spitze wurde vorgeschlagen. Die AFM-Spitzenalterung wurde über die Signalintensität der δ_s(Si-CH$_3$) Bande beurteilt, welche einer stabile Verunreinigung der goldbeschichteten Spitze zugeordnet wird. Die vorgeschlagene Technik wurde erfolgreich während der Messung von biologischen Proben (Zellen und Gewebe) angewandt.

PTIR spektroskopische und bildgebende Messungen von einzelnen *E.coli* Bakterien, welche das Protein Meerrettichperoxidase in Form von „inclusion bodies" (IBs) enthielten, wurden durchgeführt. Es wurde festgestellt, dass die durchschnittliche Sekundärstruktur der IBs sich von der des restlichen Bakterium unterscheidet. Eine Methode zur quantitativen Analyse der vorhandenen IB wurde gezeigt.

PTIR und FTIR Spektren wurden von abgestorbenen (apoptotischen) und lebensfähigen Zellen nach einem histologischer Schnitt aufgenommt und analysiert. Die Ergebnisse der Nahfeldanalyse stimmen mit den mikroskopischen Messungen im Fernfeld überein. Insbesondere Änderungen der Sekundärstruktur von Proteinen und nichtlineare Eigenschaften der IR Absorption durch kondensierte Nukleinsäuren wurden festgestellt.

Des Weiteren wurden einzelne apoptotische sowie lebensfähige Zellen mittels der PTIR Technik charakterisiert. Zwei Arten von apoptotische Zellen konnten unterschieden werden. Einige Zellen zeigen Unterschiede in der Proteinsekundärstruktur zwischen Zellkern und Cytoplasma. Andere Zellen weisen keinen Unterschied in der Proteinsekundärdtruktur auf. Die beide Arten von apoptotische Zellen zeigen einen Rückgang der Absorptionsbande für Nukleinsäuren (C-N-C Streckschwingung von Ribose-Phosphat). Lebensfähige (Kontrol) Zellen zeigen keine signifikante Änderungen in der Proteinsekundärstruktur zwischen Zellkern und Cytoplasma. Es wurde festgestellt, dass die allgemeine Proteinkonformation im Zellkern der apoptotischen und Kontrollzellen unterschiedlich ist.

Der zweite experimentelle Teil beschäftigt sich mit der kombinierten (Multisensor) Bildanalyse von histologischen Proben unter Zuhilfenahme der molekülspezifischen Fourier-Transformation Infrarot (FTIR) Spektroskopie und der elementspezifischen Laserablation induktiv gekoppelte Plasma Massenspektrometrie (LA-ICP-MS).

Die kombinierte Analyse von FTIR und LA-ICP-MS Bildern von Tumorproben zeigte eine statistische Korrelation zwischen elementarer und molekularer Information. Zudem wurde durch die Kombination und gemeinsame Auswertung von Messdaten dieser beiden Methoden eine Verbesserung der Clusteranalyse ermöglicht. Dadurch gelang auch eine verbesserte Unterscheidung der verschiedenen Stufen der Apoptose.

Während der Multisensor Analyse von Dünnschnitten einer ischämischer Hirnläsion eines Rattenhirns wurden die Klassifikationsverfahren Partial Least Squares Diskriminanzanalyse (PLS-DA) und Random Decision Forest (RDF) angewendet und deren Leistungsfähigkeit bzgl. der Klassifizierung von verschiedenen Bereichen der Dünnschnitte verglichen. Beide Verfahren erlaubten zwischen unterschiedliche Gewebetypen unterscheiden zu können. Die Leistungsfähigkeit der Klassifikationsmodelle für den kombinierten (FTIR und LA-ICP-MS Daten) Datensatz wurde mit den Klassifikationsergebnissen basierend auf Daten der einzelnen Techniken verglichen. Die Multisensor Analyse war auch hier vorteilhaft. Unterschiedliche Gewebetypen wie weiße und graue Substanz, sowie Läsion und deren Umgebung konnten dadurch noch effektiver unterschieden werden. Des Weiteren zeigte die RDF genauere Klassifizierungsergebnisse als die PLS-DA.

Die dargestellten Ergebnisse dieser Arbeit zeigen die Fähigkeiten und Fortschritte der Nah- und Fern-Feld IR Mikrospektroskopie und der spektroskopischen bildgebenden Analyse von biologischen Proben. Im Zuge dieser Arbeit konnten auch die Vorteile einer bildgebenden Multisensoranalyse zur verbesserten Analyse von biologischen Proben gezeigt werden.

Acknowledgements

It is difficult to put in words my gratitude and respect to my supervisor Bernhard Lendl. Firstly, I thank Bernhard for providing me with opportunity to get practical experience with the state of the art analytical techniques while working in his group. I have felt his care and support throughout my doctoral studies. Thanks to Bernhard I developed not only essential scientific skills, but also have grown personally, became more decisive, mature and mentally stronger. I highly appreciate the provided financial support and opportunities for participation at conferences.

I thank Georg Ramer, who supported me before I started working in the group and helped even after his graduation. He shared his knowledge and expertise in IR spectroscopy, AFM and QCLs. Working in a team with him was always fun and productive.

I am grateful to Johannes Ofner who took his time to proofread my "multisensor" manuscripts and gave valuable suggestions for their improvement.

I would like to thank Andreas Swaighofer and Stephan Freitag for absolute support and especially for the final spell check of parts of this thesis.

Many thanks go to the whole CAVS Team. Although group members change from year to year, it is always a talented team where everyone is friendly and ready to help anytime. Especially I would like to thank Karin, Christoph, Andreas, Paul, Harald, Bettina, Jakob, Pily and all the Stefans. I am happy that I was a part of this team.

I appreciate the support of Cosima Koch who shared her experience in FTIR spectroscopy as well as Julia Kuligowski – the first who introduced me to multivariate analysis.

I would like to thank Anna Satzinger for helping with paper work, receipts and further formalities.

I would like to thank Minja Celikic for her assistance with rat brain FTIR measurements and data processing, as well as Florian Reisenbauer for taking care of the built PTIR system.

I appreciate Hans Lohninger for being supportive and answering chemometrical questions and providing the valuable ImageLab software.

I would like to thank faculty members and colleagues of the MEIBio doctoral program. In particular, Martina Marchetti-Deschmann and Gerhard Schütz who organized seminars and provided us with the opportunity for networking. I express my gratitude to Max Bonta and Andreas Limbeck with whom we established a productive collaboration.

I thank Elisabeth Eitenberger for taking her time and performing SEM and EDX spectroscopy measurements of the AFM tips.

Most of the results presented in this thesis would not be possible to achieve without a help of several research groups. I am extremely thankful to:

- Dieter Baurecht (University of Vienna), who shared his idea for of the PTIR time-resolved measurements;

5

Table of Contents

Acronyms

AFM	atomic force microscopy
AFM-IR	atomic force microscopy – infrared
ATR	attenuated total reflection
DNA	deoxyribonucleic acid
EC-QCL	external cavity - quantum cascade laser
EDX	energy dispersive X-ray
EM	electro-magnetic
EMSC	extended multiplicative scattering correction
IR	infared
IB	inclusion body
FTIR	Fourier transform Infared
FPA	focal plane array
HE	Hematoxylin and Eosin
HCA	hierarchical cluster analysis
HRP	horseradish peroxidase
LA-ICP-MS	laser ablation inductively coupled mass spectrometry
LDA	linear discriminant analysis
MCT	mercury cadmium telluride
PCA	principal component analysis
PC	principal component
PDMS	Polydimethylsiloxane
PMMA	Poly(methyl methacrylate)
PLL	poly-L-lysine
PLS-DA	partial least squares discriminant analysis
PSD	photosensitive detector
PSF	point spread function
PTIR	phothermal induced resonance
RDF	random decision forest
RMieES	Resonant Mie scattering
PS	polystyrene
PSF	point spread function
SEM	scanning electron microscopy
sSNOM	scattering scanning optical probe microscopy
TERS	tip enhanced Raman scattering
TUNEL	terminal deoxynucleotidyl transferase dUTP nick end labeling
QCL	quantum cascade laser

Introduction and motivation

Relevance of the work

Infrared (IR) spectroscopy allows non-destructive and label free detection of molecules and can be applied in biomedical research[1,2]. In particular, IR spectroscopic imaging can be used as a complementary to histological analysis tool for histological or microbiological studies. However, IR spectroscopy has certain limitations.

Firstly, due to the diffraction-limited spatial resolution of FTIR spectroscopy, features in the IR images can only be resolved at the scale of several micrometers. In contrast, near-field scanning probe techniques such as phothermal induced resonance (PTIR) or scattering scanning near-field optical microscopy (sSNOM) overcome this limitation and allow IR chemical imaging and spectroscopic measurements at the nanometer scale. Those techniques make use of the sensitivity and the high resolution of atomic force microscopy (AFM) with a spatial resolution that is only limited by the radius of curvature of the AFM tip (30 nm or less). The spectral properties of the sample are defined according to the local tip-sample interaction. Dynamic systems (evolving in time) were not studied yet by the near-field techniques.

In our group at TU Wien, a custom-made PTIR system was built and characterised. However, the influence of the AFM tip degradation on the system performance was not studied so far. Regarding analysis of biological samples, few near-field IR studies demonstrated the capability of imaging individual bacteria with protein inclusion bodies[3], but those studies provided no spectral analysis that would allow quantitative characterization of the protein content. Certain near-field studies demonstrated IR imaging of individual mammalian cells[3,4], however, so far only spectral regions related to protein content (amide I and II bands) were analysed.

Secondly, IR spectroscopy cannot provide elemental analysis. For gaining access to this information, complementary techniques, such as laser ablation inductively coupled plasma mass spectrometry (LA-ICP-MS) are needed. Combined statistical analysis of the data acquired with two or more techniques appeared to be more efficient than the conventional side by side analysis[5]. In our group, the combined (multisensor) image analysis was successfully applied to aerosol particles[6]. However, the capabilities of the combined application of these techniques regarding histological samples have not been evaluated so far.

Goals and objectives of this thesis

According to the relevant challenges of IR spectroscopy and gaps in practical knowledge, the main goal of this work is to advance the state-of-the-art of PTIR spectroscopy and PTIR imaging with regard to biological samples.

This goal was tackled through the analysis of various biological samples, such as mouse tumor and rat brain thin sections, individual bacteria and mammalian cells as well as a bio-polymer thin film.

The following points provide an overview about the performed work and their objectives:

- **Time resolved PTIR spectroscopy.** Implementing and performing time-resolved IR spectroscopic measurements of a bio-polymer thin film using the custom-made PTIR system.

- **PTIR system characterization.** Investigating the aging of AFM tips during prolonged measurements and studying its influence on the performance of the PTIR system.

- **PTIR spectroscopy and chemical imaging of individual bacteria.** Performing spectroscopic and image analysis of individual bacteria containing aggregated proteins.

- **PTIR and FTIR spectroscopy of a tumor tissue.** Comparing the results of near- and far-field spectroscopic analysis of apoptotic (dead) and viable tumors.

- **PTIR spectroscopy and chemical imaging of individual mammalian cells.** Characterizing intracellular morphology of apoptotic cells and viable cells.

- **Combination of FTIR and LA-ICP-MS image analysis for characterization of tumor thin sections.** Performing multivariate image analysis for discrimination and characterization of tumor tissues with different degree of viability. Finding statistical correlation between elemental and molecular chemical maps.

- **Combination of FTIR and LA-ICP-MS image analysis for improved multivariate image analysis.** Implementing different classification approaches to distinguish different brain tissue types and compare the performance of classification models built on the combined dataset with the classification results based on the individual datasets.

Methods of the study

In this work, primarily IR spectroscopy was used, in particular, FTIR and PTIR techniques. For the combined analysis, samples were additionally imaged using the LA-ICP-MS technique. Scanning electron microscopy (SEM) and energy dispersive X-ray (EDX) spectroscopy were used to support the results of the PTIR system characterization. Standard methods of histology such as staining Hematoxylin and Eosin (HE) and terminal deoxynucleotidyl transferase dUTP nick end labeling (TUNEL) staining were used to support the results of the combined image analysis. For data processing of imaging results, two analysis methods were utilized: univariate and multivariate. For the combined image analysis multivariate methods, such as k-means clustering, hierarchical cluster analysis (HCA) of principal component loadings, partial least squares discriminant analysis (PLS-DA), random decision forest (RDF) were utilized. The reproducibility of the acquired spectra was characterized by a standard deviation approach.

Scientific and practical novelty of the work

In this work for the first time the following achievements were accomplished:

- Implementation and performing of time-resolved PTIR spectroscopic measurements of a bio-polymer thin film. The temporally-resolved measurements monitored the changes in

secondary structure of a poly-L-lysine by means of changes in the shape of the amide I band in the PTIR spectra.

- Performance characterization of the custom-made PTIR system and its capabilities regarding practical aspects such as AFM tip aging.
- Proposition of a method for monitoring the PTIR performance of the AFM tip and its application to the measurements of the biological samples.
- Differentiation of the secondary structure of a recombinated protein within individual bacteria by PTIR spectroscopy.
- Proposing a method for the qualitative estimation of aggregated proteins.
- Discrimination of individual mammalian cells (dead and viable) by PTIR spectroscopy. Spectra and chemical images related to the nucleic acids were obtained.
- Application of combined image analysis of FTIR and LA-ICP-MS to tumor thin sections. The advantages of this method compared to a single technique analysis were demonstrated. In particular, improved cluster analysis and statistical correlation of the spatial distribution of elements and molecules were obtained.
- Application of combined image analysis of FTIR and LA-ICP-MS to post-stroke rat brain tissue thin sections. Combined analysis was found to improve the classification of different tissue types. Different classification approaches were implemented and their classification performance was evaluated.

Presentation of the results of the dissertation

The author has presented the results of this work at six international and two national conferences through two oral talks and 6 poster presentations. One poster presentation was awarded with a poster prize.

Publication of the results of this thesis

The results of this work were published in three papers in peer-reviewed journals.

Structure of the dissertation

This dissertation consists of three main chapters ("theoretical background and state-of-the-art", "materials and methods" and "results and discussion"), conclusion, bibliography, abstracts of the related publications and appendix.

Chapter 1

I. Theoretical background and state-of-the-art

In this chapter we discuss fundamentals of far-field mid-infrared (IR) spectroscopy, atomic force microscopy (AFM), near-field imaging techniques, such as ptotothemal induced resonance (PTIR). Then we give a basic introduction to biological processes undergoing in living systems and their analysis using IR spectroscopy. Further we provide a short introduction into the data analysis methods related to this thesis. Finally we provide the state-of-the-art developments and methods related to IR spectroscopic imaging of biological samples.

1.1. Infrared spectroscopy

This sub-chapter is guided by Griffiths et al.[7], Stuart et al.[8] and Kubitscheck[9].

Basic principles

Mid-IR spectroscopy is a powerful analytical technique based on the detection of vibrations and rotations of atoms or molecules at mid-IR frequencies (2.5-25 µm wavelengths) and allows for the chemical identification of a broad range of samples (gases, liquids, solids). A typical IR spectrum is acquired when IR radiation is passed through a sample and a fraction of the incident radiation absorbed at a particular energy is determined. Any peak appearing in this spectrum corresponds to the frequency of a molecular vibration or rotation. A collection of such peaks can be used to uniquely identify the chemical identity of the studied material.

We treat the IR radiation as a plane wave characterized by wavelength λ and frequency v:

$$\lambda = \frac{c}{v} \tag{1.1}$$

where c is the speed of light in vacuum. Wavenumber $\tilde{v}$ is common unit used in IR spectroscopy. Typically wavenumber is defined as the number of wave periods in a length of one centimetre:

$$\tilde{v} = \frac{1}{\lambda} = \frac{v}{c} \tag{1.2}$$

$\tilde{v}$ is expressed in the inverse centimetres (cm^{-1}).

IR spectroscopy can be explained in terms of quantum mechanics. According to the quantum theory, EM radiation can be represented as a stream of photons – light particles with the energy defied as:

$$E = hv \tag{1.3}$$

where h denotes the Planck constant and v – a vibrational frequency. A matter consisting of atoms and molecules can be described by quantized (discrete) energy levels (E_0, E_1, E_2, etc).

Molecules can interact with EM waves by means of absorption of photons. A molecule can absorb only photons with the energy that fits to the difference between the energy levels E_1 – E_0 or E_2 – E_1, etc. When a photon is absorbed, a molecule is transferred to a higher energy level and then relaxes back to the original state or the lower energy levels in a matter of nanoseconds.[7]

Vibrating molecule can be represented as a quantum harmonic oscillator in which atoms, linked via chemical bonds, periodically oscillate or vibrate. In such a quantum system, atoms oscillate with particular discrete frequencies v. The energy states of a harmonic oscillator can be described as follows:

$$E_n = hv(n + \tfrac{1}{2}) \tag{1.4}$$

where n is the number of energy level. A harmonic potential energy diagram of a two-atom molecule is depicted in Figure 1.1.1 by the dashed curve. In reality potential energy (interatomic distance versa energy level) is not harmonic but becoming more asymmetric when the molecule is excited to a higher vibrational state (Figure 1.1.1, solid curve).
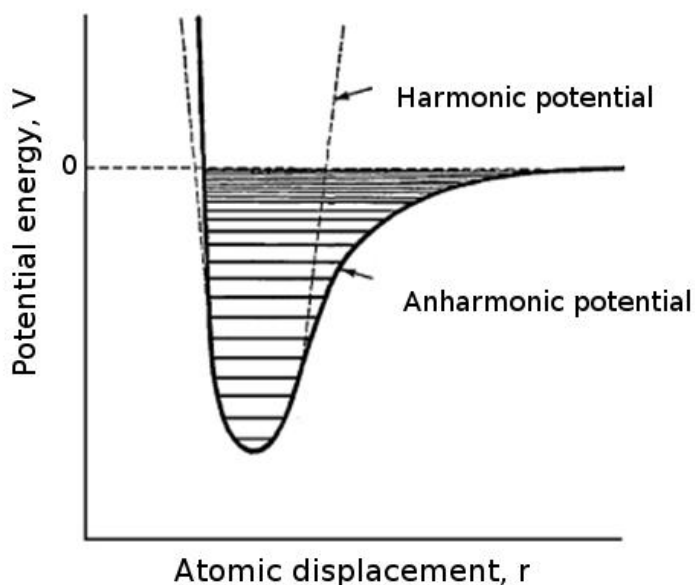
Figure 1.1.1. Potential energy diagram of an asymmetric two-atom molecule for a harmonic oscillator and an anharmonic oscillator. Adapted from Griffiths et. al [7].

The energy levels in this case can be written as follows:

$$E_n = hv\left(n + \tfrac{1}{2}\right) + hv\chi\left(n + \tfrac{1}{2}\right)^2 \tag{1.5}$$

where χ is the anharmonicity constant. Vibrational frequencies define the transition energies and highly characteristic for different bonds, i.e. one could identify functional groups according to them.[7]

A molecule can be considered as a system of masses that are connected by chemical bonds. Those bonds act as springs and are characterized by different stiffness constants k. For such

15

a model the frequency of vibration can be related to the bond stiffness as in the Hooke's law:

$$\nu = \frac{1}{2\pi}\sqrt{\frac{k}{m_r}},$$ (1.6)

where $m_r = \frac{m_1 m_2}{m_1 + m_2}$ is the reduced mass for a system of (two) atoms with masses m_1 and m_2. Thus, every lo9calized vibration has a specific oscillation frequency that depends on the atom masses and the strength of the chemical bond.

A molecule absorbs only radiation with the same frequency as the frequency of molecular vibrations. IR radiation cannot always be absorbed even though the photon energy matches the difference between two levels. In order to absorb a photon, a molecule should have a change in its electric dipole moment occurring during the vibration.

Atoms in molecules can oscillate in the different ways that are defined by their degrees of freedom. In general, each atom has three translational and three rotational degrees of freedom. Since the atoms are bonded in the molecule they perform a collective motion, thus, degrees of freedom are reduced. A molecule consisting of N atoms would have 3N-6 degrees of freedom.

According to different possibilities of a molecule to change its configuration in space, different kinds of vibrations exist. In molecules bonds either change in length (stretching or valence vibration) or in the angle between two bonds (bending). The stretching vibration can be symmetric (in-phase) or asymmetric (out-of-phase). Bending vibration can be either in plane or out of plane. Among the bending vibrations different types are exist (e.g. deformation, rocking, wagging or twisting).[8]

Experimentally, absorption of IR radiation by a homogeneous sample leads to the decay in the intensity of the light passing though (or reflecting from) the sample comparing to the intensity of the incoming light (Figure 1.1.2).
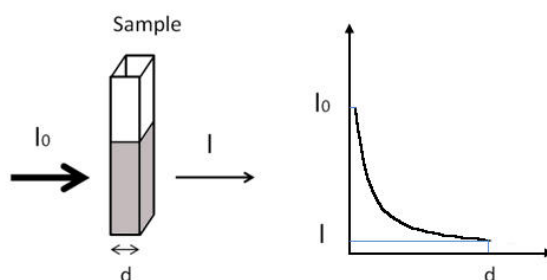

Figure 1.1.2. A schematic illustration to the Beer-Lambert law.

Absorbance of the sample $A(\tilde{\nu})$ at a wavenumber $\tilde{\nu}$ is given by a Beer-Lambert law:

$$A(\tilde{\nu}) = -log\frac{I(\tilde{\nu})}{I_0(\tilde{\nu})} = \varepsilon(\tilde{\nu})dc$$ (1.7)

where $I_0(\tilde{v})$ and $I(\tilde{v})$ are intensities of incoming and transmitted light, respectively; $\varepsilon(\tilde{v})$ is molar absorptivity or molar absorption coefficient that shows the ability of the sample to absorb the light at a particular wavelength (measured in $m^2 \, mol^{-1}$); d is the path length that light traverses through the sample (measured in m), c is the molar concentration ($mol \, m^{-3}$).

Instrumentation

Fourier transform Infrared spectroscopy

Fourier transform Infrared (FTIR) spectroscopy is the most common technique that allows for acquisition of IR spectra. This technique uses a Michelson interferometer that consists of a beam splitter, two mirrors (fixed and movable) and a detector (Figure 1.1.3).
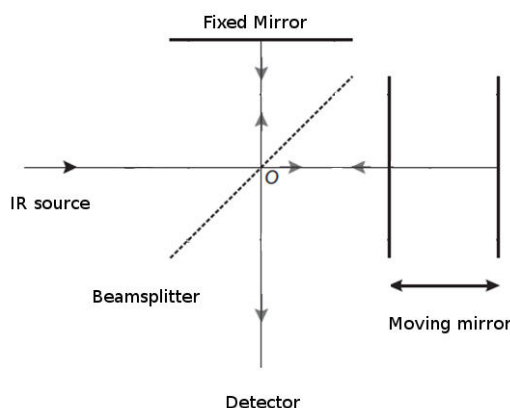
Figure 1.1.3. Optical scheme of Michelson interferometer used in FTIR spectrometer. Adapted from Griffiths et al. [7].

FTIR spectrometers use typically a thermal source (e.g. silicon carbide rod), that emits an IR radiation in the whole IR frequency range (broadband radiation). The working principle of an FTIR spectrometer is as follows: the beamsplitter (marked as O in Figure 1.1.3) separates the incoming light beam into two beams. One beam is reflected from a fixed mirror and is passed back through the beamsplitter to the photodetector. The second beam is reflected from another, movable mirror and is also redirected to the photodetector by the beam splitter (Figure 1.1.3). The movable mirror is linearly translated and the IR intensity as a function of the mirror position (interferogram) is recorded at the photodetector. The Mirror translation changes the optical path difference (OPD) between these two beams. Waves of different wavelength experience constructive or destructive interference depending on the OPD. Thus, the interferogram encodes information about all wavelengths. The IR spectrum representing the intensity as function of wavenumber (frequencies) is derived from the interferogram by means of a Fourier transformation.[7]

The absorption of a sample can be calculated according to the formula (1.7). The sample spectrum $I_1(\check{v})$ represents the intensity of the light recorded by the interferometer when the sample is placed into the optical path. It is also referred as single channel or single beam spectrum. The background spectrum or background channel $I_0(\check{v})$ represents the signal

intensity without the sample. Thus, the FTIR spectrum would represent the absorbance of the sample as a function of wavelength.

FTIR spectroscopy has three main advantages compared to the former established dispersive IR spectroscopy. The first one – "Jacquinot advantage" (no losses in signal intensity of incoming IR light due to the absence of apertures (slits). The second advantage – "Fellget advantage" (all wavelengths are measured simultaneously). This leads to fast spectra acquisition (few seconds per scan). As a result, signal-to-noise ratio is improved by a factor of $\sqrt{N}$ (N – the number of the sampled spectral wavelengths or repeated measurements). The third advantage – "Connes advantage". FTIR spectrometers use a Helium–Neon laser as an internal reference to derive the wavenumber scale by means of determining the mirror position. It is a stable and accurate method for wavenumber calibration comparing to the calibration methods used in dispersive spectrometers.[7]

Recently quantum cascade laser (QCL)-based IR spectroscopy has been developed. The related techniques use the advantages of QCL as a mid-IR light source that has high intensity and can be tuned across a broad wavelength region. Additionally, those spectrometers might provide an improved spectra acquisition speed comparing to FTIR spectroscopy. QCL-based IR spectrometers find many applications for the analysis of biomedical samples.[10]

By now FTIR spectroscopy is considered as a standard method for IR spectroscopy. Currently extensive reference databases based on FTIR spectra exist. Those spectra are collected from a number of various samples and can be used for material identification.

FTIR microscopy

The combination of a FTIR spectrometer with an IR microscope allows for investigation of small (few microns) or heterogeneous samples. IR spectroscopy can be used for microscopic imaging and is referred to as FTIR microscopy or microspectroscopy. IR microscopes are designed in a confocal configuration where the IR beam is directed and focused onto the sample by a focusing optical element (typically Cassegrain objective). The sample is placed on an x-y stage that can be moved in a raster-scanning manner. The area of the measurement at each point can be confined by a moving aperture. The light beam is passed through the sample (in the case of a transmission mode), collected by another Cassegrain objective and focused on a detector (typically mercury cadmium telluride, MCT). [9]

FTIR microscope can also operate in a reflection mode. In this case the same objective is used to focus the incoming IR beam to the sample and to collect the reflected light from it. Figure 1.1.4 shows a scheme of a typical FTIR microspectrometer.

Input IR beam from
FTIR spectrometer

Aperture

Cassegrain objective

Sample

Cassegrain objective

Output to detector
(transmission)

Aperture
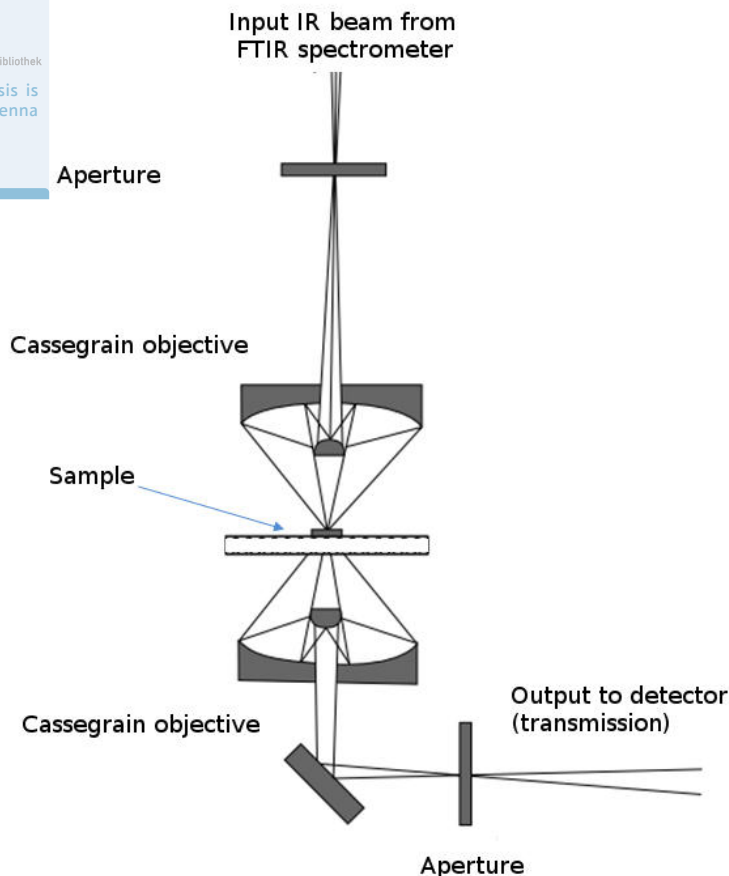
Figure 1.1.4. A scheme of a FTIR microspectrometer. Adapted from Stuart et al.[8]

Using FTIR microscpectroscopy, the sample can be raster-scanned, recording the spectra at single points in a user defined rectangular pattern. In FTIR microscopy also simultaneous measurements of several points can be achieved. For the latter, a focal plane array (FPA, 2.65 μm pixel size) or linear array detectors are utilized. The usage of FPA detectors in FTIR microscopy notably shortens the measurement time.[9]

An acquired FTIR microscopy image represents a hyperspectral dataset where to each measured point (pixel) a FTIR spectrum corresponds. From this dataset chemical maps that plot intensity values at an arbitrary wavelength can be generated. Those maps allow visualisation of the distribution of different molecules within the sample (see chapter 1.3). Also multivariate techniques can be used to created images.

Spatial resolution

Similarly to optical far-field microscopes, IR microscopes have a limited spatial resolution on the scale of $\sim\lambda$ which for mid-IR frequencies corresponds to 1.25-12.5 μm. The spatial resolution is the smallest distance at which two point-like objects can be differentiated. The fundamental diffraction-limited spatial resolution of the far-field microscopy is defined by the wavelength of the light and numerical aperture of the microscope. The numerical aperture is a product of the refractive index of the medium in which the objective is placed

and the sin of the half aperture angle of the objective. In case of an IR microscope spatial resolution is approximately equal to the wavelength of the IR radiation.[9]

Fundamental limitation of the optical resolution can be demonstrated from an example of a rectangular grating imaged by a microscope that consists of two lenses (Figure 1.1.5). The grating has a period d, which is close to a wavelength λ_0 of the light (in vacuum) that is used for illumination.
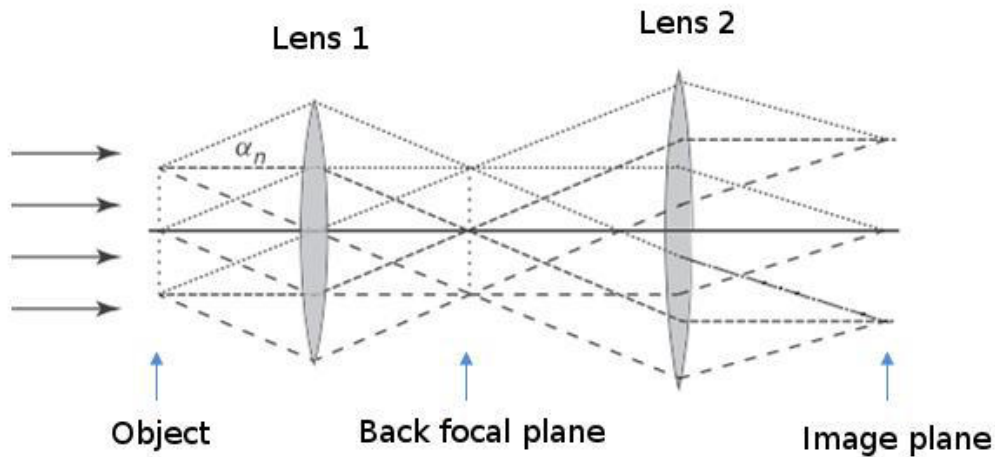
Figure 1.1.5. Imaging of a grating structure by a microscope. Adapted from Kubitscheck[9].

The incoming light is diffracted by the grating elements and propagates further at different angles α_n and interfere. Constructive interference occurs only for rays at particular angles α_n according to the Bragg condition:

$$2\,d\sin\alpha_n = N\lambda_0 \tag{1.7}$$

where N is the diffraction order. The related diffraction pattern is imaged in the back focal plane of the tube lens (image plane).

If d is reduced, one needs to increase α_n in order to image all features of the object (grating elements). However, a lens has a finite aperture (which cannot be infinitely increased because of practical reasons), therefore, not all diffracted rays can be captured by the lens. If the grating period $d < \frac{\lambda_0}{2\sin\alpha_n}$, then even the first diffraction pattern ($N=1$) would be incomplete. Thus, all the information regarding the structure of the imaged object at the scale smaller than d would be lost. If the light propagates in a medium with a refractive index n then the wavelength of the light would be reduced:

$$d < \frac{\lambda}{2\,n\sin\alpha_n} \tag{1.8}$$

Now we consider a single point-like object imaged by a microscope (Figure1.1.6). The object diffracts the incoming light into a spherical wave w_0. The lens 1 transfers this wave into a plane wave w_1.
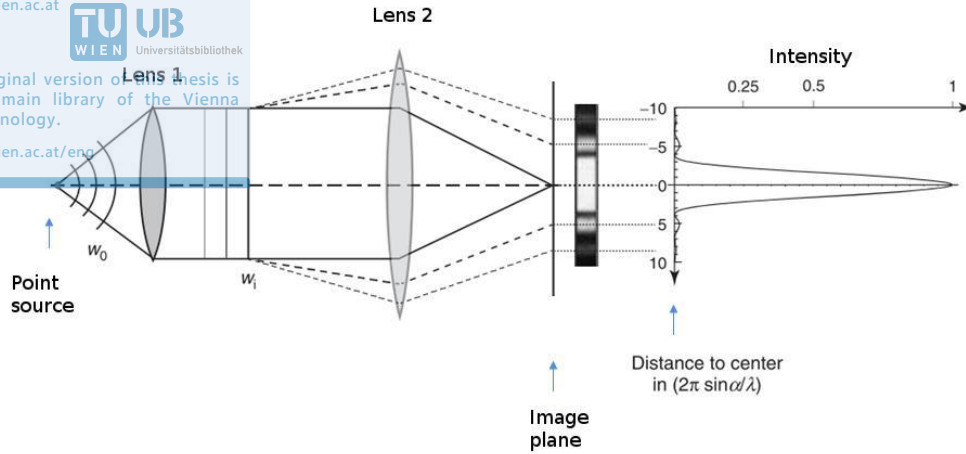
Figure 1.1.6. Image formation of a point-like object by an optical microscope. Front. Adapted from Kubitscheck[9].

Following the Huygens principle, every point of the wavefront w_1 can be considered as a so-called Huygens wavelet. All wavelets are coherent and interfere with each other. The resulting diffraction pattern is projected by second lens 2 into the image plane.

The constructive interference occurs at the focus of the lens (Figure 1.1.6, bright region) and represents the image of the point object. The image appears as a disc with a finite size because only a finite number of wavelets have been interfered upon a limited lens aperture. The region of the constructive interference follows a ring related to a destructive interference (Figure 1.1.6, dark region). Further the second "constructive" ring follows and then another "destructive" ring and so forth. The intensity distribution of such a diffraction pattern is known as Airy pattern and represents a point spread function (PSF). The PSF defines the degree of smearing the point object by an optical system.[9]

Rayleigh suggested a criterion according to that the two imaged objects with the related PSFs can be resolved: when the center of one PSF coincides with the first minimum of the second PSF. According to that criterion the resolution limit is equal to the first minimum of the Airy function and is defined as follows:

$$\Delta x \approx \frac{0.61\,\lambda}{n \sin \alpha} \tag{1.9}$$

Δx is derived by Kubitscheck et. al [9] from the zero of the first order of the Bessel function J_1 that describes the Intensity of the Airy function:

$$I(r) = I_0 \left[\frac{J_1(2\pi\,\Delta x\ \text{n} \sin \alpha/\lambda)}{2\pi\,\Delta x\,\text{n}\ \sin \alpha/\lambda} \right]^2 \tag{10}$$

where I_0- light intensity in the focus of the lens, the first zero of the Bessel function is at $\frac{2\pi\,\Delta x\,\text{n} \sin \alpha}{\lambda} \approx 3.83$

Thus, if with two PSFs spaced from each other at a distance smaller than Δx, the related objects cannot be resolved (Figure 1.1.7 A).

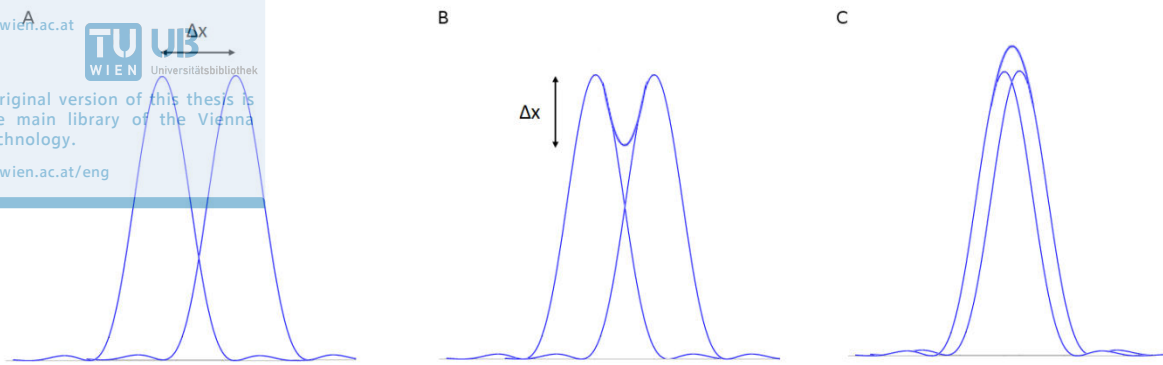**Figure 1.1.7.** Spatial resolution criteria. Two resolved PSFs according to the Rayleigh (A) and Sparrow (B) criteria; two unresolved PSF (C).

Sparrow criterion is another criterion that defines the resolution limit. According the Sparrow criterion, two PSFs can be resolved until the dip between them is detectable (Figure 1.1.7 B). When the PSFs are too close, they overlap and no dip is observed (Figure 1.1.7 C).[9]

An increase of the acceptance angle of an objective might improve the spatial resolution but leaving it limited (finite lens aperture). On the other side, the spatial resolution can be improved when the refractive index of the surrounding medium is increased. In optical microscopy for that purpose objectives are immersed into water or oil. In IR microscpectroscopy the refractive index is increased when an attenuated total reflection (ATR) element is applied. ATR microscopy uses typically germanium crystals ($n \approx 4$) that are placed („immersed") into close proximity to the sample. However, even with the increased spatial resolution by a factor of 4, it is still challenging to resolve sample features below 1 µm with an ATR microscope. This prohibits the subcellular analysis of many biological samples.

Near-field Infrared imaging techniques

Near-field techniques avoid the diffraction limit while registering IR signal at the distances comparable or smaller than the wavelength of the incoming radiation. Those techniques allow spectroscopic and chemical image analysis at the nanoscale. The common nanoscopic imaging methods are scattering scanning near-field optical microscopy (sSNOM) and photothermal induced resonance (PTIR). The latter is also referred to as atomic force microscopy – infrared spectroscopy (AFM-IR). Both techniques make use of the sensitivity and the high resolution of the AFM to sense a special interaction between a sharp atomic force microscope (AFM) tip (dimensions 30 nm or less) and the sample. Spectral properties of the sample are determined according to the local tip-sample interaction. By raster scanning the sample, which is illuminated with a wavelength of interest, and collecting the signal from every point of measurement chemical maps can be generated.

Photohermal induced resonance

In PTIR nanoscopy an AFM is used to detect IR absorption of a sample by means of sensing its photothermal expansion upon repeated excitation. In this technique an IR laser beam is focused on the sample. While the laser spot size cannot be reduced beyond the diffraction limit, the sample thermal expansion may vary at the nanoscale and local absorption can thus be detected by the AFM tip which is brought in contact with the sample. Absorption of the incoming IR photons follows local increase in temperature and thermal expansion of the sample. Upon absorption the sample expands and pushes an AFM tip leading to a cantilever deflection. Thus, the magnitude of an AFM cantilever deflection is directly related to the photoexpansion which in turn is proportional to the absorption of the sample. A photoexpansion spectrum is generated by means of recording the cantilever deflection when the tip is kept at the same position and the laser is swept across a range of wavelengths. A photoexpansion image, that carries information regarding the spatial distribution of an analyte (molecule), is produced when the laser is tuned to a single wavelength of interest (usually where the analyte has absorption) and the sample is raster scanned while recordering the cantilever deflection[11].

Scattering scanning near-field optical microscopy

s-SNOM allows for spectroscopic and chemical image measurements with the spatial resolution on the scale of ten nanometers[12,13]. In s-SNOM a sharp AFM tip (typically metal coated) is brought close to a sample and illuminated by a focused IR light beam. The intensity of the backscattered light from the tip is then detected in the far-field by a photodetector. The illuminating light creates a hot-spot at the AFM tip apex (lightning rod effect). The AFM tip interacts with the sample within this hot spot causing near-field interaction. This near-field interaction affects the backscattered light, while the small size of the hotspot localizes the interaction to the nanoscopic volume just below the tip. The scattered signal depends on the optical/dielectric properties of the sample und thus carries information on the sample's local optical properties. In particular, the scattered electric field depends on the polarizability of the sample-tip dipole, which is in turns depends on the dielectric constants. The polarizability is a complex value that carries information regarding a relative amplitude and a phase shift between the incident and the scattered light. The local absorption can be derived as an imaginary part of the polarizability[14].

In order to separate the near-field signal from the parasitic background the tip is oscillated at a small frequency Ω. The near-field signal is demodulated by a multiple of the tip vibration frequencies (n=2, 3). This signal modulation allows simultaneous measurements of optical amplitude and an optical phase. Thus, by scanning the AFM tip across the sample and detecting the scattered signal amplitude and phase maps are generated. In sSNOM one can detect the near-field signal by means of homodyne, heterodyne or pseudo-heterodyne interferometric techniques. sSNOM spectra can be acquired for wavelengths ranging from visible light to terahertz depending on the light source. The spatial resolution is determined by the radius of curvature of the AFM tip apex.

1.2. Basic principles of AFM

In this sub-chapter we discuss basic principles of atomic force microscopy (AFM) which are guided by [15–17].

Brief introduction

Atomic force microscopy (AFM) was invented by G. Binnig, C. Quate and C. Gerber more than thirty years ago.[18] AFM is one of the scanning probe (SPM) techniques that measures various interaction forces (repulsive, attractive, van der Waals, electrostatic, magnetic) occurring when a sharp tip is placed in a close proximity to the sample. AFM imaging is achieved by means of the detection of the deflections of an elastic AFM cantilever (fixed to the tip) raster-scanned over the sample surface (Figure 1.3 A). The deflections are caused by the interaction forces between the tip and the sample surface. Among the existing interaction forces, the most dominant are inter-atomic repulsive forces that occur at short-range distances (Figure 1.2.1 B). Besides that on the cantilever act long-range forces (coulmb or dipole-dipole interactions, polarization, van der Waals or capillary forces) that can be either repulsive or attractive.
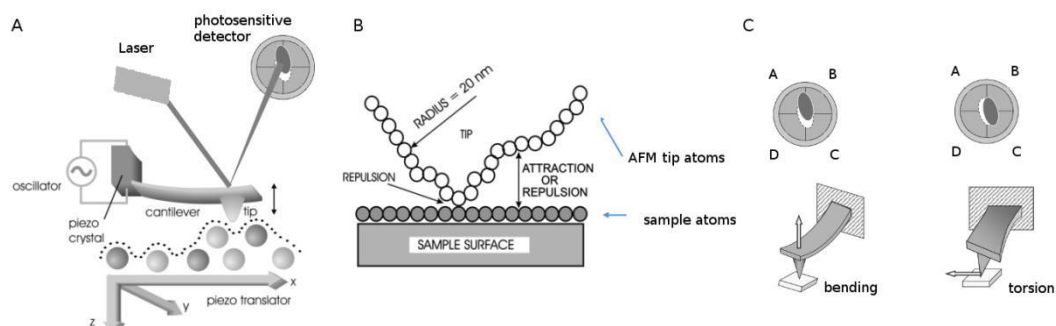
Figure 1.2.1. (A) The schematic illustration of the AFM principle. (B) The scheme of forces acting between the tip atoms (white circles) and the sample atoms (gray circles) (C). Detection bending and torsion deformations by PSD. Adapted from Friedbacher and Bubert [15] and from Mironov et al..[19]

When the tip is scanned across the sample interaction forces act on it and that leads to cantilever deflection. Depending on the deflection degree one can estimate the magnitude of the interaction forces. Cantilever deflection is measured by a change in the position of the laser beam reflected from the back side of cantilever to the position-sensitive photo detector (PSD) (Figure 1.2.1C). PSD consists of four detectors that allow detection of different cantilever deformations. Bending deformation (vertical deflection) is detected through the difference in voltages of the upper and lower part of the PSD. Torsional deformation (horizontal deflection) is detected through the difference in voltages of the left and right part of the PSD (Figure 1.2.1C). During scanning over the sample, the deflection signal changes are detected by the PSD giving topographical information of the surface. For a

better reflection of the laser beam and therefore a better detection of the cantilever deflection, the back side of the cantilever is coated with a thin layer of gold or aluminium. Spatial resolution and performance of AFM is determined by the tip radius and the sensitivity of the PSD. The spatial resolution of AFM is defined by the tip radius of curvature and can be less than a nanometer. Currently AFM cantilevers are fabricated from silicon or silicon nitride by microfabrication techniques. The most common geometries of cantilevers are beam shaped (rectangular) and triangular.

As was outlined before, when the cantilever is brought close to the surface a force acts on it and the cantilever deflects. Thus, a cantilever can be treated as a spring that obeys Hooks law:

$$F = -kx \qquad (1.11)$$

where F – force acting on a cantilever k – force constant or spring constant (has orders of magnitude $0.0005 - 40$ N/m depending on cantilever type), x – cantilever deflection. According to the Hooks law the force acting on the cantilever is directly proportional to its deflection.

Qualitatively the interaction of the AFM cantilever with the surface can be described by the Lennard Jones potential:

$$U_{LD}(r) = U_0 \left\{ -2 \left(\frac{r_0}{r} \right)^6 + \left(\frac{r_0}{r} \right)^{12} \right\} \qquad (1.12)$$

where U_{lD} – Lennard Jones potential, U_0 – minimum energy, r – distance between the atoms of the cantilever and the surface, r_o – distance between the atoms of the cantilever and the surface when they are in equilibrium.

The first part in the formula (1.12) describes long rage attractions (e.g. van der Waals forces). The second part describes repulsion at short ranges due to overlapping electron orbitals. The illustration of the Lennard Jones potential is given in Figure 1.2.2.
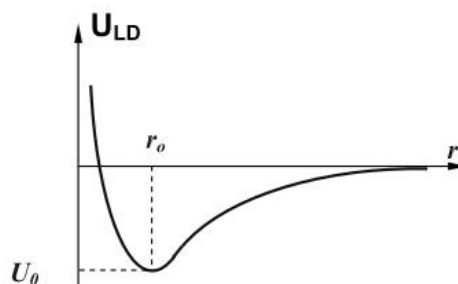

Figure 1.2.2. Lennard-Jones potential curve. Adapted from Mironov [19].

Thus, the AFM cantilever feels attraction from the sample at long distances and repulsion at short distances. In AFM the interaction between the tip and the sample is characterized by so called force-distance curves (Figure 1.2.2).
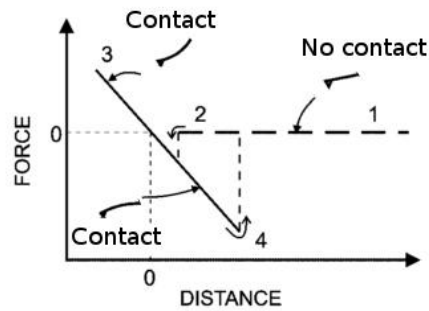
Figure 1.2.3. Force distance curve and different bending of canteliver. Adapted from Friedbacher and Bubert [15].

A force-distance curve describes changes in the force acting between the cantilever and the sample when the distance between them varies. At a large distance the tip does not interact with the sample and the acting force is equal to zero (Figure 1.2.3, the region between 1 and 2). When the tip is approached closer the sample (Figure 1.2.3, point 2), it feels the attraction from the sample (due to van der Waals forces) and jumps into contact. When the tip is moved further towards the sample, it feels the repulsive force. When the tip is retracted again (Figure 1.2.3, the region between 3 and 4) the interaction force is reduced. Below the zero line the tip feels the attractive force (due to adhesion to the sample). A further tip retraction leads to the separation of tip from the sample.

An AFM can be operated in different modes the most common of them are contact mode and tapping mode.

In the **contact mode** AFM imaging is usually performed within the repulsion mode and the tip stays in touch with the sample (Figure 1.2.3, the region between 3 and 4).[17] A setpoint is a user defined force value that is kept constant during the measurements. The values of the setpoint should be optimized to achieve high quality images. Reducing setpoint values means reducing the force acting between the cantilever and the sample. High setpoints frequently lead to tip or sample damages.

In contact mode the distance between the cantilever and the sample is kept constant while the cantilever position is constantly adjusted. The feedback loop adjusts the position of the cantilever by reading out its deflection. In AFM commonly a P-I (proportional-integral) feedback is used. The difference between the setpoint and the force is used to change the height position of the cantilever. The height position can be updated by varying two parameters: a time constant for the integrator and a value for the proportional gain. P and I describe how quickly the system (feedback) responds to changes in sample topography. Those values should be optimized depending on the imaging conditions, sample topography and scan speed. Typically large P and I coefficients would lead to a quicker reaction to changes in the topography.

The direct contact between the tip and the sample in the contact mode is considered as a main disadvantage since it may lead to damage of the tip or the sample. Therefore, contact mode is not recommended for the analysis of soft samples, such as biological samples.

In **tapping (dynamic) mode** the cantilever oscillates (usually with a sinusoidal motion) near its resonance frequency. This oscillation is driven by a piezo element. By applying several frequencies to the cantilever and detecting the deflection values a frequency spectrum can be obtained. The frequency value corresponding to the maximum in this spectrum is called resonance frequency of the cantilever. Typical values of the resonance frequencies are in the kHz region. Unlike to contact mode, intermittent contact between the tip and the sample occurs during in tapping mode. The cantilever typically behaves similarly to a single harmonic oscillator. When the vibrating cantilever approaches the surface, its amplitude is reduced and also phase and the frequency of the cantilever oscillations undergo changes. Those changes are due to tip-sample interactions and related to the sample material properties. The response time of the cantilever damping depends on the so called quality factor. The quality factor of a cantilever is defined as a ratio between the bandwidth of the resonance peak and the resonance frequency. High quality factors are favourable in AFM measurements since they provide a better signal-to-noise ratio. The values of the quality factor for a freely oscillating cantilever in vacuum are high, but reduced in case of air or liquids (less than 100 and 10 respectively). However, the quality factor can be compensated electronically (so called Q-control).

Since the oscillating tip contacts the sample not constantly but periodically, the tapping mode is less damaging than the contact mode. It is suggested to be used for imaging soft materials, such as biological samples.

An AFM can be operated in either in constant force (amplitude) mode or in constant height mode. In constant force mode the deflection of the cantilever is constant while the sample is adjusted in a vertical direction. In case of rough samples, the scan speed should be lowered in order not to damage the tip or the sample. An AFM operated in the constant height mode keeps the vertical position of the sample constant. At the same time the cantilever deflection is varied and detected. This mode allows high scan rates but is appropriate only for relatively flat samples.[15]

AFM can be operated in several different modes. The most common of them are friction force microscopy (FFM), Young's Modulus Microscopy (YMM), phase imaging and force-distance curve measurements. Those AFM modes attempt to deliver, besides topographic information, also additional information regarding the material-specific properties of the sample.[15]

FFM measures cantilever torsional deformations of the cantilever. This brings information on lateral forces and friction. YMM measures indentation of the tip into the sample. According to the measured values one can estimate elastic properties of the sample. Phase imaging detects the damping of the oscillation during the tapping mode while recording the phase difference between the initial piezo oscillation and the measured responding oscillation of the cantilever. Phase imaging allows visualization of material-specific contrast related to elastic or adhesive properties of the sample. Force-distance curve measurements provide information regarding interactions between the AFM tip and the sample.[15]

AFM cantilever bending modes

In this sub-chapter we consider a beam shaped AFM cantilever with length L, width w and thickness t (Figure 1.2.4 A). An AFM cantilever has several bending possibilities or vibration modes (Figure 1.2.4 B). Different bending modes are excited when the cantilever is driven to oscillate with a particular resonance frequency.
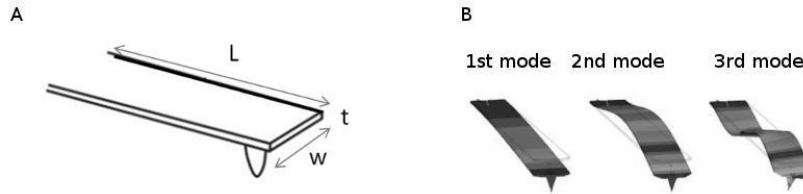
Figure 1.2.4. (A) A sketch of a beam cantilever. (B) The first three resonant mode frequencies of a beam cantilever. Adapted from Eaton[17] and Reifenberger et al.[16].

Oscillations of a cantilever obey fundamental mechanic principles. For a homogeneous rectangular (beam) shaped cantilever the equation of motion for flexural vibrations is defined by the Euler–Bernoulli differential equation[16,20]:

$$EI\frac{\partial^4 z}{\partial x^4} = -\rho A \frac{\partial^2 z}{\partial t^2} \tag{1.13}$$

where z - is the vertical deflection from the rest position; E – the Young's modulus of the cantilever, I – moment of intertia ($wt^3/12$), ρ – density of the cantilever material, A – cross section (wt).

Equation (1.13) can be solved analytically:

$$z(x,t) = (a_1 e^{kx} + a_2 e^{-kx} + a_3 e^{ikx} + a_4 e^{-ikx})e^{-i\omega t} \tag{1.14}$$

where k – wavenumber ($k = \frac{2\pi}{\lambda}$), ω - angular frequency ($\omega = 2\pi f$) and a_i (i=1,2,3,4) are constants.

The boundary conditions are resulting from clamping the cantilever on one side as follows:

$$\begin{cases} z(0) = 0, & \text{no motion at the clamped side} \\ \dfrac{\partial z(0)}{\partial x} = 0, & \text{no slope at the clamped side} \\ \dfrac{\partial^2 z(L)}{\partial x^2} = 0, & \text{no moment at the free side} \\ \dfrac{\partial^3 z(L)}{\partial x^3} = 0, & \text{no shear force at the free side} \end{cases}$$

After solving the system of equations the following equation can be obtained:

$$cos\, k_n L \cosh k_n L + 1 = 0 \tag{1.15}$$

where k_nL solutions of the equation exist, k_n – wavenumber of a flexural vibration mode , n – the mode number (n=1,2,...). This equation can be solved numerically (e.g. using software Mathematica) and the first three solutions would be related to the first three vibrational modes:

$$k_1L = 1.8751$$
$$k_2L = 4.6941$$
$$k_3L = 7.8548$$

By plugging (1.5) and (1.4) in (1.3), the resonance frequency for the nth mode would be:

$$f_n = \frac{(k_nL)^2}{2\pi L^2} \sqrt{\frac{EI}{\rho A}} \tag{1.16}$$

Thus, the position of the resonance frequency depends on geometric and material properties of the cantilever as well as on the number of the vibration mode.

1.3. Basic principles of PTIR

Here we discuss the key aspects of PTIR together with the currently existing PTIR methods. This sub-chapter is guided by [11,21,22].

Photoexpansion force

When a molecule absorbs a mid-IR photon a vibrational mode is excited and the molecule is transferred to a higher energy level. The excited molecule releases the gained energy through a non-radiative transition to its lower energetic level and contaminant energy transfer to surrounding molecules. This causes a heating of the sample where absorption took place. The resulting increase in volume is referred to as thermal expansion of the sample. As a result, a photoexpansion force acts from the sample on an AFM tip when placed in contact with the sample. The photoexpansion force can be explained from the force - distance curve graph (Figure 1.3.1).
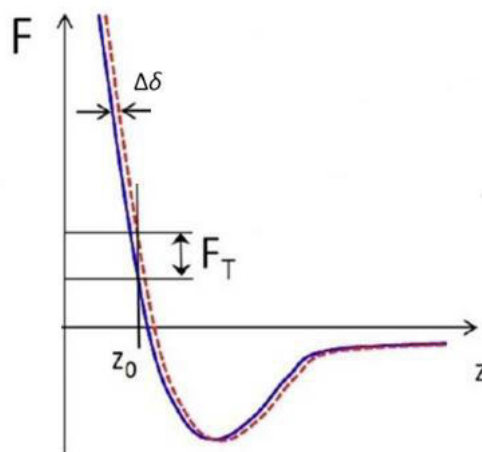
Figure 1.3.1. Scheme of AFM cantilever deflection during sample photoexpansion. Adapted from Lu and Belkin [21].

The solid curve (Figure 1.3.1) is related to the tip-sample interaction before the laser excitation. z_0 is the distance between the AFM tip and the sample in contact mode. Upon excitation by a laser pulse the sample expands. The sample photoexpansion develops almost instantaneous compared to the response time of the AFM, which is 5 μs, assuming cantilever resonance frequency of 200 kHz. Therefore, even though the position of the tip has not been changed right away, the force distance curve is shifted (Figure 1.3.1, dashed curve). The value of this shift corresponds to the sample expansion $\Delta\delta$. From those force distance curves one can find the value of the photoexpansion force F_T that acts on the AFM tip from the expanded sample.[21]

Lu et al. estimated values of the photoexpansion force using the Derjaguin-Muller-Toporov (DMT) model. [23] This model evaluates the sample – tip interaction by means of calculation the force that acts between an elastic plane (sample) and a rigid sphere (tip) (Figure 1.3.2).
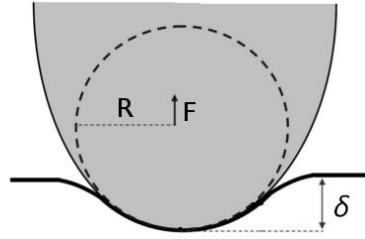
Figure 1.3.2. Graphic illustration of the sample indentation δ caused by the AFM tip brought in contact with the sample. F – repulsive force acting between the tip and the sample. R – radius curvature of the tip. δ – indentation depth. Adapted from Kontomaris et al [24].

When an AFM tip is in contact with the sample, two forces act on it. The first is repulsive due to the elastic sample deformation. This force acts in the area of contact between the tip and the sample. The second is attractive due to van der Waals forces. This force acts on the part of the tip that is not in contact with the surface. The resulting force with which tip and the sample interact was defined Lu et al.[23]:

$$F = \frac{4}{3}E^*R^{1/2}\delta^{3/2} - 2\pi Rw \qquad (1.17)$$

where E^*- the reduced Young's modulus; $2\pi Rw$ – the pull off force due to sample adhesion. In case of the tip-sample distance change (sample expansion) $\Delta\delta$ much smaller than δ, the photoexpansion force F_T will be defined as:

$$F_T \approx 2E^*R^{1/2}\delta^{1/2}\Delta\delta \qquad (1.18)$$

By plugging the following values for a $CH_3(CH_2)_{17}SH$ monolayer: E^* = 5 GPa, R = 25 nm; δ = 0.7 nm ; Δδ = 3.2 pm into (1.18), F_T is estimated about 0.13 nN. [23]

Thermal diffusion length

Spatial resolution of PTIR imaging is connected with the thermal diffusion length. The thermal diffusion length depends on the thermal diffusivity μ and the light pulse width τ [25,26]:

$$L_d = \sqrt{\mu\tau} \qquad (1.19)$$

Thermal diffusivity is defines as follows:

$$\mu = \frac{k}{\rho C} \qquad (1.20)$$

where k – heat conductivity, ρ – density, C – heat capacity.

Lu and Belkin [21] estimated thermal diffusion length $L_d \approx 100\ nm$ for chem/bio polymers with typical values k = 0.5 W m^{-1} K^{-1}, ρC = 2 J cm^{-3} K^{-1} , for a light pulse $\tau = 40$ ns .

Photoexpansion signal

The main concept of the PTIR technique is based on the assumption that the detected photoexpansion signal is proportional to the absorption (imaginary part of the complex refractive index) of the sample. Theoretical calculations showed that the amplitude of the PTIR is indeed related to the absorption.[22] Dazzi et al. considered an absorbing spherical particle with a constant complex refractive index and constant mechanical properties. Furthermore, they assumed measurement in the ATR configuration and using a rectangular AFM cantilever. The authors assumed that the cantilever obeys Euler-Bernoulli mechanics. It was supposed that a single laser pulse causes photoexpansion. Different pulse durations ranging from nanoseconds to several microseconds were discussed.

The calculations showed that the amplitude of the PTIR signal of mode n can be expressed as a product of five contributions:

$$\tilde{S}_n(\omega_n, \lambda) = H_m H_{AFM} H_{opt} H_{th} \frac{Im(n(\lambda))}{\lambda} \qquad (1.21)$$

where ω_n – frequency; $Im(n(\lambda)$ - imaginary part of the refractive index of the sample; λ - wavelength of the incoming radiation. In the following these contributions will be discussed separately.

Mechanical contribution:

$$H_m = k_z \alpha_{sph} a \qquad (1.22)$$

where k_z - the spring constant of the force between the tip and the sample, α_{sph} - thermal expansion coefficient of the sample, a – the radius of the spherical sample.

H_m describes the mechanical contribution of the expanding spherical sample.

Cantilever contribution:

$$H_{AFM} = \frac{1}{\Gamma \omega_n} (\delta x \cos \alpha + H \sin \alpha) \frac{D}{\rho A L} \left[\frac{\partial g_n(x)}{\partial x} \bigg|_{x=L} \right]^2 \qquad (1.23)$$

where Γ - the damping of the cantilever; ω_n - the resonance frequency of n mode; α – the angle between the cantilever and the sample surface; δx - the distance from the tip to the end of the cantilever; H – the tip height; D - the diameter of the deflected laser spot on the cantilever; ρ – the density of the cantilever material, A – the cross section of the cantilever; L – length of the cantilever; $\frac{\partial g_n(x)}{\partial x} \bigg|_{x=L}$ - the slope of the cantilever at its end.

H_{AFM} describes the properties of the AFM cantilever.

Optical contribution:

$$H_{opt} = \frac{Re(n)}{(Re(n)^2+2)^2} c \varepsilon_0 |E_{inc}|^2 \qquad (1.24)$$

where $Re(n)$ – the real part of the refractive index; c – the speed of the light; ε_0 – the dielectric constant in vacuum; $|E_{inc}|^2$ - incident laser power.

H_{opt} describes the influence of the refractive index and the incident laser power on the signal.

Thermal contribution:

$$H_{th} = \begin{cases} \frac{6\pi}{\rho_{sph} c_{sph}} t_p \left(\frac{t_p}{2} + \tau_{relax} \right), \ t_p \ll \tau_{relax} \\ \frac{4\pi a^2}{\kappa} \left(\frac{\sin(\frac{\omega_n t_p}{2})}{\omega_n} \right), \ t_p \gg \tau_{relax} \end{cases}$$ (1.25)

where ρ_{sph} - density of the sample; c_{sph} - the thermal capacity of the sample; t_p – pulse length; τ_{relax} – the relaxation time of the sample; a - the radius of the spherical sample; κ - the effective heat conductivity. H_{th} describes the influence of the pulse duration and material properties of the sample. Here two extreme cases can be distinguished where the excitation pulse is either much shorter or much longer compared to the sample relaxation time.

In the complex expression (1.21) most of the parameters besides the last fifth contribution $\frac{Im[n(\lambda)]}{\lambda}$ are constant or do not change during the measurement. Taking into account that at a microscopic scale the absorbance spectrum of a layer with thickness z is described by the by the Beer–Lambert formula:

$$\alpha_{abs}(\lambda) = \frac{4\pi z}{\lambda} Im[n(\lambda)] \propto \frac{Im[n(\lambda)]}{\lambda}$$ (1.26)

where λ denotes wavelength of the light; n is the complex refractive index of the material. For a given layer with the thickness z, the absorbance is proportional to the ratio $\frac{Im[n(\lambda)]}{\lambda}$.

Thus, comparing formulas (1.21) and (1.26) we conclude that the amplitude of the signal recorded is directly proportional to the absorption of the sample. In the first approximation, the AFM cantilever deflection is linearly proportional to the absorbed optical energy. Thus, molecular absorption α_{abs} can be obtained after normalization of the AFM cantilever deflection to the laser intensity:

$$\frac{\tilde{S}_n(\omega_n, \lambda)}{I(\lambda)} \propto \alpha_{abs}$$ (1.27)

where $\tilde{S}_n(\omega_n, \lambda)$ - AFM cantilever deflection, $I(\lambda)$ - incident laser intensity.

Detection methods of the photothermal signal

There are currently two methods which are used to extract the photothermal signal: ring down and resonance excitation.

Ring down

The ring down detection of phothermal expansion signal was demonstrated by Dazzi et al.[27]. The technique is frequently referred as atomic force microscopy – infrared (AFM-IR) spectroscopy. AFM-IR [27,28] was performed using a CO_2 laser with an optical parametric oscillator (OPO) or a free-electron laser (FEL). The OPO source was operated with 10 ns pulse length with laser (50 mW) at repetition rate 10 kHz. The FEL was operated with 8 µs long train of ps pulses (50 mW) at repetition rate 25 Hz. Later Dazzi et al.[29] estimated the temperature increase upon photothermal expansion of a dry bacterium by FEL with 9 µs pulse length, consisting of 600 micropulses each separated by 16 ns to be 10 K.

In the ring down experiments each laser pulse forces an AFM cantilever to oscillate around its equilibrium, the amplitude of those oscillations fades with time (Figure 1.3.5, left). Considering pulse length and repetition frequency the cantilever had enough time to return to the equilibrium state prior to the next laser pulse.
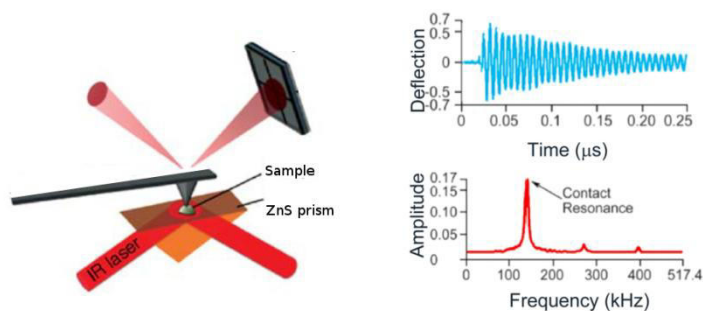
Figure 1.3.3. Illustration of the ring down PTIR scheme. The IR laser beam illuminates a sample deposited on a ZnSe prism through ATR. Photoexpansion signal sensed through the deflection of the AFM tip placed in contact with the sample is recorded by an oscilloscope. Adapted from Dazzi et al.[11,30]

The Fourier transformed time-dependent deflection signal results in a frequency spectrum that consists of a few peaks centered at the frequencies of the cantilever contact resonances (bending modes). From this frequency spectrum the amplitude at a chosen resonance is recorded. The IR spectrum is constructed as a function of those signal intensities recorded for different wavelengths.

The ring down excitation method allowed the detection of polymer films with a minimum thickness of about 15 nm[31]. A further increase in sensitivity would only possible by increasing the power of the laser, which however would lead to the damage of the sample.

Resonance excitation

As the name suggests, in this PTIR technique resonance excitation is used to detect the photothermal signal. Resonance excitation improves the sensitivity of the photothermal spectroscopy compared to ring-down detection. In the resonance excitation method the repetition frequency of the laser is matched to one of the resonance frequencies of the cantilever. In the resonance excitation the deflection of the cantilever builds up from short

laser pulses. As a result the response of the cantilever is significantly increased, therefore, improving the sensitivity (Figure 1.3.4).
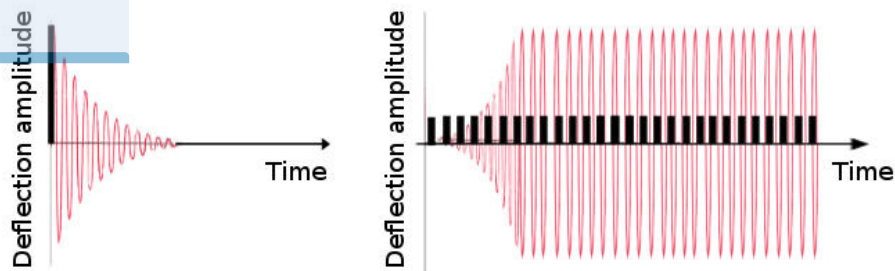
Figure 1.3.4. Illustration of different modes of excitation the deflection of the AFM cantilever. (left) Ring mode, (right) resonance mode.

Figure 1.3.4 depicts the comparison of the amplitudes of cantilever deflection generated by ring down method and the resonant method. Black lines depict laser pulses.

The first experimental implementation of the resonant PTIR method was demonstrated by Lu and Belkin (Figure 1.3.5)[21]. In this setup a lock-in amplifier was used to record the amplitude of the vertical cantilever oscillations at the pulse frequency of the employed QCL. The vertical cantilever deflection signal (detected from the PSD) was transferred into a lock-in amplifier referenced by a QCL trigger signal. The pulse rate of the QCL was used as reference for the lock-in amplifier thus making pulses of the lock-in amplifier and the QCL synchronized. In resonance excitation experiments typically pulses with a length of 40 ns and repetition rate in the order of 130 kHz are used. The QCL laser power is about 100 mW. Lu and Belkin [21] estimated the temperature increase for a 300 nm thick polymer sample SU-8 to be 10 mK.
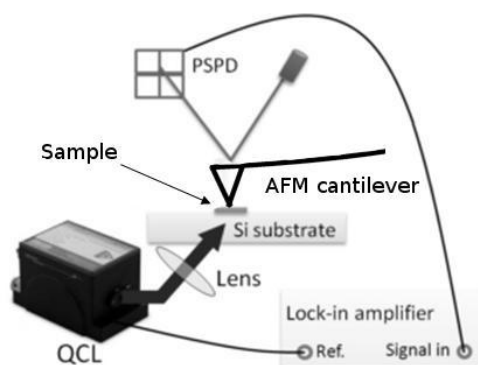
Figure 1.3.5. Illustration of the resonant PTIR scheme. Adapted from Lu and Belkin [21].

In PTIR imaging the absorption signal is recorded from the deflection signal of the AFM tip. During the raster scan of the sample however additional deflections can be induced due to changes in topography. Thus, the deflection signals caused by IR absorption and topography need to be separated. Fortunately, those deflections are located in different frequency

ranges and thus can be separately extracted from the recorded cantilever deflections. The frequencies of IR absorption deflections are related to the frequencies of the contact resonance (from 10 to 300 kHz), the frequencies of the deflections caused by topographical changes are around 1 KHz.

For the resonant excitation a laser with high repetition frequency (around 200 kHz) is required. In this regard EC-QCLs are particularly interesting sources. First of all they can be operated at repetition rates up to several hundreds of kHz. Furthermore, they are small in size, room operated and most importantly they cover the whole mid-IR spectral range.

Further the sensitivity of the PTIR method can be improved by so called tip enhanced PTIR method[23] which uses the local enhancement of the incoming laser radiation in the gap between the gold surfaces of an AFM probe and a gold substrate. Due to the increased amplitude of this enhanced electric field the PTIR signal gradually enhances as well, thus increasing the sensitivity of the PTIR method. The degree of the enhancement is associated with the so called lightning rod effect (the enhanced signal is primary localized around the metal surface and fast decays fast with the distance[32]). Tip enhanced PTIR demonstrated the ability to detect even monolayers.[23] Analogously to the principle utilized in tip enhanced Raman scattering (TERS)[33] the enhancement strongly depends on the tip sharpness and is highly sensitive to its contamination.

Resonance tracking. In case there is a drift of the contact resonance during measurement, the recorded amplitude will be affected as well. The contact resonance frequency might be shifted due to changes in mechanical properties within the sample or changes in ambient parameters during the measurements (e.g. temperature). If not corrected, such drifts will lead to erroneous results. In order to avoid these errors the laser repetition rate has to be automatically readjusted to the contact resonance during the measurement. In the first experimental implementations of resonant PTIR the laser repetition rate was adjusted manually once prior to the measurement. Recently a practical realization of the resonance tracking method was demonstrated[34,35].

1.4. Biochemical processes in cells and their characterization by mid-IR spectroscopy

IR spectroscopy can be applied for characterization of various biological systems. In this sub-chapter we discuss those biochemical processes undergoing in cellular living systems which were investigated in this thesis. Further, we highlight the capabilities of IR spectroscopy for characterization of those systems and the respective biochemical processes. We provide information on spectral features which can be used in the characterization of dead and viable cells or tissues, ischemic brain and inclusion bodies (proteins) in bacteria.

Cell death

Investigation of cell death mechanisms is an important issue in molecular biology and medical research[36]. For example, understanding of the death mechanisms allows to follow the interaction of cells with introduced stimuli, such as a drug treatment, which is of particular importance in drug transfer research[37].

Cell death can be conducted by two mechanisms – apoptosis and necrosis. During apoptosis the death of the cell is programmed (genetically determined) and triggered by the cell itself. Usually apoptosis occurs during cell aging or as a defence mechanism[38]. Apoptosis includes several stages, such as cell shrinkage, cell blebbing, phosphatidylserine exposure, nuclear condensation and DNA fragmentation[39]. Afterwards apoptotic cells are phagocytosed by macrophages or adjacent normal cells. Normally no inflammation occurs during apoptosis[38].

Necrosis is a death that occurrs due to external stress, such as thermal shock, chemical stimuli or toxic agents. During necrosis a cell undergoes certain morphological changes: cell swelling; formation of cytoplasmic vacuoles; formation of cytoplasmic blebs; disruption of the cell organelles and loss of cell membrane integrity. All those processes result in the release of the cytoplasmic contents into the surrounding tissue and are accompanied by inflammation[39].

In biomedical research discrimination between apoptosis and necrosis is of importance since it can help to elucidate the biological processes occurring within the cell towards an inducing stimuli. It is also a challenge to distinguish apoptosis from necrosis as both processes can occur independently, sequentially, or simultaneously. Sometimes even the type or the degree of stimuli inducing cell death determines how cells die. Thus, at low doses, stimuli such as heat, radiation, hypoxia and cytotoxic anticancer drugs can induce apoptosis but at higher doses the same stimuli can facilitate necrosis[38].

There are many techniques which are now routinely used to identify viable and dead dells, such as light microscopy, electron microscopy, gel electrophoresis and flow cytometry among others[40]. While most of the modern methods need tedious sample preparation and are time consuming, it is still challenging for them to discriminate different cell death modes. IR spectroscopy provides access to the main biomolecules (Figure 1.4.1). It was shown that methods of vibrational spectroscopy are highly promissing for this task [41–43].
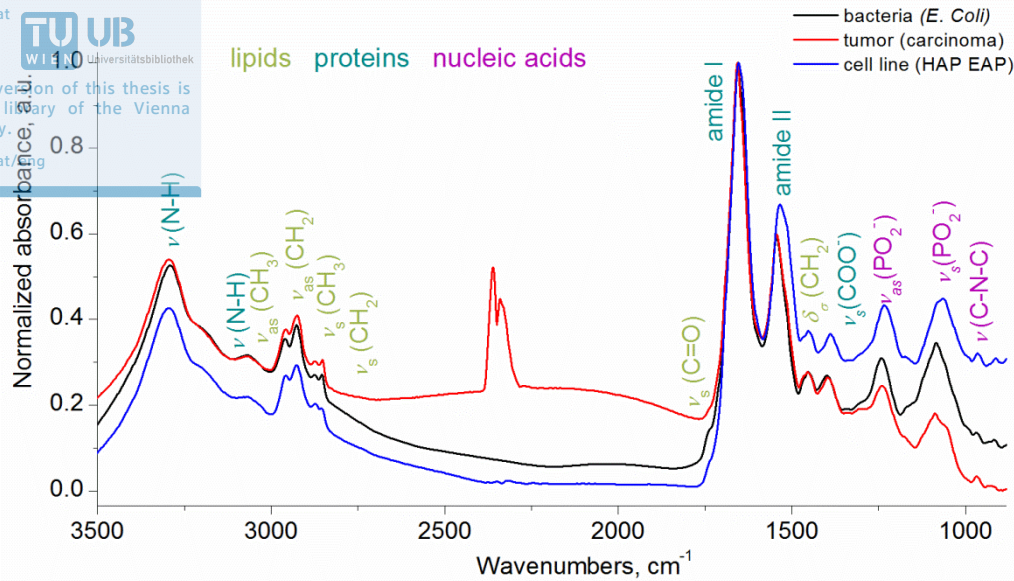
Figure 1.4.1. FTIR spectra of biological samples related to this thesis.

It was shown by a number of studies that IR spectroscopy can discriminate between viable and dead cells, besides it is capable of discriminating of apoptotic and necrotic cell lines and tissues. [41,42,44–48] Due to the strong mid-IR absorption of water, detection of cells in aqueous solution becomes difficult. Therefore, for mid-IR spectroscopic investigation of cells these are usually dried prior to analysis. It is worth to mention that it is still possible to discriminate dried cells in terms of viability.

Concerning IR spectroscopic analysis of various cell lines common features especially with respect to cell death can be identified. In general, dead cells are discriminated from viable ones by global changes in the secondary structure of proteins (Table 1.4.1). This is possible by analysing the shape of the amide I band[49].

Table 1.4.1. FTIR band assignment related to the peptide bond (proteins) and signatures of protein secondary structure. Adapted from Bukowska et al. [50].

Vibrational mode	Wavenumber, cm^{-1}	Proteins secondary structure assignment
amide I:	1695-1670	anti-parallel β-sheet, β-turns
C=O stretching	1670-1660	3$_{10}$-helix structure
N-H bending	1660-1648	α-helix structure
C-N stretching	1637-1623	β-sheet structure
amide II N-H bending C-N stretching	1580-1480	

The amide I band is mostly comprised of protein backbone signal and is commonly used in the analysis of protein secondary structure. This band is composed of sub-bands assigned to

different secondary structure elements of proteins (α-helical, β-sheet, random, turn). Second derivative spectroscopy of the amide I band region is commonly used for quantification of the protein secondary structures by following the local intensity minima.

For all cell death modes the most significant alterations are found for α-helix (1654 cm^{-1}) and parallel β-sheet (1627 cm^{-1}). In particular, increased amount of β-sheet and decreased amount of α-helical structures in dead cells was reported[42]. This is attributed to an increased amount of aggregated proteins in dead cells as opposed to viable ones.

Further, an increased amount of lipids (CH_2 and CH_3 stretches, for example at 2852 cm^{-1}) at all cell death modes comparing to viable cells was detected, too[41]. The band with a maximum around 1740 cm^{-1} is assigned to the lipid ester group. This band characterizes plasma membrane lipids. Alterations in phospholipids composition have been suggested as a possible sign of apoptosis[51] and explained by increased cellular surface area to volume ratio occurring during cell shrinkage and leading to a relative increase in phospholipid signal in the plasma membrane. Additionally, an increased peak intensity around 1743 cm^{-1} in apoptotic cells there was considered as a marker for apoptosis by other studies[42].

The changes which cellular nuclei undergo during cell death can be followed also by the absorption bands with the maximum at 1080 cm^{-1} and at 1240 cm^{-1} assigned to symmetric and asymmetric phosphate stretching, respectively. The decay of the intensity of the phosphate bands has been considered as a sign of apoptosis by several FTIR studies[42,51]. This phenomenon is related to the changes in the cell nuclei, in particular, nuclei condensation, which is an essential event in cellular apoptosis. Nuclei condensation accompanies an enormously increased concentration of DNA molecules causing a rise in its optical density of DNA related wavenumbers[52]. The decrease in the intensity of the nucleic acid band is explained by nonlinear IR light absorption or opaqueness of nuclei to IR light. Other studies also suggest that the degree of apoptosis can be quantified by the intensity of DNA related absorptions[53]. Contrary, the intensities of these DNA related absorption bands increase in case of necrotic cells. This fact is explained by the unwinding of DNA molecules. Since in necrotic cell death the DNA is unwound and not compact anymore, one might assume that the DNA is not opaque and thus "visible" to IR at this stage[41,54].

Among others few studies reported conflicting IR results on apoptotic cells, i.e. Zhou et al.[55] observed no significant changes in lipid content and an increase in the detected DNA signal. This can be explained by heterogeneous cell populations (cells were at different stages of apoptosis).

Brain research and ischemic stroke

Brain stroke is a leading disorder affecting people over the world[56]. The most frequent stroke type, brain ischemia, occurs when blood vesicles are blocked and the blood flow to the brain is reduced. This disorder might bring lethal consequences or cause various disabilities in walking and talking. Often patients who suffered from cerebral ischemia demonstrate recovery and improvements at some level. The property of the brain to recover and regain lost functions is called brain plasticity.

Currently, factors that cause brain ischemia and methods for its prevention are known but the response of brain tissue after injury is still a topic of research. Knowing the mechanism of the stroke one could suggest treatment solutions after the stroke, which are not available today.

Neural pathways consist of neuron cells connected with each other. The neuronal cell consists of a cell body and an axon which is an elongated part of the neuron cell. Axons are connected to other neuronal cells. This allows signal transition from a cell body to another neural cell. Some axons contain a myelin sheath. This is a modified insulating plasma membrane which facilitates a faster signal transfer via the action potential[57].

In brain tissue, depending on the amount of myelin in neurons different types of tissues can be differentiated such as white and gray matter. White matter contains more myelinated axons than gray matter. As myelin mainly consist of proteins and lipids white matter also contains more of these substances than gray matter. This difference can easily be seen in IR spectroscopy.

One of the possible schemes of functional brain repair after stroke is associated with neuronal modifications such as strengthening of existing neural pathways and formation of new neuronal pathways[58]. The basic concept of neuronal modification is myelination of nerve cells.

Nowadays the main methods used in stroke brain research are (functional) magnetic resonance imaging and diffusive tensor imaging [59–62]. They are powerful tools allowing non-invasive imaging. Sometimes imaging methods providing molecular specific information at a higher lateral resolution are needed. For example, by using MRI it has been demonstrated that neuronal networks reorganize and regain their lost functions.[61,63] This technique can perform imaging with a spatial resolution of about 250 µm, however, to prove the neuronal reorganisation a higher resolution is required. For that purpose histological staining methods are used in brain research [64,65]. The drawback of histological staining is that it is a time consuming procedure which gives information only for specific molecules. IR spectroscopic imaging does neither require special sample preparation nor any staining, besides it brings along simultaneous information about the presence of different molecules. Thus this technique is advantageous, although only few studies were conducted to characterize ischemic brain[66–69].

FTIR microscopy also allows visualization of molecules (markers) related to neurodegeneration. This process is characterized by alterations in levels of lipids and proteins, as well as changes in protein secondary structure. The analysis might be performed by means of univariate analysis when the related band areas are integrated and plotted for each pixel of the hyperspectral image. The images of the distribution of lipid acyl groups (v_s(CH$_2$, 2865–2845 cm^{-1})[70], lipid esters (v(CO), 1755–1715 cm^{-1})[71], protein amide I band (1700–1600cm^{-1})[72] and aggregated proteins (second-derivative intensity at 1625 cm^{-1})[73] can be successfully used to identify changes within the injured tissue, its surroundings and unaffected tissue. Remodeling of the neuronal pathways can be monitored by markers related to total lipid and protein content, since they are characteristic for myelination.

Bacteria inclusion bodies

Inclusion bodies (IBs) are submicron insoluble protein aggregates produced in recombinant bacteria. IBs are formed upon the induction of gene expression through the aggregation of polypeptide chains. The most common organism for the production of recombinant proteins is the gram-negative bacterium *Escherichia coli*[74]. Using biotechnological routes of production recombinant proteins can be produced as IBs.

IBs can be isolated from bacterial cells through mechanical cell disruption[75]. Bacterial IBs are widely used in material sciences (scaffolds in tissue engineering) and in medicine (models for amyloidosis and prion propagation; functional materials in tissue engineering; targeted and non-targeted drug delivery systems; implantable depots of therapeutic proteins)[76].

IBs formation is explained by two mechanisms: IBs might either grow from single molecules acting as nucleation sites, or smaller aggregates assemble forming larger aggregates[76]. The exact mechanism of formation of IBs is still topic of ongoing research. Bacterial IBs can be imaged with fluorescent microscopy and scanning electron microscopy (Figure 1.4.2).
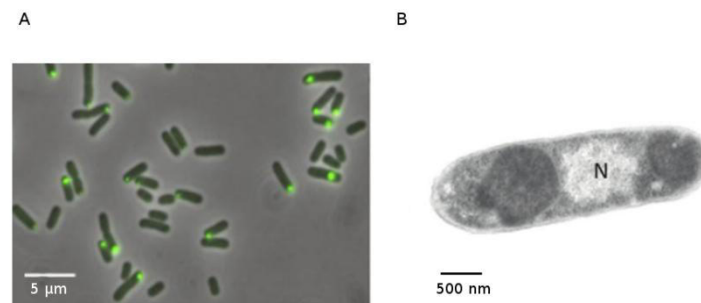

Figure 1.4.2. (A) Distribution of fluorescent IBs in *E.coli* (green). Scale bar – 5 μm.[75] (B) Transmission electron microscopy a bacterium with IBs (dark grey) areas, N – the nuclear region. Adapted from Rueda et al.[76].

Figure 1.4.2 A shows fluorescent IBs formed by a green fluorescent protein in *E. coli* (green), upon recombinant gene expression[75]. Figure 1.4.1 B shows a TEM image of an individual *E. Coli* cell with polar IBs. Dark gray color corresponds to the electrodense material.

IBs are mainly located in the polar regions of *E. coli* cells. IBs can be in both or in one pole (Figure 1.4.2). Such location of IBs is explained by macromolecular crowding in the central part of the cell where DNA is located. In other words, the middle part of the cell is too dense leaving no space for the accumulated proteins[76].

The common methods for monitoring IBs accumulation consist of IBs extraction through cell breakage and electrophoretic separation of the IBs. Those methods are time consuming and expensive.

It was demonstrated that spectroscopic techniques can be successfully applied to characterize and control the production of IBs in bacteria non-invasively[77]. In particular, FTIR spectroscopy can be successfully used for characterization of bacteria IBs[78].

Since the considered IBs consist of proteins, IR spectroscopic analysis is usually aimed to study protein content.

FTIR adds knowledge about protein folding state, but due to the limited spatial resolution individual bacteria cannot be imaged with FTIR microscopy. Characterization of IBs shape, size and structure is important for the optimization of the biotechnology processes. This motivated the analysis of bacteria containing IBs using (see section 3.3) our nanoscopic imaging technique PTIR.

1.5. Data analysis strategies

In this sub-chapter we discuss main strategies in the analysis of hyperspectral data. In general there are two approaches: univariate and multivariate. We discuss the methods that were employed in the scope of this work. Additionally, we discuss basic concepts of combined (multisensor) image analysis.

Univariate analysis

For univariate analysis a hyperspectral image that consists of a spectrum at each pixel is visualized in a form of a false color map. This map shows the intensity at a selected wavelength. Not only single wavelengths can be visualized but also their combination, such as integrated band, bands ratio etc. Univariate analysis is also commonly used for side by side analysis, when the spatial distribution of different analytes (molecules) is compared. Univariate analysis can be easily interpreted, but it also may discard useful spectral information. To extract the useful information from the whole spectrum multivariate methods are employed.

Multivariate analysis

Unlike univariate analysis, multivariate analysis derives information from the entire spectrum, thus, delivering extended information about sample properties. However, the analysis of a set of multidimentional spectra, such as mid-IR spectra, might be challenging since every spectrum consists of a number of variables (wavenumbers). Some variables carry unrelated information (e.g. noise, where sample has no absorption). Besides, frequently the change in values of one variable (absorbance) correlates with the change in others (e.g. a functional group having two IR-active bonds such as $\nu(C=O)$ and $\delta(N-H)$ in the amide biond). Multivariate analysis uses statistical methods to enable a more thorough interpretation of the complex data by means of extracting the useful information and leaving out less relevant information. For that a number of strategies exist. Depending on the analytical task different methods can be employed. In this subchapter we discuss the multivariate methods relevant to this thesis.

Principal component analysis

Principal component analysis (PCA) is a common statistical technique that rearranges complex datasets for an easier interpretation and extraction of important information. Multidimentional datasets, in particular IR spectra, frequently have variables which depend on each other, thus carry redundant information. PCA reduces the dimensionality of a dataset and eliminates correlated variables by projecting dataset onto a new space with a lower number of dimensions.

In the PCA data is represented as an array in a *m*-dimensional variable coordinate system. First, the center of this cloud is to be found. This center will be the origin of a new system of coordinates. Then, the direction of the largest variations is chosen. This direction is called the first principal component (PC1). Then a new direction which accounts for the maximum

of the remaining variation orthogonal to the previous PC is calculated. This direction will be the second principal component PC2. The process of the choosing the PCs proceeds until all variation in the dataset is described. As the relevant information is concentrated in the first PCs it is common practice in PCA to neglect PCs of higher order in further data analysis. In other words, PCA performs rotation of the axes of the original variable coordinate system to a new orthogonal coordinate system whose axes (PCs) match with directions of maximum variation in the original coordinate system.

This new orthogonal coordinate system is constructed of new uncorrelated variables (PCs). As a result, multidimensional spectral data is represented in a new dataset with a reduced number of variables (PCs).

Assume that we have a dataset which is a matrix X with n rows (number of samples or spectra) and m columns (number of variables or wavenumbers). In PCA X will be decomposed into a scores matrix T and a loadings matrix V and an error matrix E, which contains the unexplained variance:
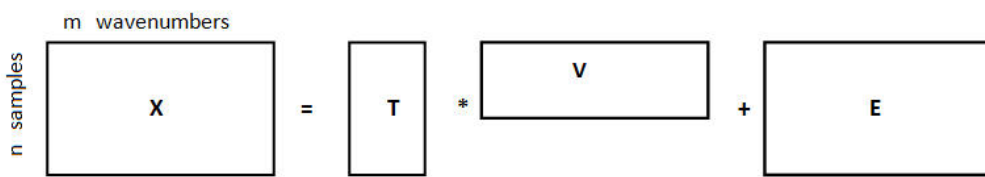
$$X = TV^t + E \qquad (1.28)$$

Figure 1.5.1. Demonstration of the PCA principle. X is the data matrix, which is decomposed into a matrix of scores (T) and a matrix of loadings (V). E is an error matrix which contains unexplained variance (E).

Matrix V contains the so called loading vectors. These have dimension of the original spatra and describe the location (direction) of the new coordinate axis (PC) in the space of the original data matrix X. Matrix T contains the so called score values. These values indicate the relevance (importance) a given loading vector has in the reproduction of a given original spectrum. In V the loading vectors (v) are sorted by their importance, expressed as their eigenvalue. The number of PCs to be calculated is defined according to the "Kaiser" criterion [79,80]. According to this method only PCs exhibiting eigenvalues larger than one can be included into the analysis.

Unsupervised classification

K-means clustering

Clustering algorithms classify spectra into groups by minimizing differences within groups and maximizing differences between groups. This classification can be used for segmentation of hyperspectral images[81].

The iterative k-means clustering algorithm performs unsupervised sorting of spectra with similar spectral features. Spectra assigned to different clusters express different spectral signatures whereas spectra of one cluster are similar to each other. In this method an individual spectrum is represented as a point in an m-dimensional space, where m is equal to the number of variables (data points in a spectrum). In this space k points corresponding to the origin of the related clusters are selected. Before the k-means clustering is performed the number of clusters (k) should be selected. K is jointly defined according to a particular sample (e.g. the number of tissue types of interest) and supported with the "Kaiser" criterion[79,80] and the "Elbow" method[82,83]. The "Kaiser" criterion suggests to define the number of clusters according to the number of principal components (PCs) possessing eigenvalues larger than one. In the "Elbow" method the error sum of squares is plotted against various k. The number after which the curve starts flatten is related to the correct value of k. Further, distances between the selected k points and the spectra are calculated. The spectra nearest to a cluster (distance between them and a k point is minimum) are assigned to the related cluster. Then, for each cluster a centroid (centre of a cluster) is calculated, then the distance between centroids and samples are recalculated. If a sample is not the closest to the associated centroid, the sample will be assigned to the cluster with the nearest centroid. The locations of centroids are recalculated every time when a sample was assigned to a new cluster. The procedure repeats until the samples do not change their cluster membership[84].

In other words, k-means clustering algorithm sorts spectra in such a way that the intra-cluster variance minimal and inter-cluster variance is maximal. It is a rigid method which assigns an individual spetrum only to one class. Other methods such as fuzzy clustering are less crisp and might assign a spectrum to more than one cluster.

In cluster image analysis a distinct color is assigned to all samples of one cluster. Since every sample has its own spatial coordinate in the hyperspectral map, those colored samples provide a false color cluster image of the sample. Mean spectra corresponding to each cluster can be calculated and used to interpret the spectral differences between the clusters.

Supervised classification

Multivariate analysis includes methods that allow supervised learning. Such methods are usually classification techniques. Using classification models unkown samples can be characterized. Typically, prior to the classification a training dataset containing data (spectra) is generated. Afterwards a classification model (classifier) on a basis of the training dataset is calculated. The performance of the classifier is checked on a validation dataset. Further this model can be applied to a new sample. The models can be calculated with different methods. In this chapter we discuss the most common approaches for classification of hyperspectral images – partial least squares discriminant analysis (PLS-DA) and random decision forest (RDF).

The performance of a classification model can be described by a confusion matrix (Figure 1.5.2). The matrix consists of number of true-positives (green dots, in the upper left corner);

false-positives (red crosses in the upper right corner); false-negatives (red crosses in the lower left corner); and true-negatives (gray dots in the lower right corner).
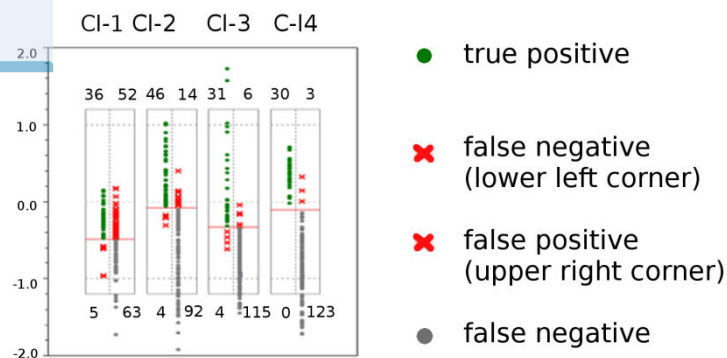

Figure 1.5.2. Illustration of a typical result of a classification model – a classification matrix with the number of true positive, false negative, false positive and false negative samples.

Partial least squares discriminant analysis

Partial least squares-discriminant analysis (PLS-DA) is a supervised method for classification of samples in a dataset. If a sample consists of two groups (classes A and B), PLS-DA can be considered as a linear two-class classifier. In this case the method tries to find a straight line that divides the sample space in two parts. PLS-DA searches this discriminator (separator) function. For many groups this separator function represents a hyperplane in multidimensional space [85].

PLS finds relation between two matrices: so called X data matrix, consisting of n samples containing m experimental measurements (e.g. number of wavenumbers in a spectrum) and a c vector consisting of n elements. Each element has a numerical label for each sample according to its group membership. PLS-DA derives a regression model between X and c [85]. PLS-DA represents X and c with the following equations:

$$\begin{cases} X = T\,P + E \\ c = T\,q + f \end{cases} \tag{1.29}$$

where T – score matrix; P – loading matrix and q – loadings vector; E – residual matrix and f – residual vector. When a PLS algorithm is applied to the X and c a prediction (classification) model is built. Here we consider a classification of a dataset containing only two classes (A and B), the related algorithm for that is referred to as PLS1. This algorithm can be extended in case of classification of more than two groups in a sample and is then referred to as PLS2. Typically PLS1 algorithm calculates PLS weight vector w, PLS scores T, X loadings p, c loading q and residual data matrices and vector for X and c, respectively. [85]

A built PLS-DA model can predict the values of c in the original data and in a new dataset containing unknown samples. X will be related with c as follows:

$$c = Xb + f = Tq + f \tag{1.30}$$

where b is a regression coefficient vector.

46

Unknown sample value of $\hat{c}$ would be defined as:

$$\hat{c} = xb \tag{1.31}$$

The value of b is defined by:

$$b = W(PW)^{-1}q \tag{1.32}$$

where W is a matrix containing weight vectors of the PLS components.

The $\hat{c}$ value determines to which particular class belongs a sample. In the simplest case a dataset containing only two classes, if $\hat{c}$ is above 0, then the sample is assigned to class A; otherwise - to class B.

The performance of PLS model is usually estimated by cross-validation (CV). For that the dataset is split into two subsets: a training set and a validation set. The calculated model based on the training dataset is used to predict $\hat{c}$ values in the validation set. By averaging over several splits the model performance is estimated. The performance of PLS-DA classification model can also be characterized by calculating the root mean square error of prediction (RMSEP).

Random decision forest

Random decision forest (RDF) or random forest is a machine learning technique that combines a number of decision trees and forms a forest for classification analysis. RDF uses a decision tree as a predictive model. Each decision tree is built on a unique sub-set of the training data. Those sub-sets are picked randomly from the training dataset. Thus, all trees in the forest are independent and do not correlate A decision tree depicts in a way of a diagram the possible outcomes from a series of decisions (Figure 1.5.3)[86].
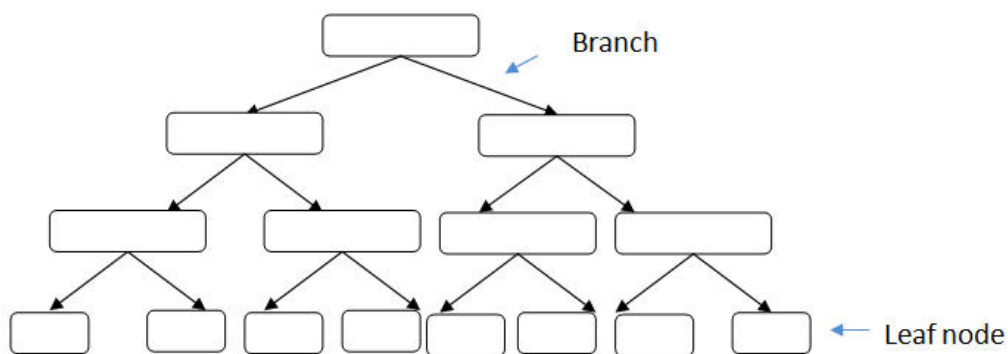
Figure 1.5.3. A basic scheme of a decision tree.

A decision tree receives an input vector (e.g. a spectrum) and splits it into attributes (features). Each decision tree represents a structure consisting of nodes and branches. Each leaf node represents a decision which was made after computing all attributes. To each tree a model that describes the characteristics of an input feature is related. When a new object is classified the input vector is applied to each decision tree in the forest. The forest chooses the classification that has the most votes among the classifications that are suggested by

each tree. Such analysis of independent decisions significantly reduces the risk of over-fitting[86].

The performance of a RDF model is usually characterized by the average of the training and the out-of-bag (OOB) error estimates or by the average classification error (AvCE). During the construction of a RDF, the percentage of variables used to build the individual trees can be chosen. The number of trees can be set as well. Classification results can be analyzed regarding the importance of the variables introduced to the models[86].

Multisensor image analysis

With the current development of modern analytical imaging techniques, the combined image analysis becomes desirable, since it is often difficult to characterize a chemical composition using a single imaging technique. For that purpose several multimodal analytical approaches were introduced.[87–89] However, those techniques primarily combine different modalities of one technique (eg. different modalities of vibrational spectroscopy [87,89]). It could be of interest to perform a combined analysis of data from different techniques such as SEM, EDX, FTIR, Raman, MS spectrometries. The combination of two or more complimentary techniques can be performed in terms of multisensor (combined) image analysis[88]. This method allows combination of complementary chemical imaging techniques applied to one and the same sample. This technique offers information for sample characterization that is not accessible by a single technique or a side-by-side analysis. The implementation of multisensor image analysis in the software package ImageLab (Epina, Austria) allows a user friendly execution of this new way of data analysis. It allows import, data fusion and chemometric analysis of arbitrary hyperspectral datasets.

To analyze the different spectral images of the same sample, the corresponding single datacubes have to be fused to an overall multisensor hyperspectral dataset. This procedure is discussed elsewhere in detail. [6,88] First, individual datasets should be separately aligned to the same reference image (visible light microscopic image). Then common (anchor) points are defined on the distinct areas of a reference image and a voxel image. Precisely defined anchor points facilitate an accurate alignment of data sets. Using the defined anchor points a dataset is aligned via a linear affine transformation (automatically performed in the Imagelab software package). Secondly, the aligned datasets have to be merged. Finally, a new hyperspectral cube is created which consists of appended voxels of different data sets.

Spectral descriptors concept

Multisensor image analysis allows the multivariate interpretation of the data. The raw data is replaced with so called spectral descriptors (SPDCs) [88] that extract meaningful information from the data. SPDCs solve the problem of the curse of dimensionality in multidimensional datasets and structure the data. Analysis by means of SPDCs facilitates an improved statistical analysis and faster calculations.

Depending on the type of spectral data different types of SPDCs can be introduced. For FTIR spectroscopic image analysis of biological samples commonly used SPDCs related to peak

intensities, peak areas; peak or bands ratios. These can also be calculated from first or second derivatives of the original data. Figure 1.5.4 illustrates the definition of the types of SPDCs used for the multivariate analysis of IR-spectra in this thesis.
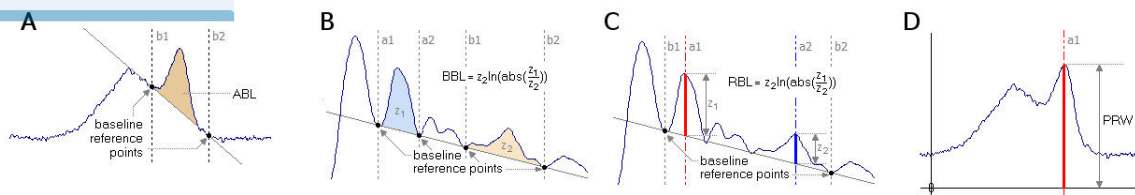

Figure 1.5.4. The types SPDCs used for the analysis in this thesis. A – band area with subtracted baseline, B – band ratios, C – peak ratios, D – peak intensity. Adapted from the ImageLab software.

SPDCs describing changes in band intensities, band ratios (Figure 1.5.4 A-C) and are used to describe changes FTIR spectra of biological samples. SPDCs describing changes in MS spectra are rather simple – peak intensity (Figure 1.5.4D). The choice of the analysed bands and the set of SPDCs are defined according to the spectral properties of a particular sample (for examples see publications II and III).

SPDCs can be used both for univariate und multivariate analysis. For univatiate analysis a SPDC is applied to the dataset and a false color chemical image is generated. In multivariate analysis several SPDCs are used for data analysis. In case of multisensor analysis the number of variables will be equal to the sum of SPDCs selected from the combined techniques.

Hierarchical cluster analysis of PCA loadings

Hierarchical cluster analysis of PCA loadings (HCA of the PCA loadings) is a method that allows visualizing and determination of the correlated variables. HCA of the selected eigenvector loadings of the PCA can be calculated in defined m-dimensional space, where m is the number of the selected PCs. Figure 1.5.5 illustrates the principle of HCA of the PCA loadings.
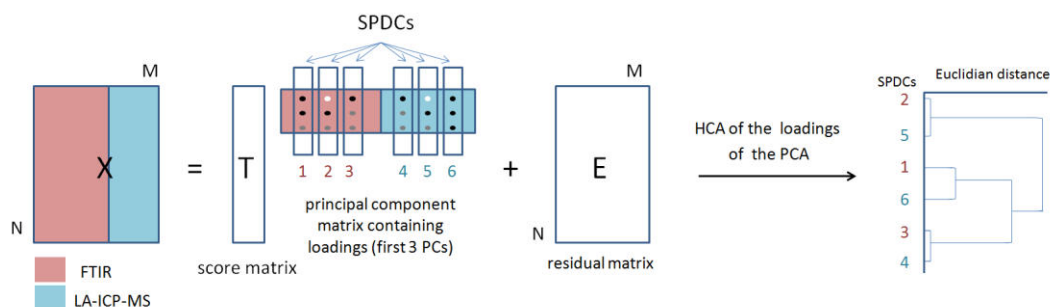
Figure 1.5.5. Hierarchical cluster analysis of the PCA loadings. Reproduced from permission Balbekova et al.[90]

The correlation of variables is demonstrated by the related dendrogram. Horizontal lines on the dendrogram show the similarity between the SPDCs expressed in the Euclidian distance

between them in the loadings of the PCs space. Small values of Euclidian distance are related to high correlation between SPDCs and vice versa.

This method is useful when applied to the multisensor image analysis for identification of chemical compounds and correlation in spatial distribution of the different components.

This approach was applied for the combined analysis when different datasets were merged and analysed (Publication II).

1.6. State of the art biomedical applications and challenges of mid-IR spectroscopic imaging

In this sub-chapter we discuss current trends and achievements in far- and near- field mid-IR spectroscopic imaging in the context of biological samples.

FTIR spectroscopic imaging

Since decades FTIR spectroscopic imaging has been applied to discriminate biochemically different regions in thin tissue sections and has demonstrated its potential in histopathological diagnosis. Results of FTIR imaging of histological tissue sections have been compared with standard imaging approaches based on Hematoxylin and Erosin (HE) histological staining.[81,91–93]

FTIR imaging found applications in identification and characterization of various biochemical processes, related to biomedical research, such as pathological changes in brain tissues[94], tumor malignancy[95,96] as well as identification of tumor and non-tumor tissues[97,98]. In the following relevant work in the field of brain imaging and imaging involved in tumor research are given.

Changes in brains occurred during the development of glioma tumors were studied by Amharref et al.[99] Tumors were successfully discriminated from healthy tissues with the help of multivariate statistical analysis. The results demonstrated good agreement with histological staining results and additionally it was shown that FTIR imaging allowed early detection of pathological changes in tissue. Further, FTIR imaging was used to study changes in brain after implantation and development of glioma tumor. The study suggested using FTIR imaging for differentiation and classification of tumors based on collagen content. Various tissue types (healthy brain, solid and diffuse tumor) were classified according to the collagen content and protein secondary structure profile by means of multivariate statistical analysis.[100] Petibois et al. demonstrated accurate discrimination between healthy and cerebral tumor areas by means of FTIR spectral imaging. FTIR spectroscopy identified several cancer markers based on molecules (carbohydrates, lipids, proteins) and molecular structure information of protein secondary structure and fatty acyl chain peroxidation level.[44]

D'inca et al.[101] used FTIR microspectroscopy to study tumor viability for evaluation of anticancer therapy of a model organism (rabbit). The treated liver tumors were automatically characterized and quantified by means of *k*-means clustering followed by principal component analysis (PCA) and linear discriminant analysis (LDA). Using the *k*-means clustering of control or treated tumors a database of different tissue FTIR spectra was created. Using this reference library, the PCA-LDA predictive models were built. Using those models tumor viability on unknown tissue sections could be identified and quantified automatically. The results of this quantification agreed well with the related results of histological staining.

A similar approach was performed Gazi et al..[102] The authors assessed the grade and stage of prostate cancer histological samples by FTIR microspectroscopy combined with LDA. The performance of the developed diagnostic classifier demonstrated 80% agreement of FTIR-LDA grade to histology. Those authors also adopted Time-of-Flight Secondary Ion Mass Spectrometry (TOF-SIMS) imaging of prostate cancer cells, however no combined (multisensor) analysis was performed.

Wald et al. investigated histological samples of patients with the non-metastatic and metastatic melanoma cells. The samples were imaged with FTIR spectroscopy and analysed using multivariate analysis. According to the results different cell types were discriminated by IR spectral features that are unique for every type of the cells. Automated identification of the cells was obtained using a supervised PLS-DA model. The results of this analysis proofed to be similar in sensitivity and specificity as immunohistochemistry.[103]

PTIR spectroscopic imaging

Baldassarre et al. demonstrated a linear dependence of the PTIR signal on the sample thickness using a polymer as a model sample. This dependence correlates with the theoretical model that describes thermal expansion of the sample below the scanning probe. The authors also demonstrated protein distribution in single mammalian cells via mapping of the PTIR signal at 1660 cm^{-1} related to the amide I band. Further, in this study they investigated *E. coli* bacteria containing expressed proteins as inclusion bodies (IBs). In *E. Coli* bacteria with IBs topographical changes were observed and those changes correlated well with the strength of the amide I signal.[3]

Amenabar et al. presented work where mapping of individual protein complexes with 30 nm lateral resolution was performed by the sSNOM technique. This work demonstrated spectra of a virus, ferritin complexes, purple membranes and insulin aggregates in the spectral range of the amide I and II bands. Those samples were interpreted in terms of their protein secondary structure.[104]

Giliberti et al. used the PTIR technique to map the spatial distribution of proteins in HeLa cells which were exposed to oxidative stress. The results indicated that due to stress protein clustering occurred within cytoplasm, as the nuclei region provided a weaker amide I signal than the cytoplasm.

Statistical analysis of the protein distribution showed that the probability to find protein clusters in the cytoplasm of the stressed cells is higher than in the control cells.[4]

Ruggeri et al. characterized aggregation of individual Josephin amyloids (insoluble protein fibril aggregates) at the nanoscale. Through the conformational changes in proteins the oligomeric and fibrillar species produced during the amyloid aggregation were differentiated. The results suggested that the mechanism of aggregation starts with the monomer leading native structured spheroidal intermediates. These intermediates evolved into misfolded aggregates and into the final fibrils.[105,106]

Recently Jin et al. applied the PTIR technique to image a PMMA polymer immersed in heavy water. The authors reported that the employed technique preserves sensitivity and spatial resolution. The suggested method overcomes challenges caused by water absorption and

scattering, as well as mechanical damping of cantilever vibrations. The authors demonstrated spectroscopy and imaging of a 20 to 50 nm thick polymer with a 25-nm spatial resolution in the amide I and II spectral regions.[107]

Berweger et al. performed spectral imaging of a dried purple membrane (a part of cytoplasmic membrane in microorganisms) with infrared sSNOM nanoscoscopy. Imaging was performed using near-field spectral phase contrast based on the Amide I band. According to the results the protein distribution was imaged with 20 nm spatial resolution.[108]

Kennedy et al. quantified biochemical heterogeneity in human epithelial cancer cells using the PTIR technique. The PTIR chemical and topographic images were combined to enhance the image clarity thus localizing the nucleus. Further, the combined topographic analysis gave insight into chemical heterogeneity of mammalian cancer cells at the nanoscale.[109]

Amenabar et al. for the first time demonstrated hyperspectral infrared nanoimaging with a tunable bandwidth-limited laser continuum by means of sSNOM. Hyperspectral IR mages consisting of around 5,000 pixel, each pixel containing a spectrum in the range from 1,000 to 1,900 cm[1] were registered in less than 8 hours. A polymer blend and a melanin granule in a human hair cross-section were imaged with a spatial resolution around 30 nm and multivariate data analysis was applied.[110]

It was previously reported in literature that IR spectroscopy is capable of discrimination between viable and apoptotic cells, but imaging of individual apoptotic cells was not performed so far. By producing high-resolution images of biological systems PTIR technique could potentially facilitate a deeper understanding of the different processes occuring during cellular death.

Combined image analysis

Combined data analysis can be carried out in different ways. Often data from a given technique is analysed and then only the obtained images are compared. In multimodal or multisensor analysis attempts are made to merge the data from the different techniques prior to chemometrical (multivariate) analysis. Often the wording multimodal analysis is used in this respect. As very often such analysis concerns the use of different modalities of a given technique (IR and Raman as modalities of vibrational spectroscopy) the concept of multisensory imaging was introduced, too. Multisensor imaging refers to the use of imaging techniques providing different information (elemental vs molecular).

Perez-Guaita et al. merged FTIR and Raman imaging data by adjusting the same spatial resolution. The authors investigated red blood cells and a desmid microalgal species. The combination of the two techniques provided complementary information not evident in the analysis of the individual images. The assignment of some FTIR bands was only possible by correlating with the Raman spectra. Additionally, the correlation of the Raman and FTIR spectra was defined by statistical heterospectroscopy. This method allowed the assignment of overlapping lipid and carbohydrate bands.[111]

Lasch et al. introduced two-dimensional correlation spectroscopy for joint analysis of hyperspectral data acquired from hamster brain tissue using FTIR microspectroscopy, Raman

microspectroscopy and matrix-assisted laser desorption ionization time-of-flight mass spectrometry. Such hyperspectral image analysis also allowed additional spectral band assignments.[112] Combined multivariate analysis was demonstrated by Ofner et al..[113] The authors also analysed tumor cells via different imaging methods (Raman spectroscopy, secondary ion mass spectrometry and energy dispersive X-ray spectroscopy) and found statistical correlation between spatial distribution of chemical elements and molecules. Such multisensor (combined) analysis is a universal approach as it is possible to combine different imaging techniques. The combined multivariate analysis using FTIR and LA-ICP-MS imaging data was however not shown before.

Chapter 2

II.   Materials and methods

This chapter describes sample preparation, provides details and parameters of the measurements as well as information on data processing steps that were performed throughout the work.

2.1. Sample preparation

The analysed substances (samples) were deposited either on CaF_2 (Sigma Aldrich), silicon wafers (CrysTec GmbH, Germany) (for FTIR measurements), or glass slides coated with a few micrometrs gold layer (for PTIR measurements). Prior to sample deposition, substrates were cleaned through successive rinsing in acetone, ethanol and ultrapure Milli-Q water.

Poly-L-lysine thin film

Poly-L-lysine (PLL) hydrobromide Molecular weight 15.000–30.000 (Sigma Aldrich) films were prepared using spin-coating. An aqueous solution of PLL with concentration 4.6 % (w/v) was casted (3 µl) at the spinning CaF_2 substrate with a rotation speed of 1500 rpm. The rotation time was set to 1 minute. Afterwards, the sample film was dried under ambient conditions for several hours.

Polystyrene thin films

Polystyrene (PS) purity ~280kDa, Molecular weight ~280,000 was purchased from Sigma Aldrich. PS thin films were prepared by spin-coating. One drop (3µl) of a PS solution in toluene (0.4 % w/v) was casted at a spinning substrate (CaF_2 or gold) with a rotation speed of 1500 rpm. The rotation time was set to 1 minute. Eventually the substrate was dried under ambient conditions. The thickness of the film was characterized by AFM after a part of the polymer film was removed from the substrate by a slight scratch of a toothpick stick.

Bacteria with inclusion bodies

Recombinant protein (horseradish peroxidase, HRP) was produced in a host organism - *Escherichia coli* (*E. coli*) in the group of Prof. Herwig (TU Wien, Institute for biotechnology). In this process, HRP is produced in cytoplasmic inclusion bodies (IBs)[114]. Further, control samples (*E. coli* bacteria without IBs) were cultivated. Prior to analysis, the bacteria were washed in 0.9 % NaCl aqueous solution and the culture medium was removed by centrifugation at 1000 revolutions per minute. Afterwards, the obtained bacteria pellets of IB-samples and control) were spotted on CaF_2 and gold substrates and dried over three hours under ambient conditions.

HAP1 cell lines

HAP1 cell cultures (kindly provided by Prof. Rothender, Max F. Perutz Laboratories, Vienna) were harvested on gold and CaF_2 substrates, washed with 0.9% NaCl solution in ultrapure

Milli-Q water and dried under ambient conditions. Two groups of cells were produced: cells incubated with Puromycin during 24 hours and control cells, which were not treated with the drug. Fluorescence-activated cell sorting (FACS) flow cytometry confirmed that in the drug treated cells apoptosis was induced.

Tumor thin sections

A group of 8-week-old female Balb/C mice (National Oncology Institute, Budapest) were injected subcutaneously with the tumor cells (C26 mouse colon adenocarcinoma (Eppelheim, Germany)). The mice were treated with Sunitinib (LC Laboratories, USA) for 7 days after tumor cell injection. The treatment was performed orally with a feeding tube once daily (during 11 and 17 days) at a dose of 80 mg/kg. With the last dosage of Sunitinib, the mice received also cisplatin (Accord Healthcare, GB) intraperitoneally at a dose of 10 mg/kg. Three hours after the last treatment, the mice were sacrificed. Tumors were extracted from the animals and snap frozen by submerging the tissues into dry-ice cooled isopentane.

Cryo-cut sections of tumor tissue with thicknesses of 10 μm were deposited on silicon wafers (CrysTec GmbH, Germany). Silicon substrates were surface modified with (3-aminopropyl)-triethoxysilane in order to optimize adhesion of the tissue section.

Ischemic rat brains thin sections

Photothrombotic stroke was induced in 11-week old male adult Sprague Dawley rats (Charles River, Germany) according to the common protocols.[115] The stroke was located in the right sensorimotor cortex. One week after the stroke, the rats were sacrificed. Their brains were extracted, embedded in paraffin and sectioned with a microtome. The investigated samples – coronal thin sections (thickness: 5 μm) – were taken at different regions (distances from bregma): bregma-0.2 mm (sample 1) and bregma −0.8 mm (sample 2). The samples were deposited on IR-reflecting glass substrates (Kevley Technologies, USA). The tissue sections were deparaffinized using xylene and isopropanol (95%)[115].

2.2. FTIR spectroscopy and spectroscopic imaging

FTIR measurements were performed using a Bruker Hyperion 3000 microscope equipped with a liquid nitrogen cooled single-point MCT and MCT-FPA detector (64x64 pixels) which is connected to a Bruker Tensor 37 FTIR spectrometer. For FTIR microscopy measurements in transmission and reflection, a 15x Cassegrain objective with a numerical aperture of 0.4 was used. Details of spectroscopic imaging of tumor samples are given in Publication II. Spectra were recorded in transmission mode in the range of 3850 to 900 cm^{-1} (2.6 to 11 μm) with 4 cm^{-1} spectral resolution. Depending on the sample characteristics, 64 or 128 scans were averaged to obtain one single beam spectrum. The influence of atmospheric water vapor on the spectra was minimized by purging the system with dry air. Background spectra were acquired of the pure substrate by coadding 128 scans. For data analysis the software package OPUS 7.2 (Bruker, Ettlingen, Germany) was used.

2.3. PTIR spectroscopy and spectroscopic imaging

Experimental setup 1

The working principle of the setup based on the resonance enhanced PTIR technique is similar to the one described in chapter 1.1. As depicted in Figure 2.1, a Daylight Solutions EC-QCL with a peak power of approx. 800 mW and a tuning range of $1720 - 1565$ cm^{-1} was employed as a light source. As a scanning probe microscope, an Agilent 5400 AFM was employed. Through an optical system consisting of multiple gold mirrors, the laser beam was directed from the laser to the AFM sample stage below the AFM cantilever at an incident angle of approx. 77°. A beam expander was inserted into the optical system to reduce the divergence of the beam upon the oblique incidence. The beam expander was built of two different parabolic mirrors (2" and 6" reflected focal length). Finally, the IR beam was focused on the sample using an off-axis parabolic mirror. Three linear translation stages were used to change the position of the focused laser spot on the sample in three dimensions independently. The sketch of the setup is displayed in Figure 2.1.
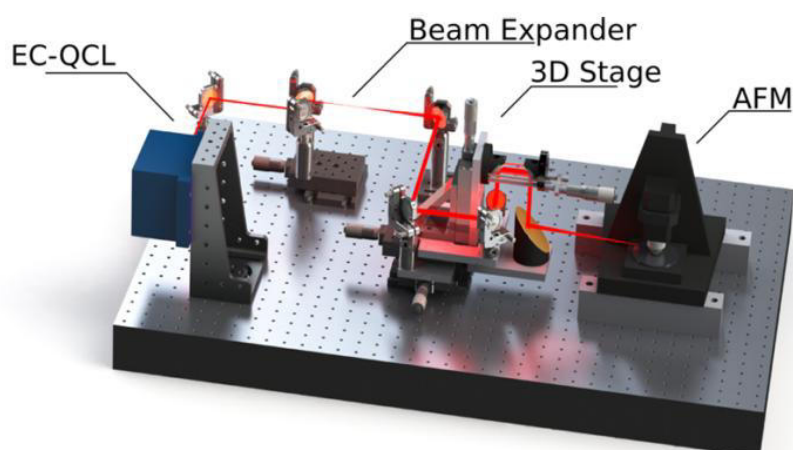

Figure 2.1. Sketch of the optical setup used PTIR measurements. The IR laser beam is shown in red. Reproduced from permission Ramer et al. [116].

The instrument was set up in a housing consisting of polyethylene foil which was flushed with dry air to reduce the influence of water vapor on the laser intensity. Further, the setup was placed onto a vibration isolation table to reduce the mechanical noise during the measurements.

In this work, AFM cantilevers with overall gold coating (Budget sensors, ContGB-G, resonance frequency 13 kHz and force constant 0.2 N/m) were used. Gold coating excludes absorption of laser light in the AFM cantilever and facilitates enhancement of the localized electric field.

The PTIR signal was split from the detected AFM deflection signal (caused by changes in topography) by means of the lock-in amplifier that is incorporated in the AFM electronics. To

achieve that, a sophisticated electronics setup (consisting of the AFM-MAC III box and an analog digital converter)[116] was developed. These electronics allowed triggering the EC-QCL emission at a particular frequency corresponding to the frequency of the lock-in amplifier. Thus, the PTIR signal encoded at a particular frequency was filtered from the AFM lock-in signal.

In order to achieve the highest signal in resonance enhanced PTIR spectroscopy, the laser repetition rate has to be repeatedly readjusted to the contact resonance (mechanical resonance) of the cantilever. In the experimental setup 1, this readjustment was performed as follows. First, the amplitude of the cantilever deflection was recorded for a range of frequencies (repetition rates) close to the expected position of the contact resonance. Then, the repetition rate was defined according to the maximum amplitude and was used for the subsequent measurements.

The time-resolved measurements were performed using the experimental setup 1. In this experiment, the frequency of the contact resonance was very unstable due to the temperature changes; the repetition rate was defined prior to recording of each spectrum. For more detailed description of the setup see Publication I[116].

Experimental setup 2

In the experimental setup 2, the light source was replaced with another EC-QCL (MIRcat, Daylight Solutions). The MIRcat contains four laser chips that emit at tuning ranges of 889–1766 cm^{-1} and 2770–2932 cm^{-1}. The laser power spectrum is given in Figure 2.2.
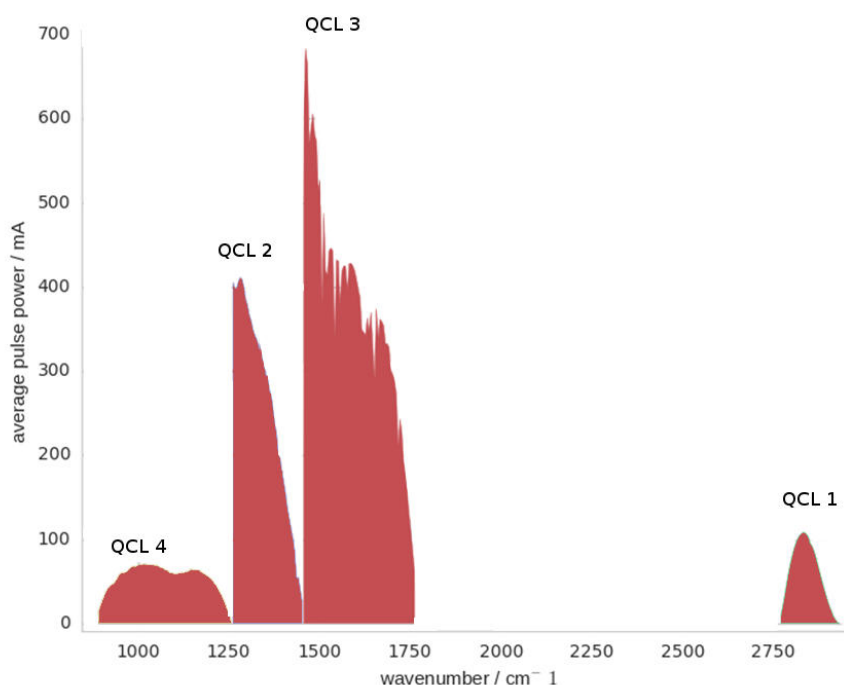

Figure 2.2. EC-QCL MIRcat laser power spectrum.

In the PTIR setup 2, the same AFM was used as in the experimental setup 1. The optical setup was slightly modified. The focusing parabolic mirror was replaced and the beam

expander was removed. Furthermore, the angle of the incident light was set to 65°. Additionally, there was implemented an electronic controller that allows resonance tracking by means of automated adjustment of the laser repetition rate according to the position of the mechanical resonance of the cantilever. This adjustment can be achieved during the measurement, which was not possible in the setup 1.

The realized resonance tracking system works as follows. First, the repetition rate of the laser is swept close to the resonance frequency (across several tens of kilohertz). Throughout this frequency sweep, the cantilever deflection amplitude related to each frequency is recorded. Finally, the maximum amplitude is sent to the controller. Thus, for each frequency sweep the maximum amplitude is recorded and exported via a digital analog converter.

For the resonance frequency tracking routine, the following input settings are required: frequency step size, frequency starting point, sweep speed, sweep direction. The detailed description of the working principle of controller electronics is given in refs[34,35].

Experimental parameters

For PTIR measurements with experimental setup 2, the following experimental parameters were used. The PTIR measurements were performed after that the AFM tip was set in contact with a sample. I and P gain parameters that determine how quickly the feedback system reacts to changes in deflection were both set to 2%. PTIR chemical imaging was performed at a resolution of 128 points per line with a speed of 0.1-0.5 lines per second (ln/s), depending on the size of the scanned area. In order to adjust to the resonance frequency, the following command was used in the custom made controller system:

$$120E6/start\_sweep(f_{start}, f_{end}, n, t)$$

where f_{start} and f_{end} are denoted in Hz, n is the number of the steps and t describes the time between steps. f_{start} and f_{end} were adjusted according to the position of the contact resonance; n was varying from 100 to 250 depending on the frequency range; t was varied from 4 to 12 depending on the type of measurement: fast (spectroscopic measurements) and slow (chemical mapping). For fast measurements, t was set to low values, and vice versa.

A series of PTIR spectra (five subsequent spectra) were recorded at each position. The acquired spectra were averaged and the standard deviation was calculated. Calculations were performed in Matlab (2013b) using a custom-written code.

2.4. LA-ICP-MS imaging

Laser ablation-inductively coupled plasma-mass spectrometry (LA-ICP-MS) is an analytical technique that allows detection of trace elements in a sample through the decomposition of molecules into respective atoms and detection of their masses. LA-ICP-MS uses a pulsed laser that is focused on the sample. The sample material vaporizes upon laser ablation. The resultant vapour (transferred through a gas stream) is ionized by means of high temperature plasma. The ionized atoms of the sample are detected by a mass spectrometer. The high

sensitivity (below μg g^{-1} level for metallic analytes) of LA-ICP-MS allows investigations of trace elements in biological tissues.

In this work, LA-ICP-MS was used for microscopic imaging of tumor and ischemic brain thin sections. For LA-ICP-MS measurements, a laser ablation system (New Wave 213, ESI, Fremont, CA) equipped with a frequency quintupled Nd:YAG laser and a fast-washout ablation cell was used. The laser ablation system was connected to a quadrupole ICP-MS system (iCAPQc, ThermoFisher Scientific, Germany) through a polytetrafluoroethylene tubing. Helium was used as ablation gas. The following isotopes were monitored: ^{13}C, ^{23}Na, ^{24}Mg, ^{25}Mg, ^{31}P, ^{34}S, ^{39}K, ^{55}Mn, ^{56}Fe, ^{57}Fe, ^{58}Ni, ^{60}Ni, ^{63}Cu, ^{64}Zn, ^{65}Cu, ^{66}Zn, ^{194}Pt, ^{195}Pt, ^{197}Au. Prior to measurements, a thin gold layer (few nm) was sputtered on the samples, which is used as a pseudo-internal standard. The whole sample tissue was scanned in a rectangular pattern. The laser power was set accordingly to ablate the complete tissue material in order to quantify the elemental concentrations accurately. The concentrations of trace elements were defined from the gold-normalized signal intensities that were calibrated using an external standard (dried droplet) as reported earlier.[117] Further details of the LA-ICP-MS measurements are given in publications II and III.

2.5. Data processing

FTIR spectra

The FTIR microscopic spectra of *E. Coli* bacteria were normalized to the symmetric phosphate band area (1080 cm^{-1}) in order to account for possible differences in thickness of the samples, assuming that in every bacterium the same amount of nucleic acids is present. The spectra of individual cells and tumor thin sections were normalized to the amide II band (1530 cm^{-1}) to account for possible differences in sample thickness, assuming that in every cell there is the same amount of proteins. If necessary, FTIR spectra were baseline corrected (linear baseline). For each sample at least five FTIR spectra were recorded. The acquired spectra were averaged and the standard deviation was calculated. Calculations were performed in Matlab (2013b) using custom-written code.

PTIR spectra

For every measurement a consequent five spectra were taken and averaged. Analogously For every PTIR measurement, a sequence of five spectra were taken and averaged. Analogously, five spectra were acquired at a substrate region where no absorbing sample is present i.e. clean gold surface as a reference. Since gold does not have absorption in mid-IR region, the PTIR spectrum of gold is expected to be similar to the incident laser power spectrum. Then, as was outlined before, according to equation 1.27, in order to obtain the PTIR spectrum, the recorded PTIR signal at the sample position is normalized (divided) to the background signal. The normalization scheme is depicted in figure 2.3.
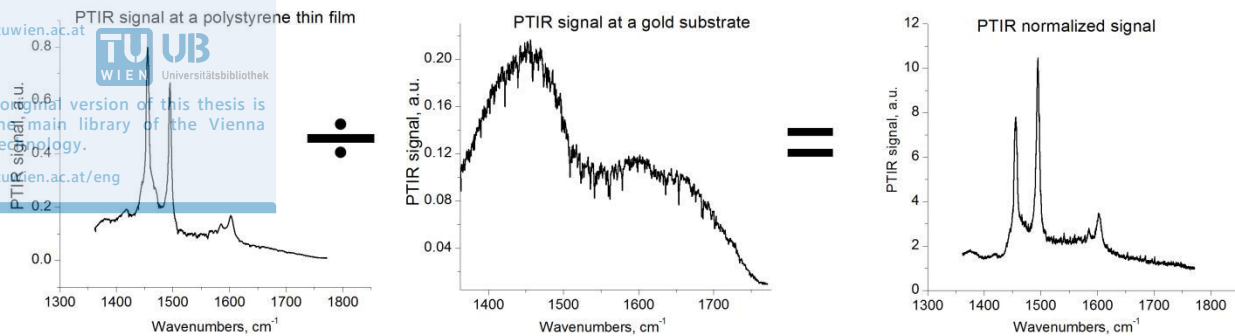
Figure 2.3. PTIR spectra background correction (normalization) workflow.

The standard deviation was calculated from the acquired spectra. Calculations were performed in Matlab (2013b) using a custom-written code.

The normalized PTIR spectra and their standard deviations were imported in the OriginPro software and processed. In particular, PTIR spectra were smoothed using Savitzky-Golay filtering (polynomial degree 2, 150 points window) or with FFT (150 points). For the spectral analysis of the amide I band, PTIR and FTIR spectra were normalized to the maximum.

For evaluation of the changes in spectral band intensities (mid-term stability of the AFM tips; bacteria IBs), bands of interest were integrated in Matlab (2013b) using custom-written code.

The percentage of proteins (IBs) in bacteria was determined as follows. In the FTIR spectra, the ratios between the integrated amide I band for IBs bacteria and control bacteria were calculated. In the PTIR spectra, the related ratio was obtained from the normalized absorption PTIR signal at 1657 cm^{-1} and the corresponding topography value.

AFM topographic and PTIR chemical maps were further processed in the Gwyddion software package. Typical slopes of topographical images were corrected using the "three point level" tool. Small spikes (pixel-sized) in PTIR images were masked manually using the "interpolation of small defects" tool.

The final graphical design of the figures was performed in the GIMP software.

Chapter 3

III.   Results and discussion

In this chapter we demonstrate and discuss the major results achieved in the scope of this doctoral project.

3.1. Time resolved PTIR spectroscopy

Introduction to the publication I
Method for time-resolved monitoring of a solid state biological film using photothermal infrared nanoscopy on the example of poly-L-lysine

Georg Ramer, Anna Balbekova, Andreas Schwaighofer, Bernhard Lendl.
Analytical Chemistry, 2015, 87(8): 4415-4420. DOI: 10.1021/acs.analchem.5b00241

In this paper we demonstrate the feasibility of the PTIR technique for time-resolved measurements across a range of more than 100 wavenumbers. We demonstrate that by detecting conformational changes in polypeptide (PLL) thin film. In particular, we follow the amide I band maximum that shifts depending on the secondary structure (e.g. α-helix, β-sheet) of the polypeptide. We induce those structural transformations by changing the degree of hydration of the polymer film.

Samples were prepared by spin-coating. A drop of an aqueous solution of PLL was casted on a spinning CaF_2 substrate. The chosen substrate allowed, firstly, to change the temperature of the sample (due to its high thermal conductivity), and secondly, to record the reference far-field (FTIR) spectra from the very same sample in transmission mode using a FTIR microscope. The transfer from β-sheet to α-helix was triggered by changing the degree of the sample hydration. The degree of hydration was adjusted by slowly changing the temperature of the sample.

During the measurements the sample was constantly purged with a stream of dry air enriched with D_2O vapor. We used D_2O vapor instead of H_2O since the absorption of the DOD deformation band (1280 cm^{-1}) does not interfere with the spectrum of the Amide I band in contrast to the H_2O molecule (1640 cm^{-1}).

The setup was constructed as described previously (see Chapter 2).

The cantilever was placed at the sample and then the QCL was tuned across its wavelength range while the temperature was changed. Before acquisition of a spectrum the lock-in amplifier has to be re-tuned to the current resonance frequency because the temperature changes caused alterations in the mechanical properties of the sample leading to a shift of the contact resonance frequency. For that prior to each measurement a resonance curve was recorded, the value of the resonance frequency corresponding to the maximum of this curve was set to the laser repetition rate.

The acquired PTIR spectra are in good agreement with the related FTIR spectra. The acquisition speed is 15 s per spectrum. Most of the time (13.5 s) is required for retuning the lock-in amplifier. By improving the tuning procedure it would be possible to achieve faster scanning rates.

3.2. PTIR system characterization

PTIR system performance

We follow the performance of the custom made PTIR system while measuring a polystyrene (PS) thin film. We use FTIR spectroscopy as a reference technique for evaluation of the performance of the PTIR system. The sample was formed by spin coating on gold and CaF_2 substrates (see Chapter 2). PTIR spectra were acquired with a new AFM tip. Figure 3.2.1 display spectra of the PS film.
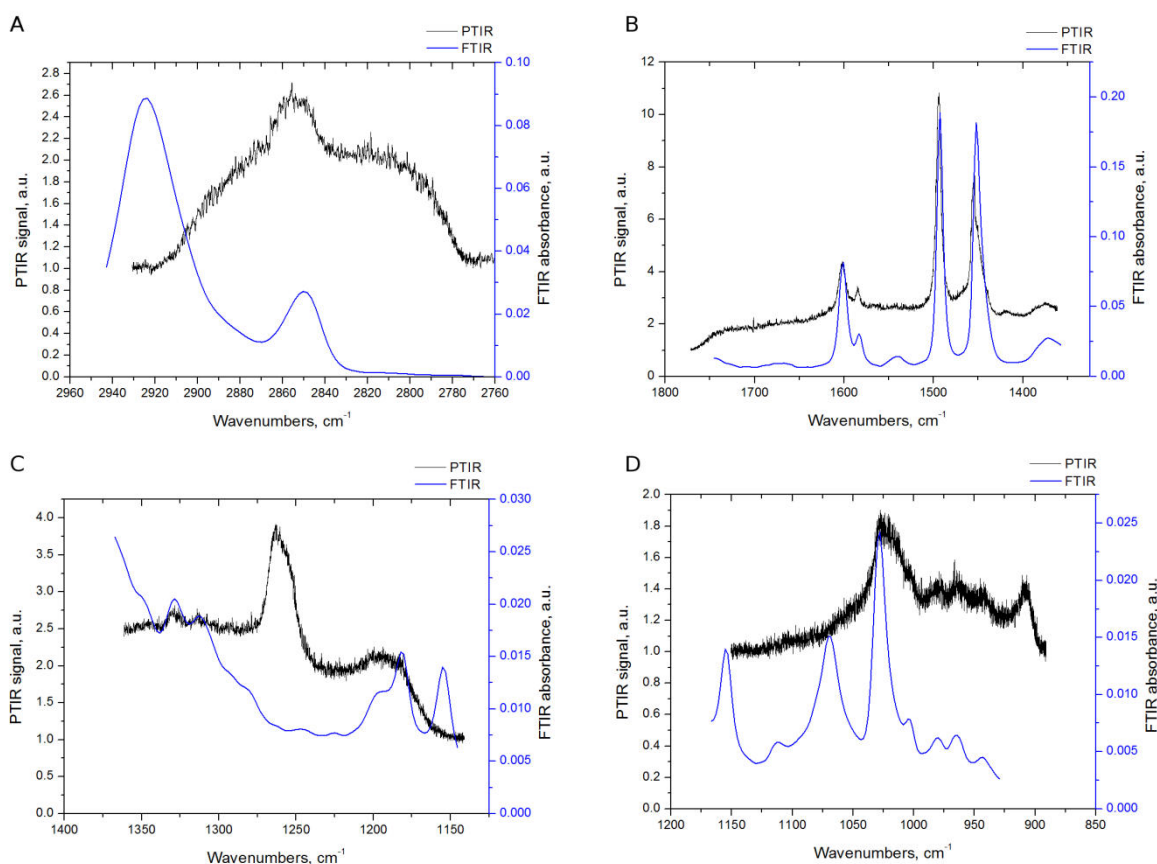

Figure 3.2.1. PTIR and FTIR spectra of 60 nm PS film recorded at different spectral regions by different QCL chips in Mircat laser: QCL 1 (A), QCL 2 (B), QCL 3(C) and QCL 4 (D).

We divide the recorded PTIR spectra from PS to the PTIR signal acquired at a clean gold surface (see Chapter 2). Such normalization to the laser power allows us to correct PTIR spectra for the laser power. Since the laser source consists of four lasers, an acquired PTIR spectrum consists also of four spectra that cover a wide spectral range. Each laser has a different laser power spectrum and emits laser pulses with different intensity. Due to the

difference in the laser power the signal to noise ratio in the related PTIR spectra is different. In particular, a PTIR spectrum is recorded using the QCL with a lower intensity would be noisier then the one recorded with a higher laser power (compare Figure 2.2 and 3.2.1). The best signal to noise ratio is observed for QCL 2 and 3 (Figures 3.2.1 B and 3.2.1 C).

From the one side, PTIR spectra of PS demonstrate a good agreement with the related FTIR spectra when the laser intensity is decent (Figure 3.2.1). From the other side, we observe a mismatch with FTIR spectra in the spectral regions with the lowest laser power, i.e. 2940-2880 cm^{-1} (Figure 3.2.1 A, QCL 1) and 1200-1045 cm^{-1} (Figure 3.2.1 D, QCL 4). In the spectral region of the QCL2 (Figure 3.2.1 B) we observe a strong band with a maximum around 1260 cm^{-1}. In this spectral region PS does not have absorption bands. We relate this band to the symmetrical deformation δ_s(Si-CH$_3$) in Polydimethylsiloxane (PDMS). Contamination of commercial AFM tips with PDMS was reported previously[118] and explained by the usage of this polymer in packaging materials used for shipping AFM probes. Another reason for this band could be the presence of a thin layer of silicon oxide between the tip material and the gold coating. If the thickness of the gold layer (in our experiment around 70 nm) is not large enough, then the enhanced EM field around the tip will penetrate through the gold material and will be absorbed by the tip material. Typically the distance over that the EM field totally decays in a metal is about three skin depths[119] (around 90 nm). If the EM is not shielded by the metal and absorption occurs, then the AFM tip material itself can be detected by PTIR. However, the related phonon absorption[120] band of Silicon oxide is expected to appear much broader[121] than is observed in our experiments. Based on these considerations we conclude that the band is related to PDMS. In the further investigations we call this band as "silicon band" since it is attributed to silicon.

AFM tip stability

The PTIR technique is capable of qualitative and quantitative material characterization[122]. For that the PTIR system needs to deliver reliable and reproducible results. The stability of the system depends mainly on the stability of its key elements: mid-IR laser (power stability and pointing stability), AFM and an AFM probe (tip). Additionally, the performance of the system strongly depends on the method of the PTIR signal detection (see chapter 1.3).

Besides that, the stability of measurements is influenced by the external factors such as mechanical vibrations and atmospheric factors (e.g. water vapor).

The performance of the mid-IR laser, used in this work, was characterized previously.[35] We used a resonance tracking method that allows automatic adjustment to changes in the contact resonance. This facilitated an improved performance of the system[35]. However, so far the aging of AFM probes during the measurements was not considered. In this project we investigate for the first time the influence of the AFM probe stability on the performance of the PTIR system.

A degraded (aged or contaminated) AFM tip might significantly reduce the sensitivity of the PTIR measurements. Since the reduced or vanished PTIR signal leads to false quantitative analysis or poor quality chemical images. It is important to define when the probe starts degrading. When it comes to an investigation of an unknown sample it is difficult to

distinguish whether the PTIR signal is small due to the low absorption in the sample (low concentration of an analyte) or due to the degraded tip.

We investigated the tip performance while measuring a standard polymer sample with known properties. In addition we studied AFM tip degradation while measuring biological samples. We support our findings by characterizing "new" and "used" tips with SEM and EDX spectroscopy.

Stability of AFM probe during prolonged PTIR measurements

We investigate the AFM tip performance while measuring the standard polymer sample with known properties. The standard is a flat homogeneous polystyrene (PS) thin film (60 nm) prepared on a gold substrate via spin coating. While keeping the parameters of the PTIR measurement (e.g. gain, setpoint, amplification, etc.) constant, we follow the integrated band intensities over time (number of measurements). From these measurements we conclude on the tip stability. We follow the most prominent bands in IR spectrum of PS related to: $v(C=C)$ vibration (with maximum around 1600 cm^{-1}) and $\delta(CH)$ vibration (with maximum around 1452 cm^{-1}). A "working" (not degraded) AFM tip is expected to provide bands with constant intensities.

We evaluate the degradation of the AFM tip during eight hours of non-stop (prolonged) measurements while acquiring PTIR spectra of the PS film always at the same point. During the prolonged measurement about 50 spectra and three chemical images (5 μm^2, 218 points per line) were recorded every hour. We observe no significant differences in all band intensities. The plotted values of integrated band areas (baseline subtracted) vs the number of acquired measurements are given at the Figure 3.1.2.
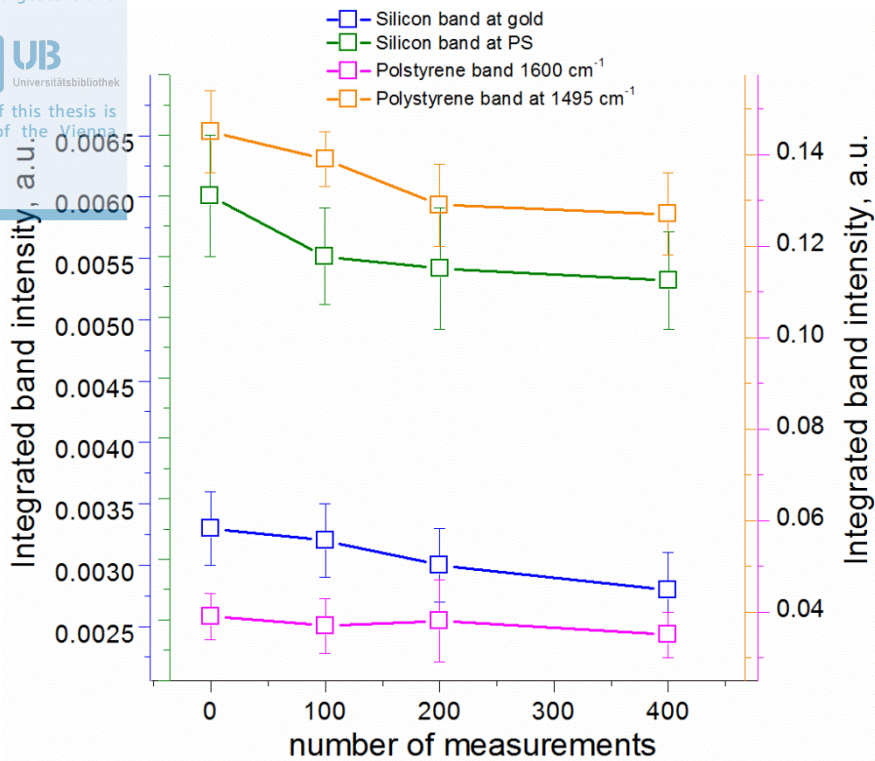
Figure 3.2.2. Integrated band intensities PTIR spectra of a PS thin film recorded with the same AFM probe at different number of measurements. Error bars – two standard deviations.

The PTIR band intensities of PS and the silicon band intensity (at the PS sample and at a clean gold substrate) acquired after the prolonged measurements possess alike intensities (Figure 3.2.2). Thus, we suppose that after the prolonged measurement of a polymer film using a single AFM tip a stable PTIR signal can be expected.

Performance of AFM tips after measuring biological samples

We evaluate the performance of AFM tips that were used for PTIR measurements of a biological sample. We acquire PTIR spectra of the PS thin film after several PTIR measurements of a single *E. Coli* (about 100 spectra and 10 chemical images). Figure 3.2.3 shows the plotted PTIR spectra that were acquired using the same AFM tip after the prolonged measurements of the PS film after several measurements of the bacteria.
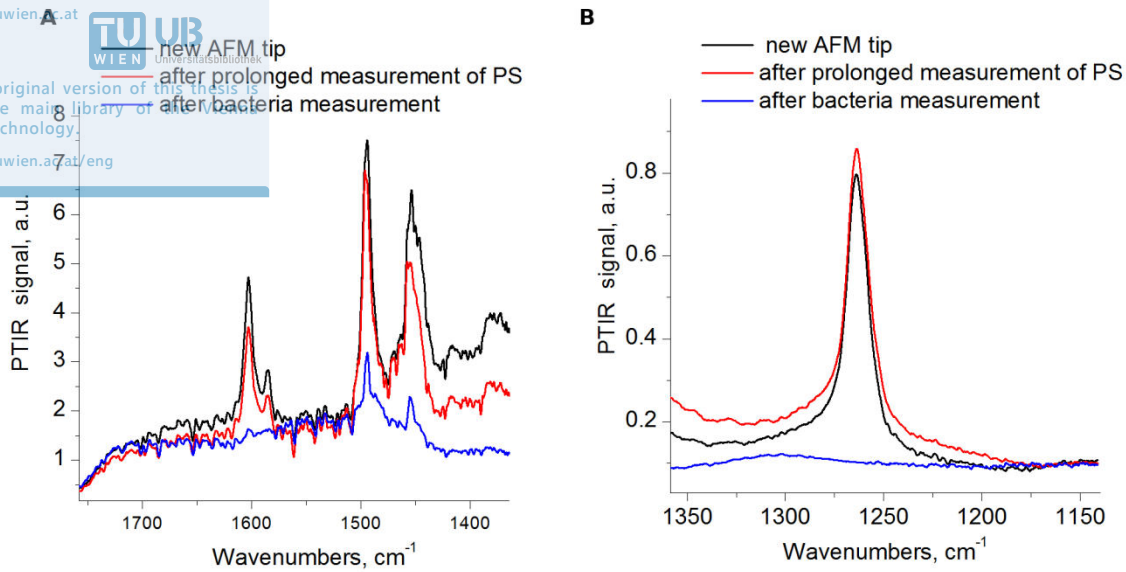
Figure 3.2.3. PTIR spectra of a PS thin film using a new AFM tip, a tip after the prolonged measurements of PS, a tip after several measurements of biological sample; of different spectral regions: a spectral region with the PS related bands (A) and a spectral region with the Silicon band (B).

The PTIR spectra were normalized to the PTIR spectrum recorded on a clean gold substrate. The band intensities of the PS standard acquired after measurements of a single bacterium are notably decreased compared with those acquired after the prolonged measurements of the PS film. The band with maximum around 1600 cm^{-1} almost disappeared and other bands are notably faded (Figure 3.2.3 A). The intensity of the silicon band decreased as well (Figure 3.2.3 B).

We explain the decrease in PTIR signal intensities by contamination of the tip during bacteria measurement. During AFM measurements of soft samples (such as biological samples) in contact mode a part of the sample could easily stick to the AFM tip. That could lead to a decrease of the lightning rod effect and a loss in the enhancement of the electromagnetic field. Decreased enhancement leads to a lower field intensity, therefore less absorption of the material is detected. The contamination of the AFM tip explains the decrease in the silicon band intensity in PTIR spectra recorded on the gold substrate after bacteria measurement as well (Figure 3.2.4).
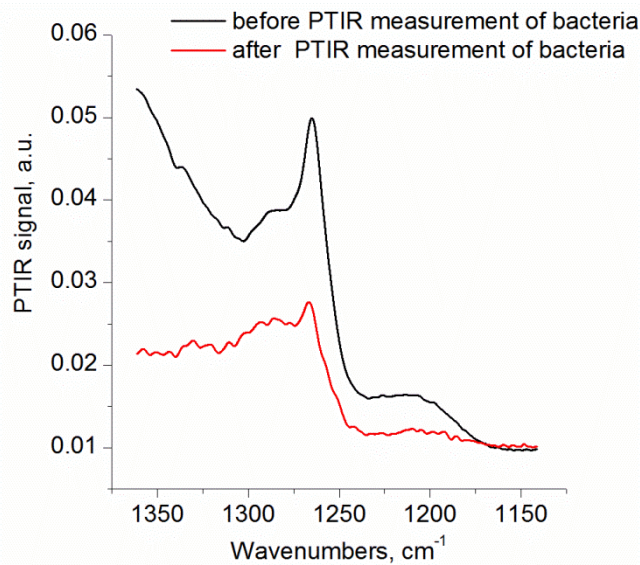
Figure 3.2.4. PTIR spectra of a clean gold substrate before and after measurements of an *E. Coli* bacterium.

The intensity of the silicon band recorded at the gold substrate is lower than the intensity of this band in PTIR spectra of a PS film. We explain this effect by the different thermal conductivity of the materials (metal and polymer). We observe the qualitative correlation between the AFM tip aging and changes in PTIR band intensities of PS and the silicon band. Thus, the intensity of those bands can be used in determination of the AFM tip aging. The performance of an AFM tip and its aging can be estimated by evaluating the band intensities of the standard sample (PS) or can be directly monitored on the gold surface (the area out of the sample).

Characterization of AFM tips with scanning electron microscopy and energy dispersive X-ray spectroscopy

In order to characterize morphological changes in AFM tips occurring after PTIR measurements new AFM probes as well as probes utilized in the measurements were investigated with scanning electron microscopy (SEM) and energy dispersive X-ray (EDX) spectroscopy. SEM images and EDX spectra were obtained using Quanta 200 (FEI, USA) scanning electron microscope coupled to Genesis (EDAX, USA) energy dispersive spectrometer. In figure 3.2.5 SEM images of a new AFM tip are given.
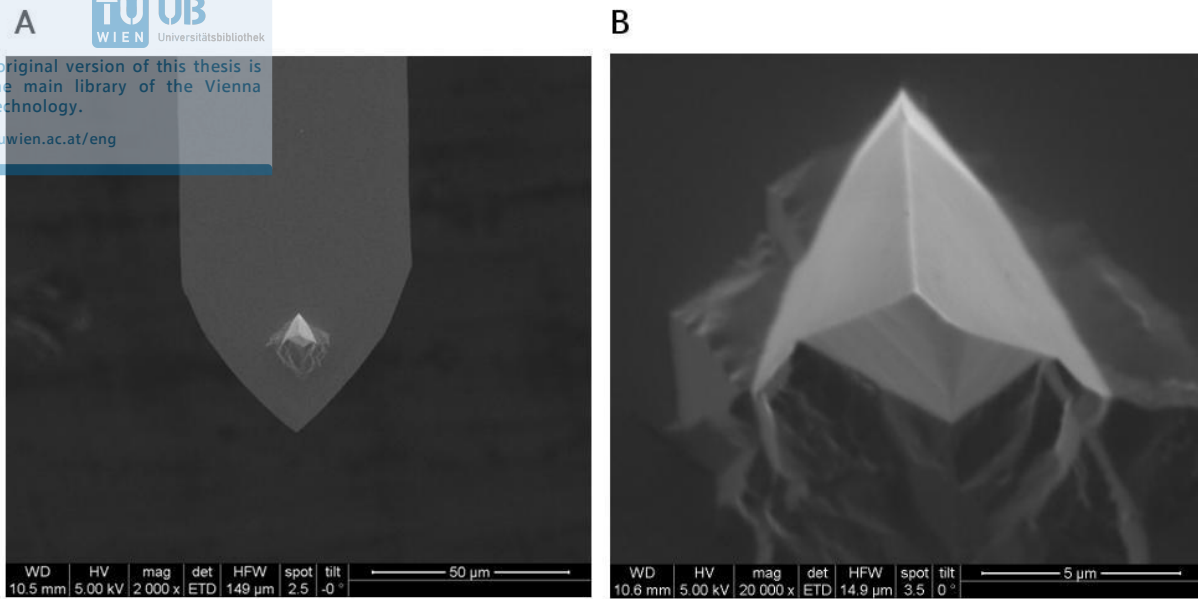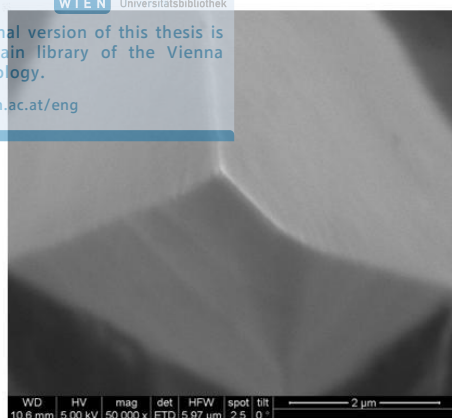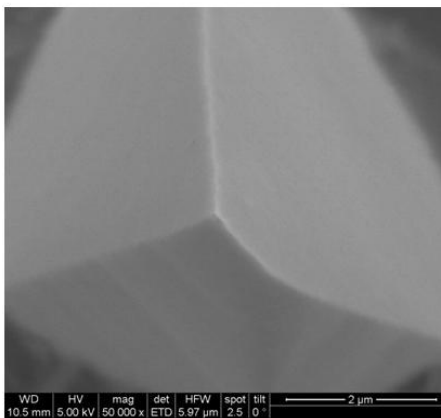
Figure 3.2.5. SEM image of the new AFM tip (A) and its magnified part (B) utilized in PTIR measurements.

The SEM image shows that the AFM tip has a pyramidal shape which is in line with the specifications (Figure 3.2.5). SEM images of a new tip were compared to the SEM images of the probes which had been used in PTIR measurements (Figures 3.2.6).
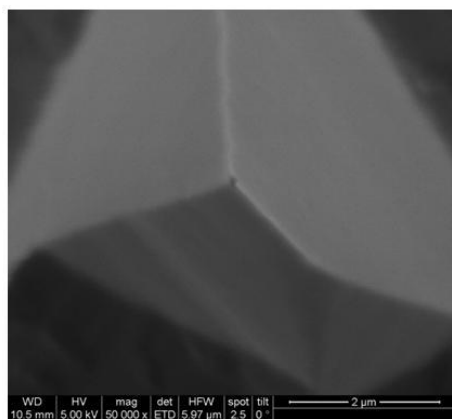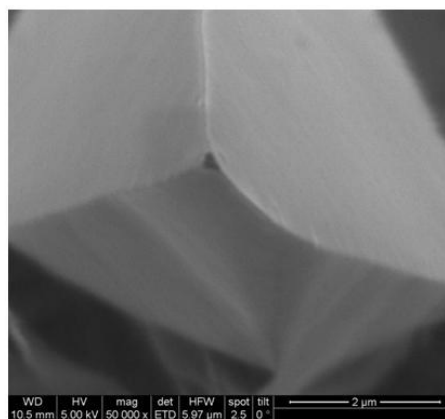
Figure 3.2.6. SEM images of a new AFM tip (A), after PS measurements (B), after mammalian cells measurement (C) and after bacteria measurement (D).

SEM images of the new AFM tip (Figure 3.2.6 A) and the tip used in PTIR measurements of the PS thin film (Figure 3.2.6 B) do not differ visually. It is in line with the PTIR results, where no distinguishable degradation of the signal was observed during prolonged measurements of PS. Unlike the "PS probe", on the top of the probes utilized in PTIR measurements of biological samples small contaminations can be observed (a larger contamination is observed after measurements of mammalian cells). This contamination might occur after contact of an AFM probe with a soft sample. A contaminated tip might be a reason for the decreased sensitivity of the system, as was previously demonstrated by PTIR spectroscopic measurements.

EDX spectra taken at the top of the AFM tips (new and contaminated after measurement of a bacterium) are given at the Figures 3.2.7-8.
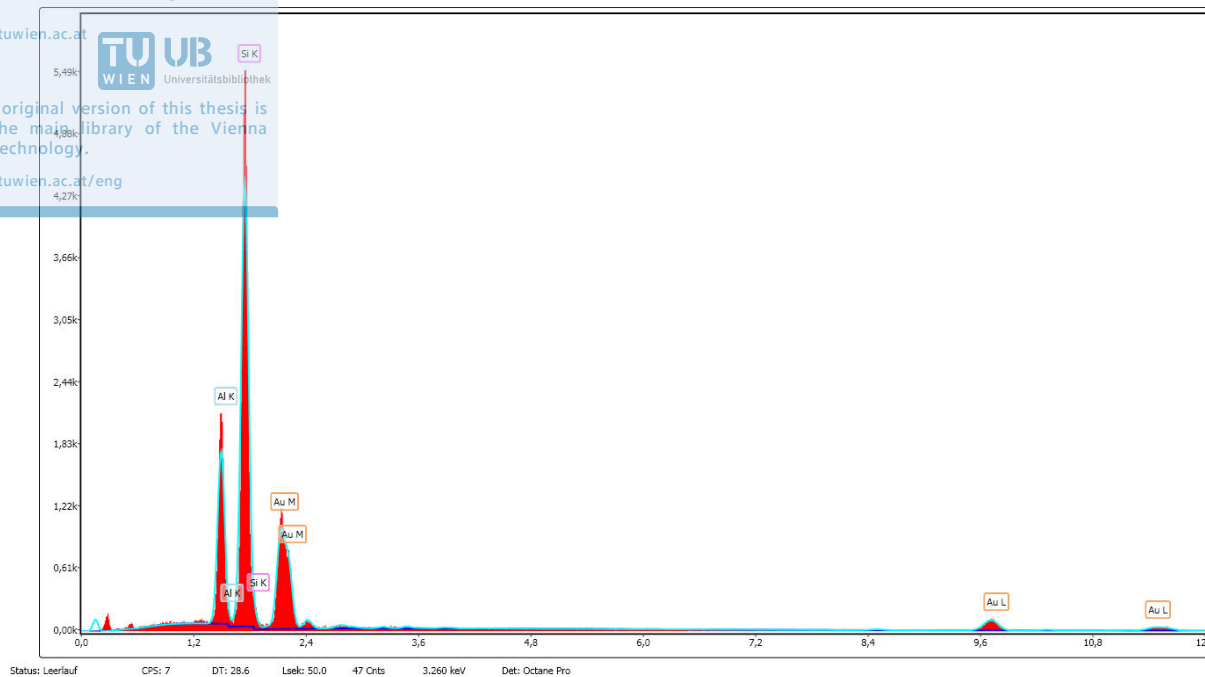
Figure 3.2.7. EDX spectra of a new tip.
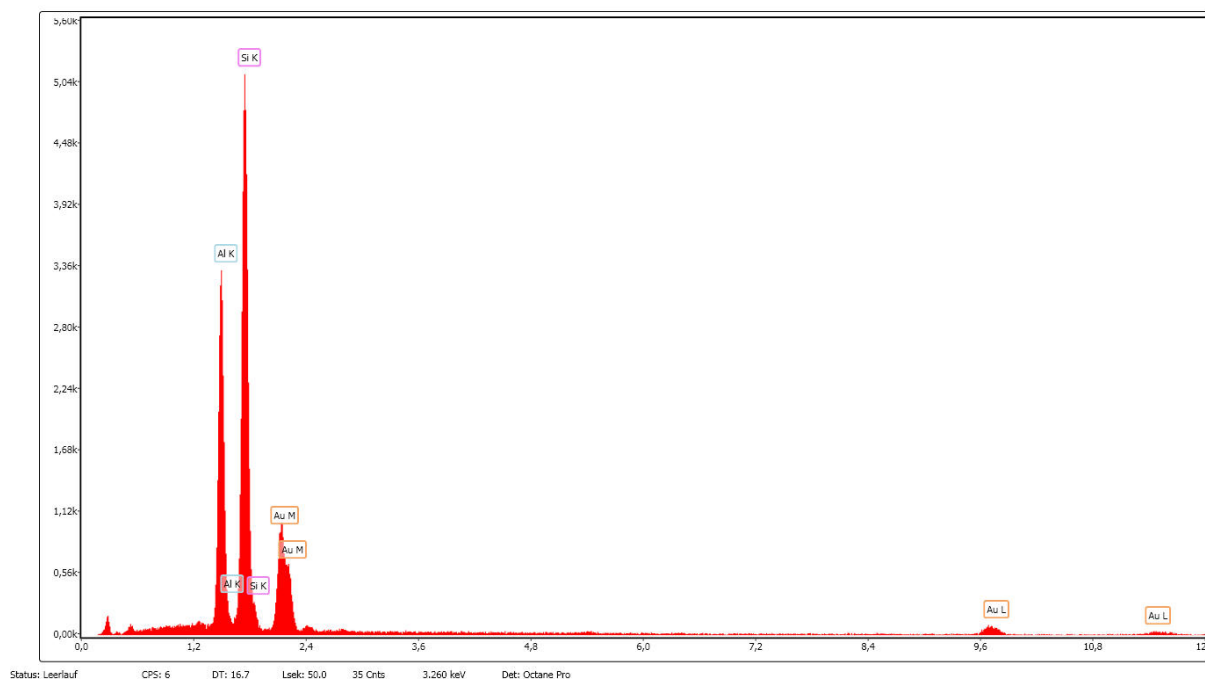
Figure 3.2.8. EDX spectra of a tip used in PTIR measurements of bacteria.

In the EDX spectra of the both "new" and "used" AFM tips several elements are primarily present. They are Si (associated with the material from which probe is made), Au (associated with the metal coating material) and Al (might be an additive used also for metal coating). The presence of the metals at the tip of the used tip suggests that the overall gold coating was not disturbed during measurements.

71

3.3. PTIR spectroscopy and chemical imaging of biomedical samples

In this sub-chapter we provide the results of the PTIR analysis of different biomedical samples, such as single bacteria *E. coli* with inclusion bodies; apoptotic and viable tumors and individual apoptotic (dead) and control (viable) mammalian cells. While performing the PTIR measurements of the biological samples, we employed a method of monitoring AFM tip performance (see chapter 3.2). An AFM tip was replaced always when the silicon band in the PTIR spectra had disappeared. The quality control spectra that represent the PTIR spectra acquired on a clean gold substrate before and after each chemical mapping are given in the Appendix.

Bacteria Inclusion Bodies (IBs)

It was shown by numerous studies that FTIR spectroscopy is capable of characterization of bacteria with IBs (protein clusters accumulated in recombinant bacteria)[77]. Most of the studies were performed on the bulk material; therefore only average spectra from an assembly of bacteria were obtained. Using synchrotron-based microscopic techniques single bacterium can be imaged[123], but due to the optical diffraction limit it is still a challenge to image a bacterium at the intracellular level. Here we attempt to access the spatial distribution of IBs and their properties using the PTIR technique. The spectral properties of the bulk bacteria with IB and control bacteria were initially defined by FTIR spectroscopy (Figure 3.3.1).

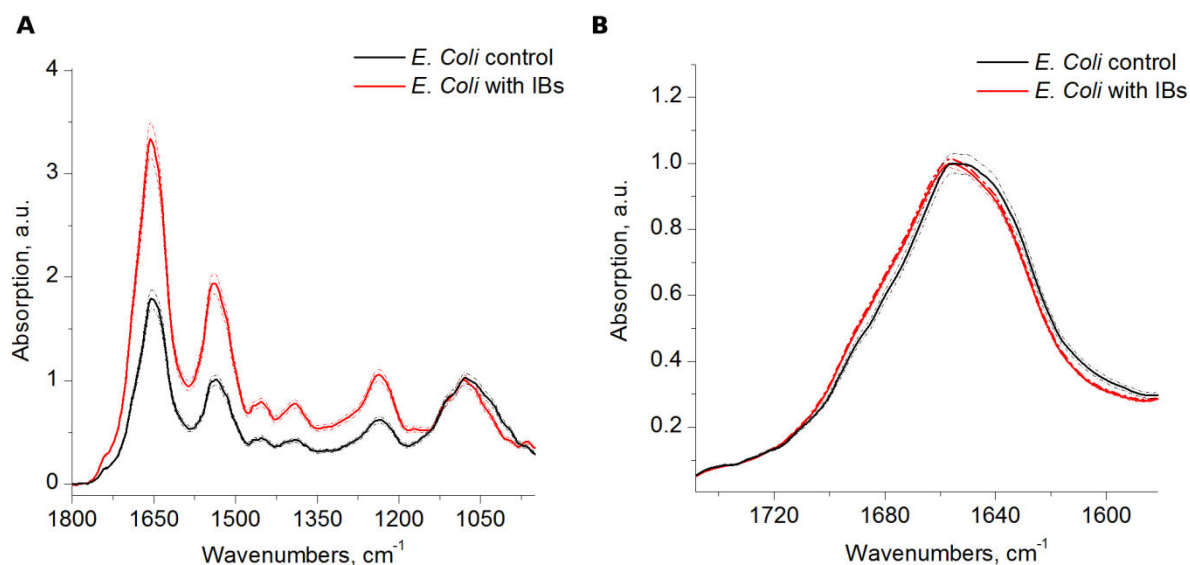**Figure 3.3.1.** FTIR spectroscopy of bulk bacteria *E. Coli* with IBs and a control sample. Spectra normalized to the symmetric phosphate band (A) and the normalized amide I band (B). Dashed lines depict two standard deviations.

The intensity of the amide bands in spectra of bacteria with IBs is almost two times larger than for the control bacteria (Figure 3.3.1 A). To account the possible differences in the

number of bacteria in a bulk sample, commonly spectral normalization is done using the amide I or amide II bands as references[124]. In this work, due to the pre-known fact that the amount of proteins in bacterial cells is different, we normalize the spectra to the intensity of the symmetric phosphate stretching band, assuming the same amount of nucleic acids in both kinds of bacteria. The difference in intensity of the amide bands in IBs containing bacteria and in control bacteria confirms the presence of protein IB in bacteria with IBs. The different shape of the amide I band (Figure 3.3.1 B) suggests a different conformation of proteins in bacteria with IB and control bacteria.

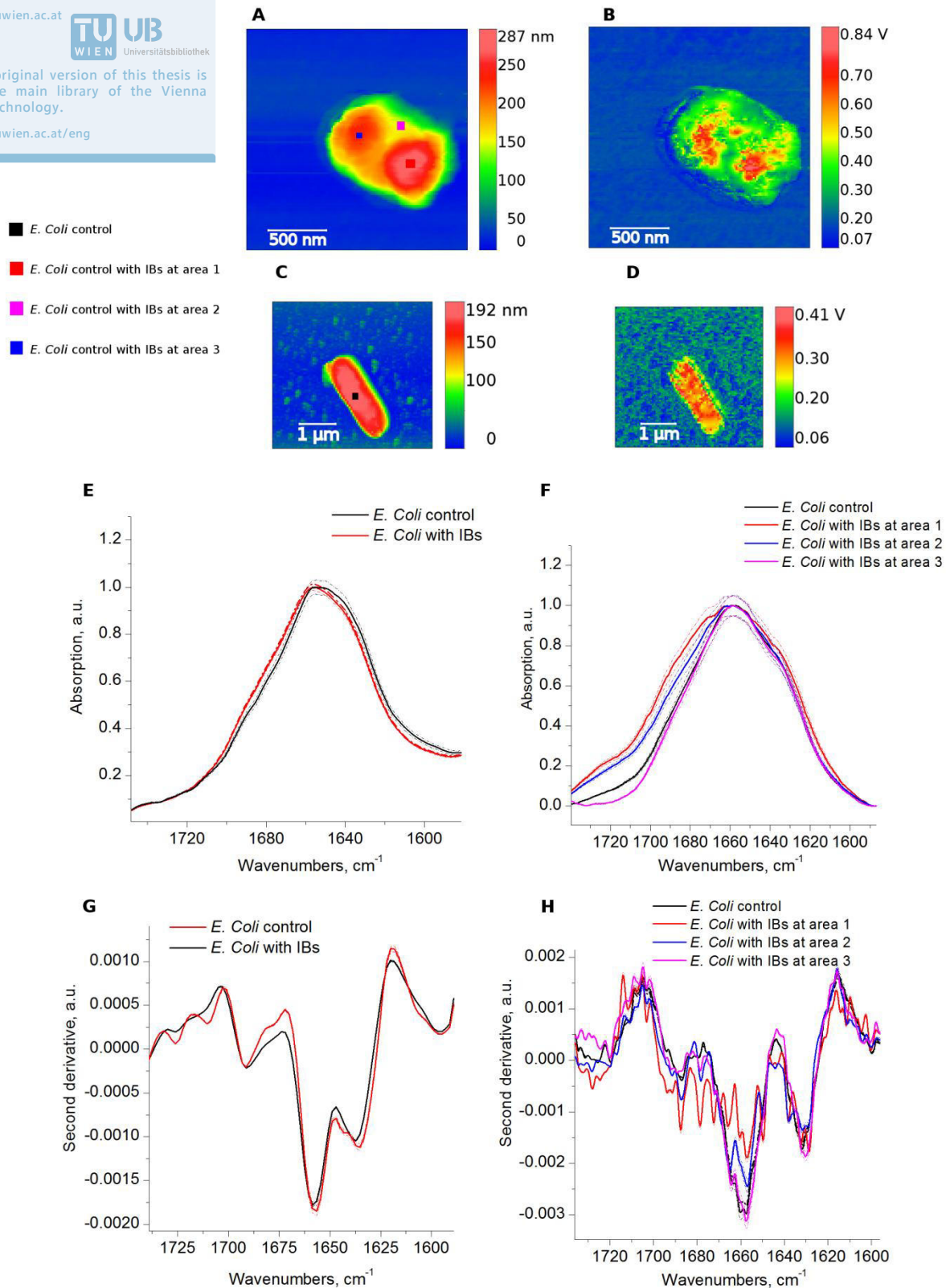Further, we performed PTIR analysis of individual bacteria (Figure 3.3.2).

Figure 3.3.2. AFM topographic images (A, C); PTIR chemical maps of proteins (1657 cm^{-1}) (B, D); FTIR (E) and PTIR (F) spectra; FTIR (G) and PTIR (H) second derivative spectra of *E. Coli* with IBs and *E. Coli* control respectively. Dashed lines depict two standard deviations.

The topographies of *E. Coli* with IBs and control are different (Figures 3.3.2 A and C). The topography of the bacterium with IBs is not flat (Figure 3.3.2 A) a fact that might be explained by the presence of IBs. The topography of the control bacterium is more even (Figure 3.3.2 C). Chemical maps of proteins (1657 cm^{-1}) agree with the related topographies. The regions with elevated protein signal are found in IBs bacteria (Figure 3.3.2 B), whereas the chemical maps of control bacteria are rather homogeneous (Figure 3.3.2 D). Analogous results were reported recently[3].

According to FTIR analysis, bacteria with IBs have about two times (50%) more proteins than the control bacteria. This value we obtained from the ratio between the integrated amide II bands in the spectra of control and IBs bacteria which were normalized to the symmetric phosphate band. According to the PTIR analysis bacteria with IBs have about one third (27%) more proteins than the control bacteria. To access the relative amount of proteins in IBs we normalized the maximum PTIR signal of proteins to the related topographic value (the height). The maximum normalized signal (0.0029 V/nm) is nearly 27% larger than the signal obtained from the control cells (0.0021 V/nm). The difference between the FTIR and PTIR results can be explained by the fact that the FTIR spectra were taken from the bulk material, thus, giving an average amount of proteins, whereas the amount of proteins in every individual bacterium with IBs might be different. Thus, in the investigated *E.Coli* with IBs we found less IBs than in the average bacteria.

We compared the shape of amide I band in the PTIR spectra of the bacteria at the regions of IB and outside them with the spectra of the control sample (Figure 3.3.2F). Similarly to the FTIR results (Figure 3.3.2 E), we observe a band broadening at 1640 cm^{-1} meaning that the relative amount of beta sheets in IBs bacteria is larger compared to the control samples. The PTIR spectra measured at different IBs are similar to each other but differ from the spectra collected at the region outside of IBs. The PTIR spectra of the control bacterium are similar to those acquired from IBs bacterium outside of the IBs regions. Second derivative spectra of amide I band in FTIR spectra (Figure 3.3.2 G) showed an increased peak in the region of 1635 cm^{-1} related to parallel β-sheets for *E. Coli* with IBs. Second derivative spectra of the amide I band in the FTIR spectra (Figure 3.3.2 H) showed periodic peaks related to the water vapor absorption. Those peaks in the spectra make it difficult to evaluate changes in protein secondary structure.

Further, we analyzed PTIR spectra of *E. Coli* in the spectral region related to nucleic acids (Figure 3.3.3).
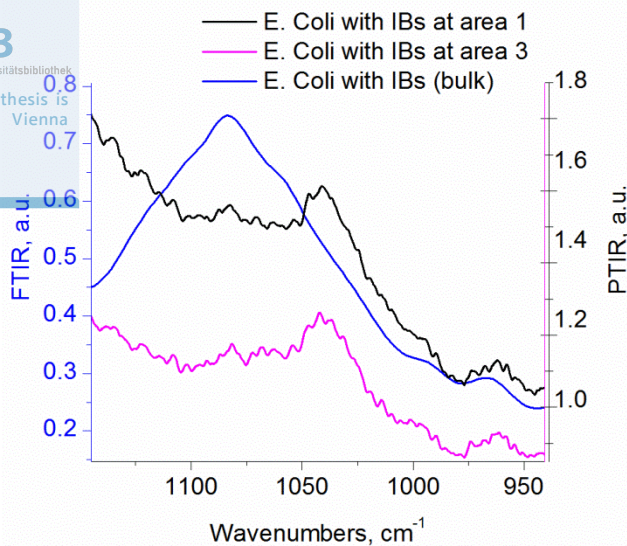
Figure 3.3.3. PTIR spectroscopy of bacteria *E. coli* in the nucleic acids spectral region.

Figure 3.3.3 demonstrates PTIR spectra of *E. coli* normalized to the gold background (see chapter 2). The PTIR spectra appeared as two weak bands. The first band we relate to the phosphate symmetric stretch (can be distinctly seen in the FTIR spectra). Although this band is broad and centered around 1080 cm^{-1} in the FTIR spectra, it appeared narrow and shifted with a maximum around 1040 cm^{-1} in PTIR spectra. We suppose that the band appeared partially in PTIR spectra due to the low laser power in the spectral region 1200-1040 cm^{-1}. Additionally, the weak PTIR signal might be due to the low concentration of the nucleic acids (nucleic acids are not localized but spread across a bacterium). In the spectral region where the laser power profile has its maximum (around 960 cm^{-1}) we observe another weak band related to the C-N-C stretch of ribose-phosphate skeletal vibrations in nucleic acids[50].

Tumor tissue

In this sub-chapter we investigate a tumor (C26 mouse colon adenocarcinoma) thin section with apoptotic and viable tissue regions. During the extensive study of this sample with FTIR spectroscopy (see chapter 3.4.) we defined IR spectroscopic properties of this sample. The aim of this project was to find whether the sample properties revealed by FTIR spectroscopy agree with the results of PTIR spectroscopic analysis (Figure 3.3.4).
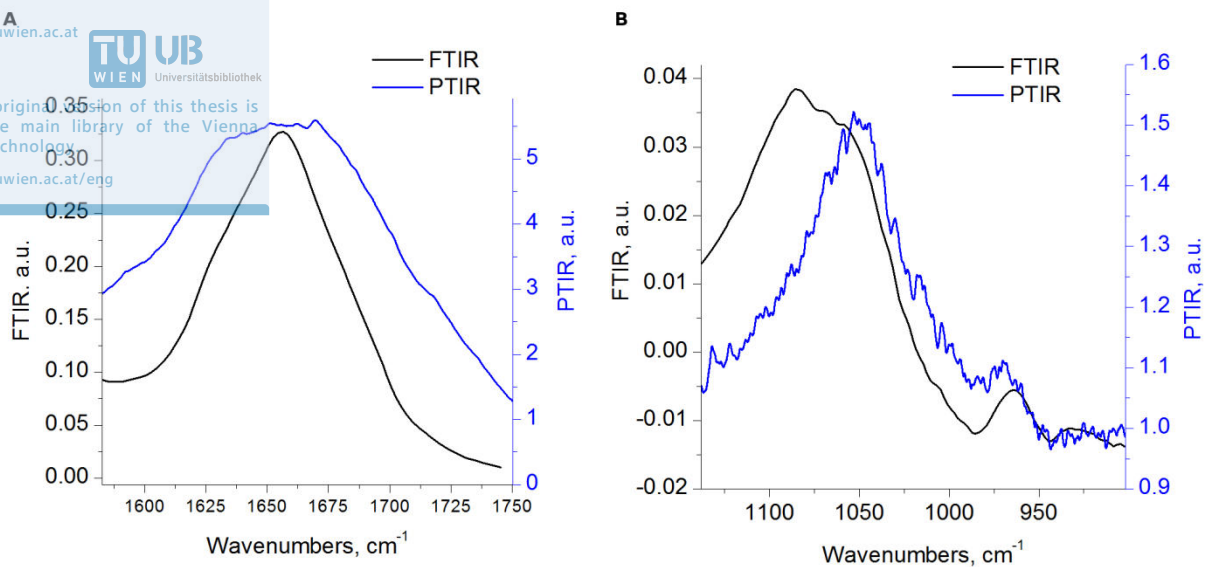
Figure 3.3.4. PTIR and FTIR spectra of a position from the tumor histological sample at different spectral regions: protein related (A), nucleic acids related (B).

Acquired at the tumor sample PTIR spectra we normalized to the PTIR background spectrum. The background spectrum at a clean silicon substrate was acquired. The PTIR spectrum of the sample in the amide I band region (Figure 3.3.4 A) appears broader compared to the related FTIR spectrum. Analogously to the PTIR spectra of *E. Coli* (mentioned above in this chapter), the band related to the nucleic acids (symmetrical phosphate stretch) can be partially seen in the PTIR spectra (Figure 3.3.4 B). Nearly half of the band (1200-1050 cm^{-1}) is absent due to the low laser power in this spectral region. Another band related to the C-N-C stretch of ribose-phosphate skeletal vibrations in nucleic acids (centered around 960 cm^{-1}) can be resolved in the PTIR spectra.

Further, we acquired PTIR spectra at apoptotic and viable regions and compared them with FTIR spectra (Figure 3.3.5).
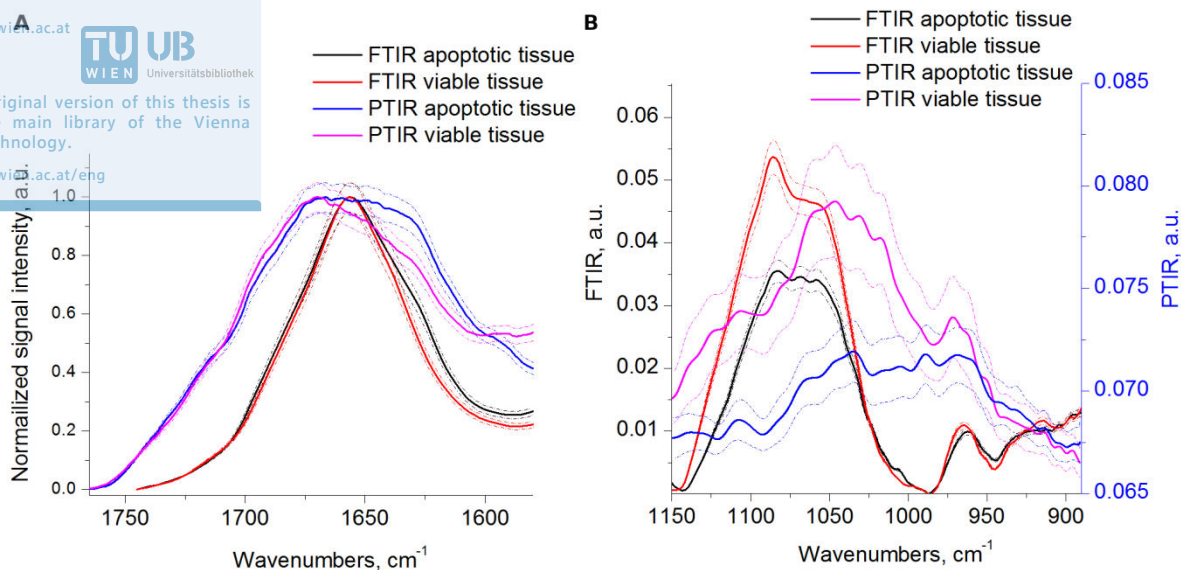
Figure 3.3.5. PTIR and FTIR spectra of the apoptotic and viable histological samples at different spectral regions: protein related (A), nucleic acids related (B). Dashed lines depict two standard deviations.

The amide I band in PTIR spectra (Figure 3.3.5 A) of apoptotic tissue region appeared to be broader in the spectral region of 1640 cm^{-1} compared to the spectrum related to viable tissue. Such change in protein secondary structure is a common marker for cell death.[41] Similarly to the PTIR spectral analysis, broadening of the amide I band in the range of parallel β-sheets has been observed for apoptotic tissue in FTIR spectra (Figure 3.3.5 A). The intensity of the phosphate band in the PTIR spectrum of the viable tissue region is larger than of the apoptotic region (Figure 3.3.5 B). Those results agree with the results of FTIR spectral analysis. The phenomena of the decay in the nucleic acids related bands in IR spectrum is explained by nuclei condensation[41,42].

Individual apoptotic cells

In this sub-chapter we study individual HAP1 EAP cells. The cell lines were cultivated on gold and CaF$_2$ substrates. Some cells were incubated with Puromycin, thus, apoptosis (programmed cell death) in those cells was induced. Other cells were not treated with the drug (control sample). For more details see chapter 2.

Figure 3.3.6 shows PTIR chemical imaging and spectroscopy of a control HAP1 EAP cell. We use FTIR spectra of bulk material (many cells) as a reference for PTIR spectra acquired from individual cells.
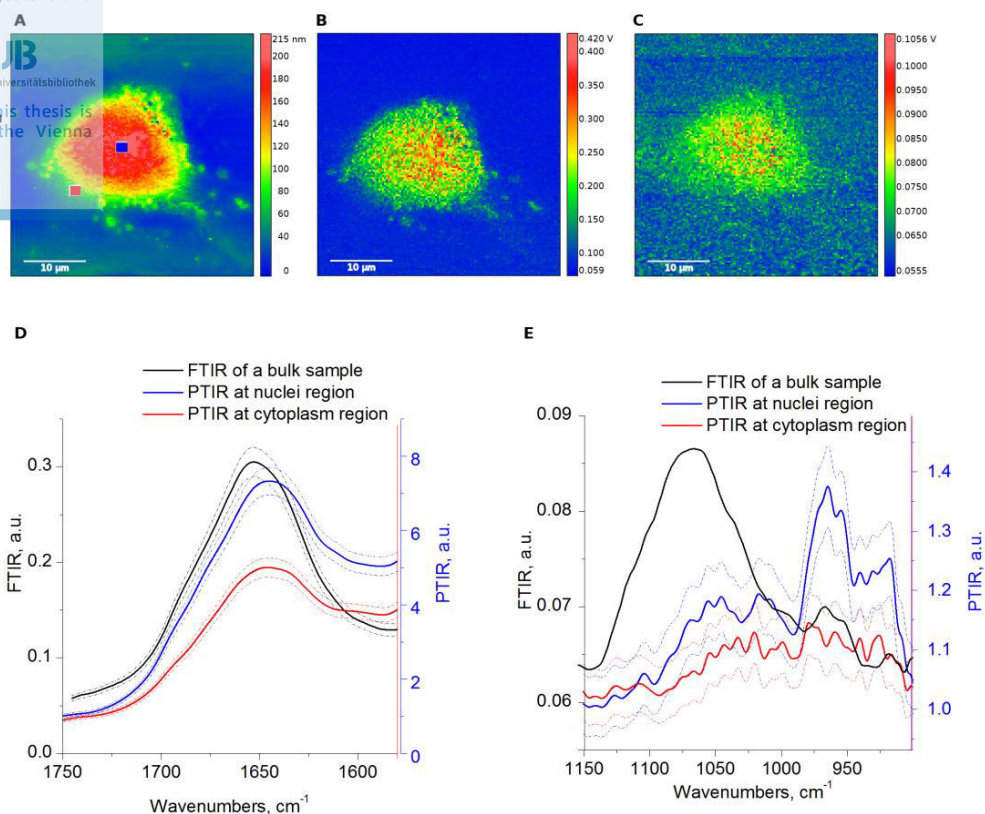
Figure 3.3.6. AFM topographic image of a control HAP1 EAP cell (A). PTIR map of the cell at frequency 1650 cm^{-1} (amide I signal intensity) (B). PTIR map of the same cell at 965 cm^{-1} (nucleic acids signal intensity) (C). PTIR spectra acquired at nuclei (blue) and cytoplasm (red) regions; FTIR spectra of a bulk HAP1 EAP control sample (black) in amide I (D) and nucleic acids (E) spectral regions. Dashed lines depict two standard deviations.

The PTIR image related to the maximum of the amide I band at 1650 cm^{-1} (Figure 3.3.6 B) indicates the strongest absorption in the nuclei region. This agrees well with the topography map (Figure 3.3.6 A). The chemical map related to a band centered at 965 cm^{-1} (Figure 3.3.6 C) correlates with the topographic image as well. This band is related to C-N-C stretch of ribose-phosphate skeletal vibrations in nucleic acids.[50] Those molecules are present in nucleic acids and therefore the signal obtained from this band is directly related to DNA. No distinct differences in spatial distribution of proteins (Figures 3.3.6 B) and nucleic acids (Figure 3.3.6 C) were observed.

The position of the amide I band in the PTIR spectrum (Figure 3.3.6 D) correlates well with the FTIR spectrum. No notable differences in the amide I band shape within nuclei and cytoplasm were observed.

The strong absorption of the band centered at 1080 cm^{-1} can be observed in the FTIR spectrum (Figure 3.3.6 E). This band is assigned to the phosphate symmetric stretch and related to nucleic acids. This band cannot be detected by the PTIR technique due to the low laser power in this region (1150-1050 cm^{-1}). However, another band centered at 965 cm^{-1}, which is also related to nucleic acids, was possible to detect. The position of this band agrees well with the corresponding FTIR spectrum.

Figure 3.3.7 shows FTIR spectroscopy of apoptotic (dead) and control (viable) HAP1 EAP cells (bulk material):
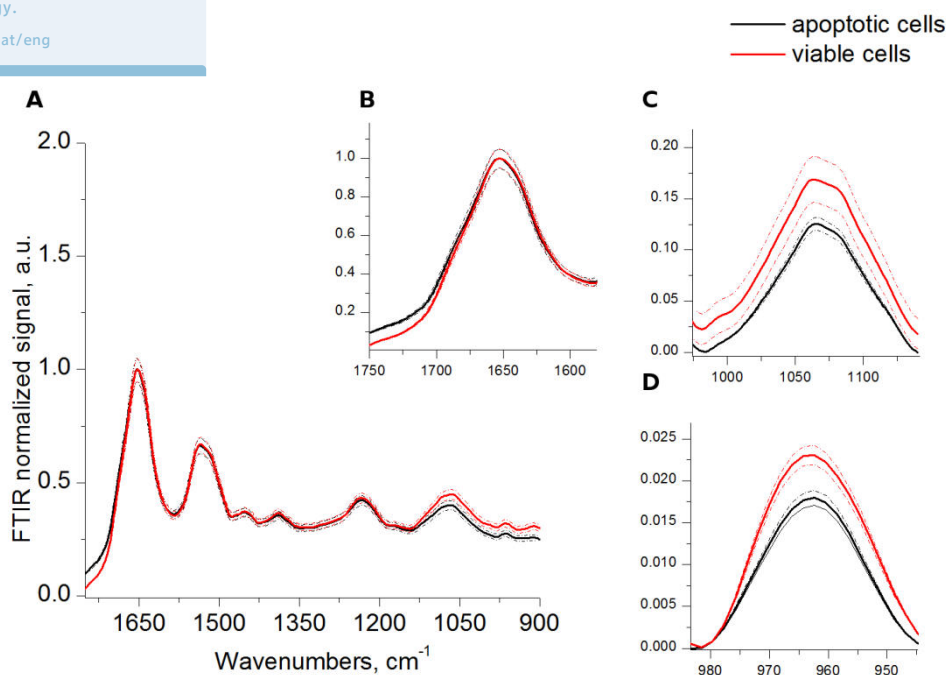
Figure 3.3.7. FTIR spectra of HAP1 EAP apoptotic and control cells (A). Inset: normalized amide I band (B); normalized phosphate band (C); normalized ribose-phosphate band (D). Dashed lines depict two standard deviations.

To account for possible differences FTIR spectra were normalized to the amide II band area. To analyze the change in band shape of the amide I band, it was normalized to its maximum. We observe almost no changes in the shape of the amide I band among apoptotic and viable cells (Figure 3.3.7 B). Further, we observe a decrease in the intensity of the phosphate (Figure 3.3.7 C) and ribose-phosphate (Figure 3.3.7 D) bands in apoptotic cells (comparing to control cells). Those spectral differences in apoptotic and viable cells were reported previously[42].

The following results demonstrate PTIR analysis of two types of HAP1 EAP apoptotic cells. The first one is shown in Figure 3.3.8.

Figure 3.3.8. AFM topographic image of an apoptotic HAP1 EAP cell (A). PTIR map of the cell at frequency 1650 cm^{-1} (amide I signal intensity) (B). PTIR map of the same cell at 965 cm^{-1} (nucleic acids signal intensity) (C). PTIR spectra of the am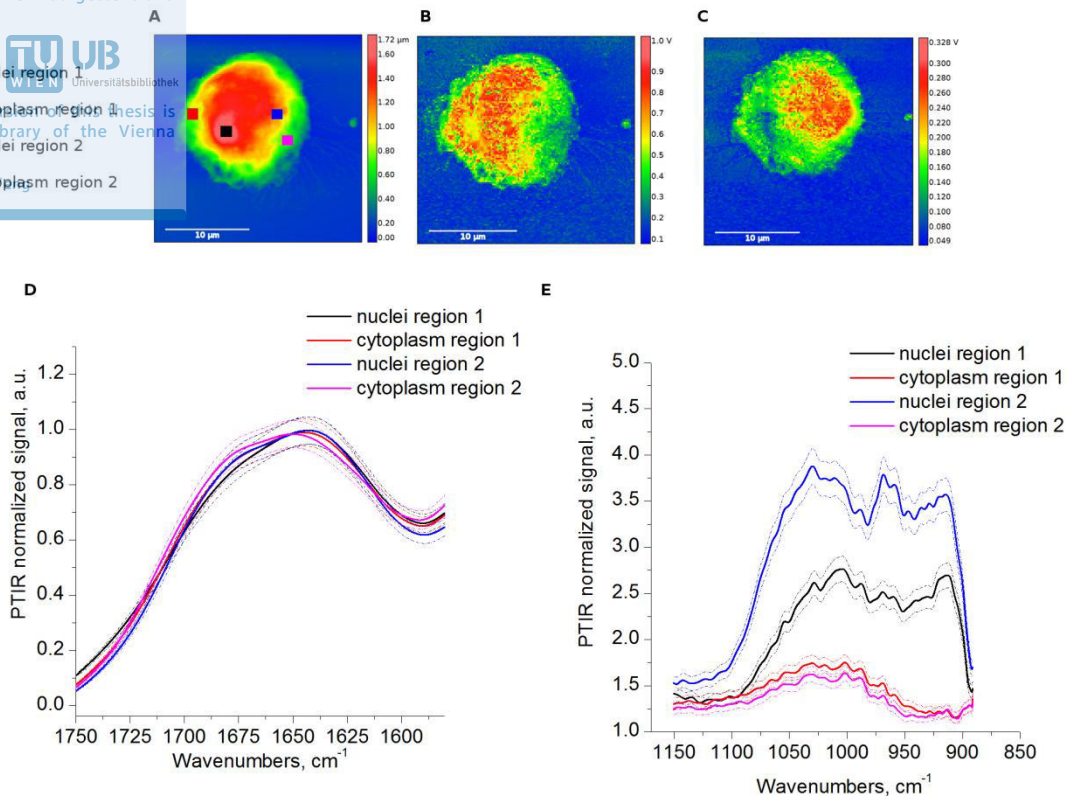ide I (D) and nucleic acids (E) bands acquired at different nuclei (black, blue) and cytoplasm (red, pink) regions. Dashed lines depict two standard deviations.

Apoptotic HAP1 EAP cells attributed to this type demonstrate a smooth topography (Figure 3.3.8 A) with the well defined nuclei region (a region with the largest topography signal). PTIR chemical imaging of proteins demonstrates an elevated signal in the nuclei region (Figure 3.3.8 B). The PITR map related to nucleic acids demonstrates a faded signal in a part of the nuclei region (Figure 3.3.8 C). We suppose that the decreased signal intensity of the nucleic acids band is caused by the local conformational changes in the nuclei (DNA condensation). Such conformational changes occur during apoptosis. The condensed nuclei has enormously increased concentration of nucleic acids, as a result, the nuclei becomes opaque to IR radiation. Thus, DNA condensation appears as a decrease in nucleic acids bands in IR spectra.[41] The band related to nucleic acids in the PTIR spectrum acquired at the region related to the presumed condensed nuclei (Figure 3.3.8 D, nuclei region 1) has almost disappeared. In the other nuclei region we observe a small nucleic acids band (Figure 3.3.9 D, nuclei region 2). We observe no notable differences in the position and the shape of the amide I band among PTIR spectra taken at different nuclei regions as well at the cytoplasm region (a region with the lower topography signal) (Figure 3.3.8 E).

Another type of apoptotic HAP1 EAP cells was found during the PTIR analysis (Figure 3.3.9).
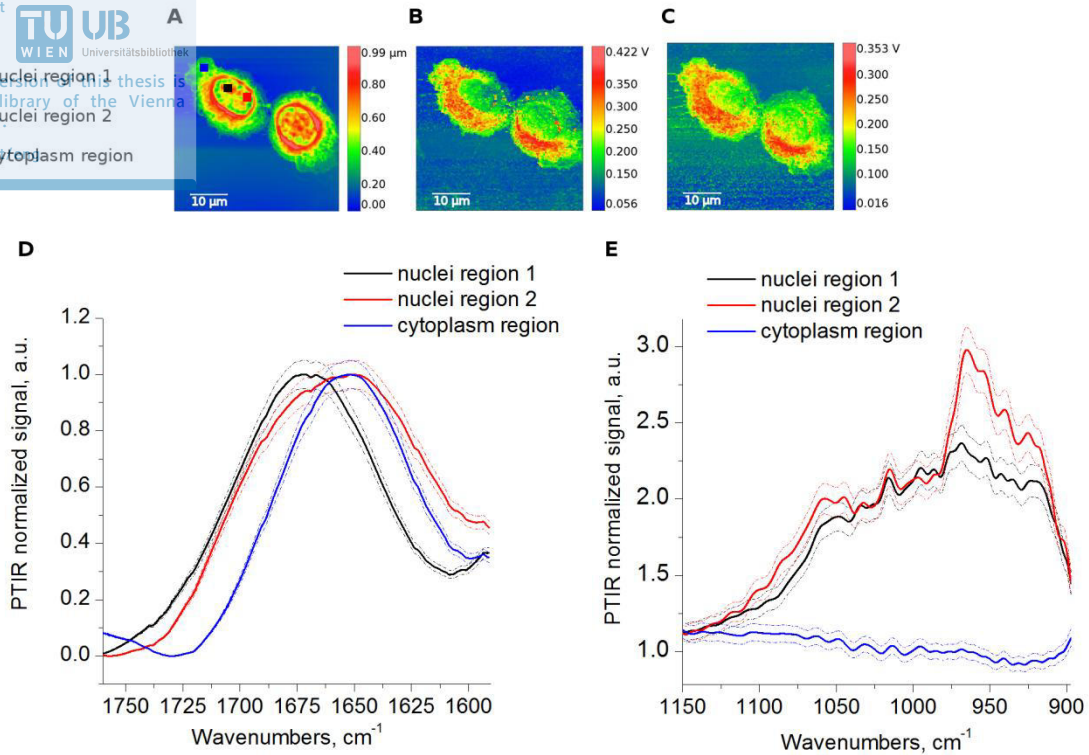
Figure 3.3.9. AFM topographic image of apoptotic HAP1 EAP cells (A). PTIR map of the cells at frequency 1650 cm^{-1} (amide I signal intensity) (B). PTIR map of the same cells at 1530 cm^{-1} (amide II signal intensity) (C). PTIR spectra of nuclei (black, red) and cytoplasm (blue) in amide I (D) and nucleic acids (E) spectral regions. Dashed lines depict two standard deviations.

Topographic image of the second type of apoptotic cells (Figure 3.3.9 A) shows distinct nucleic and cytoplasm regions. Inhomogeneous distribution within the nuclei region suggests that cells underwent alterations due to a later stage of apoptosis compared to the first type of cells. At a later stage of apoptosis generation of apoptotic bodies occurs[38,125].

Chemical images depicting protein distribution (Figures 3.3.9 B-C) demonstrate elevated PTIR signals in the cytoplasm region. PTIR spectra of the amide I band region were acquired at different cellular positions (Figure 3.3.9 E). Differences in the shape of the amide I band were observed primarily at the nuclei region and cytoplasm, suggesting different overall protein secondary structures within those regions. The intensity of the nucleic acid band appeared to be different within the different nuclei regions (Figure 3.3.9 D).

Further, we compare the amide I bands in PTIR spectra obtained for apoptotic and control cells (Figure 3.3.10).
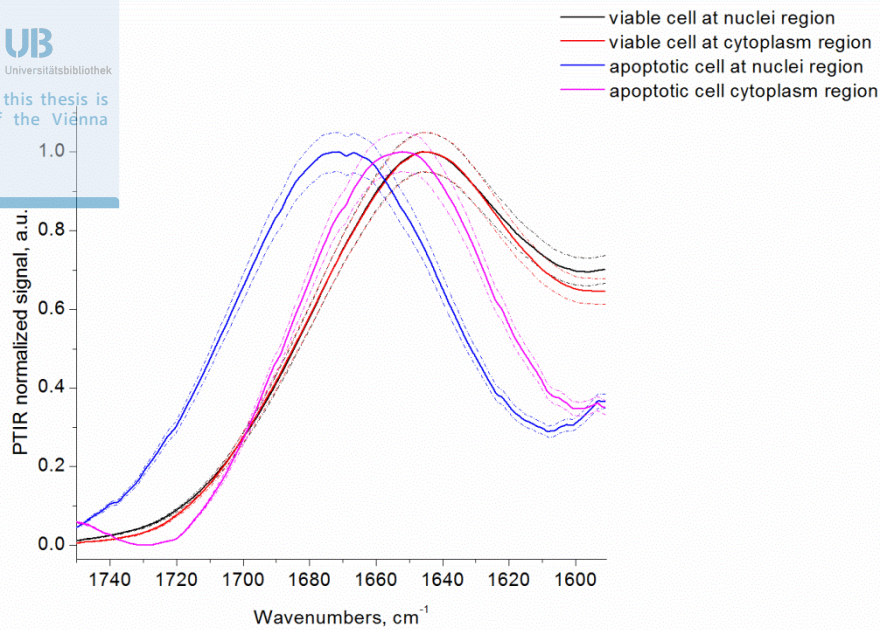
Figure 3.3.10. PTIR spectra of the amide I band of apoptotic and viable HAP1 EAP cells at cytoplasm and at nuclei regions. Dashed lines depict two standard deviations.

The position of the amide I band recorded in the nuclei region for apoptotic and control cells appeared to be different (1658 cm^{-1} and 1653 cm^{-1} respectively) suggesting that during apoptosis protein conformational changes primarily occur in the nuclei region.

So far publication of this work was not undertaken, as more and extended studies are required to confirm the observed results and drawn conclusions.

3.4. Combined multisensor imaging

Introduction to the publication II

FTIR-spectroscopic and LA-ICP-MS imaging for combined hyperspectral image analysis of tumor models

Anna Balbekova, Maximilian Bonta, Szilvia Torok, Johannes Ofner, Balazs Dome, Andreas Limbeck, Bernhard Lendl

In this paper we show that combination of chemical imaging techniques (FTIR and LA-ICP-MS) provides additional information which cannot be obtained by a single technique. The aim of this study is to show principles of combined (multisensor) analysis and to demonstrate that this analysis could deepen understanding of processes occuring in tumor samples. We analyze tumor thin sections with viable and dead tissue regions. The tumors were treated with anti-cancer agents (Cisplatin and Sunitinib). The efficacy of such a combined therapy normally investigated using routine methods (e.g. histological staining) that are time consuming and often not sensitive for discrimination of different stages of cellular death.

We measure each sample first by FTIR microscpectroscopy then by LA-ICP-MS. Using the software package ImageLab (Epina, Austria) we merge recorded datasets into one and perform multivariate analysis of the fused data. In particular, we implement the HCA of PCA method to find correlations in lateral distribution between analytes of interest. For each analyte we define a characteristic SPDC (e.g. peak intensity, peak are, peak ratio, etc). Then we replace the raw dataset with a set of SPDCs in order to simplify the multivariate dataset and minimize correlated variables[88].

We found two major correlations: the first is between protein secondary structure and platinum distribution (drug active element); and the second between a decay of physiologically relevant trace elements and changes in nuclear morphology. We found also that the degree of this correlation is related to a degree of tumor viability: strong correlations of IR and MS multisensor descriptors are related to a later apoptosis, whereas weak correlations indicated presence of both early and late apoptosis. According to this result the sample subjected to a longer drug therapy showed only late apoptotic regions, whereas the sample subjected to a shorter drug treatment delivered both early and late apoptotic regions. The results of the additionally performed univariate analysis (chemical imaging) and *k*-means clustering supported the results of combined analysis.

The results of the combined analysis point out different stages of cellular death occurring within the samples. Those results would not be possible to obtain using a single technique analysis.

Multisensor cluster analysis of tumor cross sections

The results of the Publication II showed that the combined analysis facilitate a deeper understanding of the processes undergoing within the drug treated tumors. In this sub-

chapter we provide cluster analysis of one of the samples analyzed previously (Publication II) to show that multivariate analysis of the combined datasets improves clustering of sample areas. In particular, we compare the performance of *k*-means clustering of the combined data (IR and MS) with clustering of the dataset containing only IR data.

We use optical microscopy and fluorescent staining to define apoptotic regions. Figure 3.4.1 shows a light microscopic image of the tumor cross section prepared for IR and MS measurements. Dead tissue appears as inhomogeneous dark structures. The fluorescent image of the adjacent thin section of the tumor stained for apoptotic cells is given in Figure 3.4.1 B.
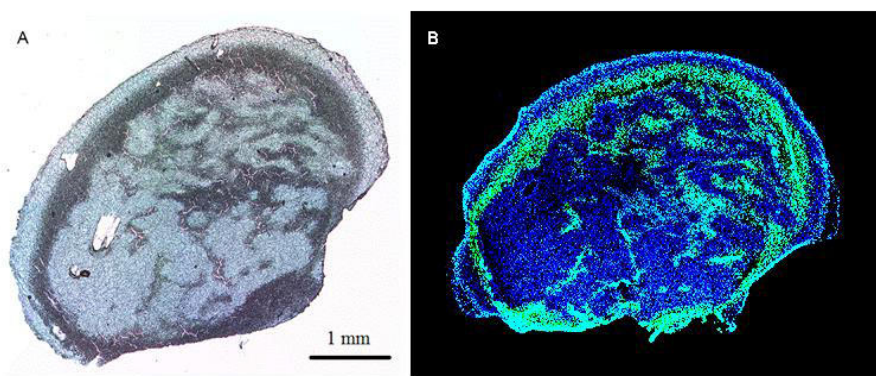

Figure 3.4.1. Optical microscopy image of the tumor tissue sections: (A) Image of the sample prepared for IR and MS measurements with a scale bar. (B) Terminal deoxynucleotidyl transferase dUTP Nick End Labelling (TUNEL) stained image of the adjacent section. Apoptotic cells (green) shown by TUNEL staining, counterstained with Hoechst 33342 (blue). Adapted from[126].

Staining revealed apoptotic areas (Figure 3.4.1 B, light green). They partially correlated with dark grey areas in the light microscopic image made from the thin-cut used for multisensor measurements (Figure 3.4.1 A). Differences in shape between those two specimens can be explained by shrinking of the tissue during the staining procedure.

In the combined cluster analysis we use the same list of SPDCs as defined in Publication II, thus, we apply the *k*-means algorithm to discriminate different tissue types within the tumor (viable and dead tissue). We perform *k*-means clustering of the fused and the IR data sets separately and compare the resulted images.

We use the Kaiser's criterion[79] to define the number of clusters that should be retained for analysis. For both datasets discrimination into three groups (clusters) was preformed, due to the fact that PCA revealed that the first three PCs showed eigenvalues larger than one. The clustered images are displayed as false-color maps and the color code was chosen to facilitate comparison of the two cluster images (Figure 3.4. 2A-B).

The red cluster appeared in both peripheral and central areas in the IR image (Figure 3.4.2 B), whereas in the combined image (Figure 3.4.2 A) the red cluster appeared mostly in the peripheral apoptotic areas and the green one predominantly in the central region. The blue cluster is assigned to the remaining tissue area in both images.

We attribute red and green clusters to apoptotic and the blue cluster to viable tissue. In the image of the fused data set one could observe a separation of the clusters allowing to distinguish between central and peripheral apoptotic tissue clusters (Figure 3.4.2 A). On the contrary, in the image deriving only from the IR data (Figure 3.4.2 B). The red cluster is present in both the central and the peripheral sample areas.

Average IR spectra assigned to each cluster in the fused and IR data sets are given in Figure 3.4.2 C-D. Figure 3.4.2 E-H demonstrate spectral fragments for each cluster related to the SPDCs 3 and 5.

The results of numerical evaluation of the descriptor for the phosphate ions (SPDC 5) are depicted in Figure 3.4.2 I-J. Here we analyzed the statistic significance of the spectral differences between the clusters.
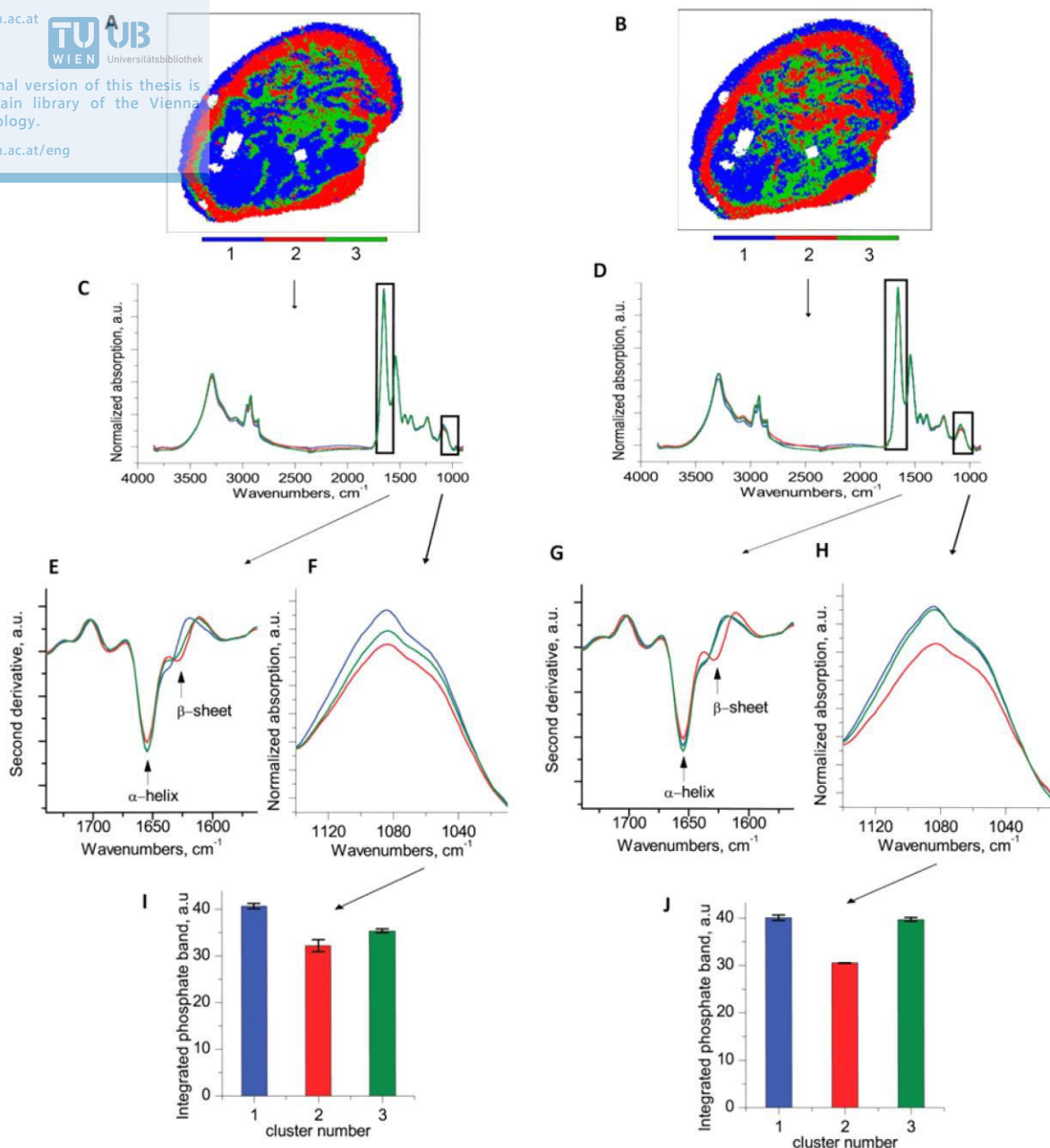
Figure 3.4.2. K-means clustered images resulting from fused IR and MS data (A) and IR data only (B). (C, D) Mean spectra of the clustered pixels. (E, G) Mean second derivative spectra of Amide I band. (F, H) Mean symmetric stretching phosphate band. (I, J) Integrated absorption of symmetric stretching phosphate band with its doubled standard deviation error bars. The colors of the graph bars, spectra and the clusters are correlating.

As an example, integrated band intensities of SPDC 5 (symmetrical stretch vibrations of phosphate) obtained from the mean spectra of the clusters in the combined dataset were compared with analogous ones in IR data set (Figure 3.4.2I-J). The degree of apoptosis can be quantified by the intensity of DNA related absorptions[53] which is reflected by this descriptor. The peripheral apoptotic area showed the lowest absorption for both data sets. The difference between viable and central apoptotic areas became pronounced in the cluster analysis performed on the combined data set, whereas clustering based on IR data

87

showed similar absorbance in viable (blue) and apoptotic (green central areas) tissues. We conclude that combined analysis facilitates more effective tumor viability discrimination. IR characterization of different stages of the apoptotic process in a tissue is difficult, since both the migration of phosphate ions at the later stages and the nuclear condensation at the earlier ones lead to decreased intensity in the phosphate band. This variation could be visualized using LA-ICP-MS as nuclear condensation does not produce a reduced concentration of phosphorus whereas migration of phosphate ions does.

According to the intensities of two apoptotic clusters obtained during classification of the combined dataset (Figure 3.4.2J), we attribute the peripheral cluster to a later stage of apoptosis as compared to the central cluster. This finding corresponds well with the above described interpretation of the LA-ICP-MS data. While IR imaging was able to detect all apoptotic areas, MS imaging detected only a part of it. We suggest that only the IR technique was sensitive to an earlier stage of apoptosis; changes to molecular structures can occur very fast while diffusion and active transport of metals are slower processes. A later stage of apoptosis was accessible by both IR and MS techniques.

Introduction to the publication III

Fourier transform infrared and laser ablation inductively coupled plasma-mass spectrometry imaging of cerebral ischemia: Combined analysis of rat brain thin cuts towards improved tissue classification

Anna Balbekova, Hans Lohninger, Geralda A. F. van Tilborg, Rick M. Dijkhuizen, Maximilian Bonta, Andreas Limbeck, Bernhard Lendl, Khalid A. Al-Saad, Mohamed Ali, Minja Celikic and Johannes Ofner

Publication III demonstrates that combined analysis facilitates an improved classification of post-stroke rat brain tissues. In this study we investigate rat brains which were recovered one week after induction of a photothrombotic stroke. Ischemic stroke is one of the leading disorders affecting people[56]. It is caused by reduction in blood flow to the brain.

The purpose of this study is to classify brain tissue types which are in close proximity to the stroke affected region. The consequences of post-stroke are primarily dependent on changes occurring in infarct zone (IZ) and peri-infarct zones (PIZ). The PIZ is initially not affected by stroke but can be subsequently altered and this can worsen recovery after stroke.[127,128] It is important to identify and understand biochemical mechanisms occurring in the PIZ because it would help to create treatment solutions. Investigation of white matter (WM) and gray matter (GM) tissues allows following brain plasticity (the ability to reorganize after the injury).

First, we image adjacent rat brains thin cuts with FTIR micro-spectroscopy and LA-ICP-MS. Then we fuse the acquired hyperspectral datacubes and perform multivariate classification analysis. We classify IZ, PIZ, WM and GM brain regions using a model based on either partial least squares discriminant analysis (PLS-DA) or random decision forest (RDF) algorithms.

PLS-DA and RDF classification results based on the combined dataset (IR+MS) demonstrated better predictions comparing to ones based on the individual datasets (IR or MS). RDF classification is more effective in predicting compared to PLS-DA classification.

Additionally, we calculate the importance and correlations of the variables (SPDCs). Correlations of the SPDCs describing both IR and MS data explained improved performance of the RDF model based on the combined dataset.

Further, we perform univariate chemical analysis of the variables that explain the underlying biological processes that facilitate an improved classification.

Finally, we apply the best classification models (among PLS-DA and RDF) to a new sample and compare classification results with the HE stained images. RDF model based on the combined datasets classifies more precisely compared to the models based on individual datasets (IR or MS). We conclude that multisensor hyperspectral imaging with subsequent RDF-based analysis improves analysis and therefore can deepen the understanding of biochemical processes occurring in ischemic brains.

Conclusions and outlook

Summary

During this doctoral project we employed near-field and far-field IR spectroscopic and imaging techniques to advance the existing state-of-the-art and to investigate the capabilities of those techniques when applied to biological samples.

In the first part of this dissertation, we suggested a method for time-resolved monitoring of changes in a bio-polymer thin film using a custom made PTIR system (see *publication I*).

- we demonstrated that the system is capable of fast time resolved measurements;
- for the first time the temporally-resolved near-field IR spectroscopic measurements were implemented and performed;
- we followed changes in secondary structure of a poly-L-lysine thin film by means of changes in band shape of the amide I band;
- we achieved an acquisition time about 15 s and suggested ways to shorten it significantly;
- our results demonstrate that the PTIR technique can be applied in a variety of applications in polymer and material science.

In the second part of this dissertation, we characterized and investigated the performance of the PTIR system regarding AFM tip stability during prolonged measurements of polymer and biological samples. This is of practical importance and has not been discussed in literature so far.

- We observed a "silicon band" related to the AFM tip in the PTIR spectra. We attribute this band to the tip contamination with PDMS (present in packaging materials).
- for the first time we performed prolonged measurements of a polymer and concluded that no significant tip degradation does occur during extensive measurements;
- we found that the AFM tip performance might get worse after several measurements of biological samples and proposed a method for AFM tip quality control;
- we suggested to use the $\delta_s(Si-CH_3)$ band (silicon band) at 1260 cm^{-1} to monitor the aging of a tip. With this method tip degradation can be evaluated *in situ* while measuring the PTIR spectra at the gold surface. A tip would be considered contaminated when the signal intensity of the silicon band is significantly reduced;
- we supported our findings with SEM and EDX spectroscopy. SEM visualized the contaminations at the AFM tips that showed the reduced PTIR sensitivity (reduced signal). EDX spectroscopy detected gold coating overall the tip, even at the very tip where contamination was observed.

In the third part of this dissertation, we studied various biological samples by PTIR spectroscopy and chemical imaging and discussed the advances which can be achieved using the PTIR system.

- we employed the quality control method which was proposed previously to follow the AFM tip degradation;

- we imaged individual *E. Coli* bacteria containing recombinant inclusion proteins (IBs) and analysed their secondary structure;

- we proposed a method for the quantitative analysis of the present IBs;

- we concluded that it is difficult to characterize the nucleic acids content in individual bacteria by our PTIR technique due to the low concentration of nucleic acids and the low laser power in the related spectral region;

- we studied a histological tumor section with dead and viable regions and found that the obtained results agreed well with the results of far-field IR microspectroscopy;

- we observed changes in protein secondary structure and reported nonlinear properties in the absorption of IR radiation by condensed nucleic acids;

- we characterized dead and viable individual mammalian cells. Two types of apoptotic cells were discriminated. Some cells have inhomogeneous morphology and different protein secondary structure at nuclei and cytoplasm regions. Other cells have homogeneous morphology and no notable difference in protein conformation. In both kinds of apoptotic cells the decay of the band related to the nucleic acids was observed. Viable (control) cells demonstrated homogeneous morphology. The protein secondary structure does not differ in nuclei and cytoplasm regions of those cells. The protein conformation in nuclei region for apoptotic and control cells were found to be different.

In the fourth part of this dissertation, we employed the multisensor approach to advance multivariate analysis of histological samples imaged with FTIR and LA-ICP-MS (see *publications II and III*).

- we characterized apoptotic regions in tumor thin sections;

- we found that the combined analysis improved the *k*-means clustering and found statistical correlations of the spatial distribution of chemical maps acquired using complementary techniques;

- we demonstrated that the combined analysis of tumor tissue allowed discrimination of different stages of apoptosis within a tumor tissue. Besides, combined analysis facilitated characterization of the different degrees of cellular death within different tumor thin sections. Those outcomes were not achieved during the analysis with single techniques;

- while studying a post-stroke brain tissues we demonstrated that combined image analysis improves the classification of different tissue types (white and gray matter, stroke region and its surroundings). We implemented different classification approaches and evaluated their classification performance. RDF classification appeared to me more precise than PLS-DA;

- we calculated the importance and correlations of the variables describing the combined dataset. Those correlations explained the improved performance of the RDF model on the combined dataset.

Outlook

In this work we have presented the capabilities and advances of IR spectroscopic imaging techniques employed to characterize biological samples. In this sub-chapter we point out the further developments which could be done, as well as possible practical limitations and challenges.

- In this work we used only beam-shaped AFM cantilevers, although triangular shaped AFM tips potentially would provide less torsional deflections. Thus, they might facilitate more stable PTIR measurements. The comparison of PTIR performance using rectangular and triangular AFM cantilevers was, to our knowledge, not reported so far.

- Although the proposed method of monitoring the AFM tip performance during the PTIR measurements worked for most of the tested AFM cantilevers, the initial intensity signal of δ_s(Si-CH$_3$) band at 1260 cm^{-1} might vary from cantilever to cantilever. Since the method basically detects a contamination that appears during the packaging and the amount of this contamination is not fixed. Furthermore, an experiment that verifies unambiguously that the observed "silicon band" can indeed be attributed to PDMS is still missing.

- As it was outlined in this work, AFM tips can be easily contaminated during the measurements of biological samples. Since the gold coating is not removed during the measurement (according to EDX spectroscopic analysis), contaminated ("not working") AFM tips can be cleaned and utilized for a second time. For that UV plasma cleaning or soaking in a solvent can be used to remove the contaminant. This option should be tested.

- When analyzing the PTIR chemical images, one could decide to divide (normalize) different chemical maps on each other (for example, protein map over the nucleic acids map). This procedure could become challenging if a small sample is being imaged for a long time (e.g. a bacterium), then chemical maps might be shifted. Thus, the straightforward division of the images would lead to an imprecise map. Thus, prior to the image division an image registration would be needed, in case images based on band ratios are calculated.

- Although FTIR microspectroscopy allows relatively fast imaging, to image histological samples (size 1-2 cm^2), it takes some time (8 hours). Frequently, the desired maximum spatial resolution would lead to a generation of a bulky data set (over 1 GB). Such large datasets often cannot be acquired due to limitations in the instruments software. The spectral pre-processing and analysis is also memory and time demanding. An interesting

option here are ne IR laser based imaging systems which are faster and can be operated to record images only at the desired SPDCs, thus also reducing the size of the recorded data.

- Another problem is that IR spectra of biological samples are frequently affected by Mie scattering [50] and resonance Mie-Scattering [129]. It often appears as a dip in the amide I region and leads to a shift of the protein band, thus suggesting wrong interpretation of the sample. However, frequently such spectra can be observed at the border between the tissue and the substrate and can be masked. Few approaches correcting Mie scattering and resonance Mie scattering were suggested. While Mie scattering can be reduced by Multiplicative Scatter Correction or Extended Multiplicative Scatter Correction algorithms available in chemometrical tools such as PLS toolbox (Mathworks), the correction of Resonant Mie scattering is rather complicated. The proposed method of spectra correction[130] uses a reference spectrum without scattering effects and works quite fine. However, it is worth to mention that this method has to be optimized when applied to the correction of hyperspectral datasets since it takes too long (weeks) when one wants to correct a standard dataset (around 183000 spectra) on a computer with 16 GB RAM, 64-bit operating system and a processor frequency of 3.4 GHz.

Bibliography

1. D. Naumann. "FT-INFRARED AND FT-RAMAN SPECTROSCOPY IN BIOMEDICAL RESEARCH". Appl. Spectrosc. Rev. 2001. 36(2–3): 239–298.

2. D. Naumann. Infrared Spectroscopy in Microbiology. Encyclopedia of Analytical Chemistry. 2006. 10.1002/9780470027318.a0117.

3. L. Baldassarre, V. Giliberti, A. Rosa, M. Ortolani, A. Bonamore, P. Baiocco, et al. "Mapping the amide I absorption in single bacteria and mammalian cells with resonant infrared nanospectroscopy." Nanotechnology. IOP Publishing, 2016. 27(7). 10.1088/0957-4484/27/7/075101.

4. V. Giliberti, L. Baldassarre, A. Rosa, V. de Turris, M. Ortolani, P. Calvani, et al. "Protein clustering in chemically stressed HeLa cells studied by infrared nanospectroscopy". Nanoscale. 2016. 8(40): 17560–17567. 10.1039/C6NR05783G.

5. Y.B. Monakhova, M. Hohmann, N. Christoph, H. Wachter, D.N. Rutledge. "Improved classification of fused data: Synergetic effect of partial least squares discriminant analysis (PLS-DA) and common components and specific weights analysis (CCSWA) combination as applied to tomato profiles (NMR, IR and IRMS)". Chemom. Intell. Lab. Syst. Elsevier B.V., 2016. 156: 1–6. 10.1016/j.chemolab.2016.05.006.

6. J. Ofner, K.A. Kamilli, E. Eitenberger, G. Friedbacher, B. Lendl, A. Held, et al. "Chemometric Analysis of Multisensor Hyperspectral Images of Precipitated Atmospheric Particulate Matter". Anal. Chem. 2015. 87(18): 9413–9420. 10.1021/acs.analchem.5b02272.

7. P.R. Griffiths, J. a. De Haseth. Fourier Transform Infrared Spectrometry. Second. John Wiley & Sons, Inc., Hoboken, New Jersey, 2006. 10.1002/047010631X.

8. B.H. Stuart. Infrared Spectroscopy: Fundamentals and Applications. Wiley-VCH, 2004.

9. U. Kubitscheck. Fluorescence Microscopy: From Principles to Biological Applications. U. Kubitscheck, editor. Wiley-Blackwell, 2013.

10. A. Schwaighofer, M. Brandstetter, B. Lendl. "Quantum cascade lasers (QCLs) in biomedical spectroscopy". Chem. Soc. Rev. Royal Society of Chemistry, 2017. 46: 5903–5924. 10.1039/C7CS00403F.

11. A. Dazzi, C. Policar. Biointerface Characterization By Advanced IR Spectroscopy. C.-M. Pradier, Y.J. Chabal, editors. AFM-IR : photothermal infrared nanospectroscopy. First Edit. Elsevier B.V., 2011. 10.1016/B978-0-444-53558-0/00009-6.

12. R. Hillenbrand, T. Taubner, F. Keilmann. "Phonon-enhanced light–matter interaction at the nanometre scale". Nature. 2002. 418(6894): 159–162. 10.1038/nature00899.

13. F. Huth, A. Govyadinov, S. Amarie, W. Nuansing, F. Keilmann, R. Hillenbrand. "Nano-FTIR Absorption Spectroscopy of Molecular Fingerprints at 20 nm Spatial Resolution." Nano Lett. 2012. 12(8): 3973–8. 10.1021/nl301159v.

14. A. V Zayats, I.I. Smolyaninov. "Near-field photonics : surface plasmon polaritons and localized surface plasmons". J. Opt. A. 2003. 16(5): 16–50.

15. G. Friedbacher, H. Bubert. Surface and Thin Film Analysis. G. Friedbacher, H. Bubert, editors. Second. Wiley-VCH Verlag & Co. KGaA, 2011.

16. R. Reifenberger. Fundamentals of Atomic Force Microscopy Part 1: Foundations. M. Lundstrom, S. Datta, editors. World Scientific Publishing Co. Pte. Ltd., 2016.

17. P. Eaton, P. West. "Atomic Force Microscopy". Oxford Univ. Press. 2010. 257. 10.1093/acprof:oso/9780199570454.001.0001.

18. G. Binnig, C.F. Quate. "Atomic Force Microscope". Phys. Rev. Lett. 1986. 56(9): 930–

933. 10.1103/PhysRevLett.56.930.

19. V. Mironov. Fundamentals of scanning probe microscopy. 2004.

20. U. Rabe, K. Janser, W. Arnold. "Vibrations of free and surface-coupled atomic force microscope cantilevers: Theory and experiment". Rev. Sci. Instrum. 1996. 67(9): 3281–3293. 10.1063/1.1147409.

21. F. Lu, M.A. Belkin. "Infrared absorption nano-spectroscopy using sample photoexpansion induced by tunable quantum cascade lasers". Opt. Express. 2011. 19(21): 1902–1904.

22. A. Dazzi, F. Glotin, R. Carminati. "Theory of infrared nanospectroscopy by photothermal induced resonance". J. Appl. Phys. 2010. 107(12). 10.1063/1.3429214.

23. F. Lu, M. Jin, M. a. Belkin. "Tip-enhanced infrared nanospectroscopy via molecular expansion force detection". Nat. Photonics. Nature Publishing Group, 2014. 8(January): 307–312. 10.1038/nphoton.2013.373.

24. S. V Kontomaris, A. Stylianou. "Atomic force microscopy for university students: applications in biomaterials". Eur. J. Phys. IOP Publishing, 2017. 38(3): 33003. 10.1088/1361-6404/aa5cd6.

25. H.Y.Z. Heng, X.C. Wang, Z.K. Wang. Advances in Laser Materials Processing: Technology, Research and Application. J. Lawrence, editor. 1st ed. Woodhead Publishing Limited, 2010. https://doi.org/10.1533/9781845699819.2.108.

26. N. Bloembergen. "Pulsed laser interactions with condensed matter". Mater. Res. Soc. Symp. Proc. 1985. 51: 3–13. 10.1557/PROC-51-3.

27. A. Dazzi, R. Prazeres, F. Glotin, J.M. Ortega. "Local infrared microspectroscopy with subwavelength spatial resolution with an atomic force microscope tip used as a photothermal sensor". Opt. Lett. OSA, 2005. 30(18): 2388. 10.1364/OL.30.002388.

28. A. Dazzi, R. Prazeres, F. Glotin, J. Ortega. "Subwavelength infrared spectromicroscopy using an AFM as a local absorption sensor". Infrared Phys. Technol. Elsevier, 2006. 49(1–2): 113–121.

29. A. Dazzi, R. Prazeres, F. Glotin, J.M. Ortega, M. Al-Sawaftah, M. de Frutos. "Chemical mapping of the distribution of viruses into infected bacteria with a photothermal method". Ultramicroscopy. 2008. 108(7): 635–41. 10.1016/j.ultramic.2007.10.008.

30. A. Dazzi, C.B. Prater. "AFM-IR: Technology and Applications in Nanoscale Infrared Spectroscopy and Chemical Imaging". Chem. Rev. 2016. acs.chemrev.6b00448. 10.1021/acs.chemrev.6b00448.

31. J.R. Felts, H. Cho, M.-F. Yu, L. a Bergman, A.F. Vakakis, W.P. King. "Atomic force microscope infrared spectroscopy on 15 nm scale polymer nanostructures." Rev. Sci. Instrum. 2013. 84(2): 23709. 10.1063/1.4793229.

32. M.B. Raschke, C. Lienau. "Apertureless near-field optical microscopy: Tip-sample coupling in elastic light scattering". Appl. Phys. Lett. 2003. 83(24): 5089–5091. 10.1063/1.1632023.

33. P. Verma. "Tip-Enhanced Raman Spectroscopy: Technique and Recent Advances". Chem. Rev. 2017. 117(9): 6447–6466. 10.1021/acs.chemrev.6b00821.

34. G. Ramer, F. Reisenbauer, B. Steindl, W. Tomischko, B. Lendl. "Implementation of Resonance Tracking for Assuring Reliability in Resonance Enhanced Photothermal Infrared Spectroscopy and Imaging". Appl. Spectrosc. 2017. 0(0): 370281769529. 10.1177/0003702817695290.

35. Ramer. "Development and Characterization of a Near-Field Infrared Microscope by the Coupling of AFM and QCL Spectroscopy". 2015.

36. Y. Tsujimoto. "Multiple ways to die: non-apoptotic forms of cell death." Acta Oncol.

2012. 51(3): 293–300. 10.3109/0284186X.2011.648340.

37. I. R. Indran, G. Tufo, S. Pervaiz, C. Brenner. "Recent advances in apoptosis, mitochondria and drug resistance in cancer cells". Biochim. Biophys. Acta - Bioenerg. Elsevier B.V., 2011. 1807(6): 735–745. 10.1016/j.bbabio.2011.03.010.

38. S. Elmore. "Apoptosis: A Review of Programmed Cell Death". Toxicol. Pathol. 2007. 35(4): 495–516. 10.1080/01926230701320337.

39. R.C. Taylor, S.P. Cullen, S.J. Martin. "Apoptosis : controlled demolition at the cellular level". 2008. 9(march). 10.1038/nrm2312.

40. M. Archana, T.L. Yogesh, K.L. Kumaraswamy. "Various methods available for detection of apoptotic cells--a review." Indian J. Cancer. 2013. 50(3): 274–83. 10.4103/0019-509X.118720.

41. U. Zelig, J. Kapelushnik, R. Moreh, S. Mordechai, I. Nathan. "Diagnosis of cell death by means of infrared spectroscopy". Biophys. J. Biophysical Society, 2009. 97(7): 2107–2114. 10.1016/j.bpj.2009.07.026.

42. A. Lamberti, C. Sanges, P. Arcari. "FT-IR spectromicroscopy of mammalian cell cultures during necrosis and apoptosis induced by drugs". J. Spectrosc. 2010. 24: 535–546. 10.3233/SPE-2010-0475.

43. E. Brauchle, S. Thude, S.Y. Brucker, K. Schenke-Layland. "Cell Death Stages in Single Apoptotic and Necrotic Cells Monitored by Raman Microspectroscopy". Sci. Rep. 2014. 4: 4698. 10.1038/srep04698.

44. C. Petibois, G. Deleris. "Chemical mapping of tumor progression by FT-IR imaging: towards molecular histopathology". Trends Biotechnol. 2006. 24(10): 455–462. 10.1016/j.tibtech.2006.08.005.

45. T. Yamada, N. Miyoshi, T. Ogawa, K. Akao, M. Fukuda, T. Ogasawara, et al. "Observation of Molecular Changes of a Necrotic Tissue from a Murine Carcinoma by Fourier-Transform". 2002. 8(6): 2010–2014.

46. L. Di Giambattista, D. Pozzi, P. Grimaldi, S. Gaudenzi, S. Morrone, A.C. Castellano. "New marker of tumor cell death revealed by ATR-FTIR spectroscopy". Anal. Bioanal. Chem. 2011. 399(8): 2771–2778. 10.1007/s00216-011-4654-7.

47. B.-B. Wu, Y.-P. Gong, X.-H. Wu, Y.-Y. Chen, F.-F. Chen, L.-T. Jin, et al. "Fourier transform infrared spectroscopy for the distinction of MCF-7 cells treated with different concentrations of 5-fluorouracil." J. Transl. Med. 2015. 13: 108. 10.1186/s12967-015-0468-2.

48. P. Plaimee, N. Weerapreeyakul, K. Thumanu, W. Tanthanuch, S. Barusrux. "Melatonin induces apoptosis through biomolecular changes, in SK-LU-1 human lung adenocarcinoma cells". Cell Prolif. 2014. 47(6): 564–577. 10.1111/cpr.12140.

49. A. Barth. "Infrared spectroscopy of proteins." Biochim. Biophys. Acta. 2007. 1767(9): 1073–101. 10.1016/j.bbabio.2007.06.004.

50. J. Bukowska, P. Piotrowski, M. Baranska. Optical Spectroscopy and Computational Methods in Biology and Medicine. 2014. 10.1007/978-94-007-7832-0.

51. Y. Gao, X. Huo, L. Dong, X. Sun, H. Sai, G. Wei, et al. "Fourier transform infrared microspectroscopy monitoring of 5-fluorouracil-induced apoptosis in SW620 colon cancer cells". Mol. Med. Rep. 2015. 11(4): 2585–2591. 10.3892/mmr.2014.3088.

52. B. Mohlenhoff, M. Romeo, M. Diem, B.R. Wood. "Mie-type scattering and non-Beer-Lambert absorption behavior of human cells in infrared microspectroscopy." Biophys. J. 2005. 88(5): 3635–3640. 10.1529/biophysj.104.057950.

53. K.Z. Liu, L. Jia, S.M. Kelsey, A.C. Newland, H.H. Mantsch. "Quantitative determination of apoptosis on leukemia cells by infrared spectroscopy". Apoptosis. 2001. 6(4): 269–

278. 10.1023/A:1011383408381.

54. N. Gault, J.-L. Lefaix. "Infrared microspectroscopic characteristics of radiation-induced apoptosis in human lymphocytes". Radiat. Res. 2003. 160(2): 238–250.

55. J. Zhou, Z. Wang, S. Sun, M. Liu, H. Zhang. "A rapid method for detecting conformational changes during differentiation and apoptosis of HL60 cells by Fourier-transform infrared spectroscopy." Biotechnol. Appl. Biochem. 2001. 33(Pt 2): 127–32. 10.1042/BA20000074.

56. G.A. Donnan, M. Fisher, M. Macleod, S.M. Davis. "Stroke". Lancet. 2008. 371(9624): 1612–23. 10.1016/S0140-6736(08)60694-7.

57. R.H. Quarles, W.B. Macklin, P. Morell. Basic Neurochemistry: molecular, cellular and medical aspects. G. Siegel, R. Albers, S. Brady, D. Price, editors. 7th ed. Academic Press Elsvier; New York, 2006.

58. S.T. Carmichael. "Cellular and molecular mechanisms of neural repair after stroke: Making waves". Ann. Neurol. 2006. 59(5): 735–742. 10.1002/ana.20845.

59. M. Zille, T.D. Farr, I. Przesdzing, J. Müller, C. Sommer, U. Dirnagl, et al. "Visualizing cell death in experimental focal cerebral ischemia: promises, problems, and perspectives." J. Cereb. Blood Flow Metab. 2012. 32(2): 213–31. 10.1038/jcbfm.2011.150.

60. P.R. Seevinck, L.H. Deddens, R.M. Dijkhuizen. "Magnetic resonance imaging of brain angiogenesis after stroke". Angiogenesis. 2010. 13(2): 101–111. 10.1007/s10456-010-9174-0.

61. R.M. Dijkhuizen, K. van der Marel, W.M. Otte, E.I. Hoff, J.P. van der Zijden, A. van der Toorn, et al. "Functional MRI and Diffusion Tensor Imaging of Brain Reorganization After Experimental Stroke". Transl. Stroke Res. 2012. 3(1): 36–43. 10.1007/s12975-011-0143-8.

62. S. Umesh Rudrapatna, T. Wieloch, K. Beirup, K. Ruscher, W. Mol, P. Yanev, et al. "Can diffusion kurtosis imaging improve the sensitivity and specificity of detecting microstructural alterations in brain tissue chronically after experimental stroke? Comparisons with diffusion tensor imaging and histology". Neuroimage. Elsevier Inc., 2014. 97: 363–373. 10.1016/j.neuroimage.2014.04.013.

63. M. van Meer, W.M. Otte, K. van der Marel, C.H. Nijboer, A. Kavelaars, J.W.B. van der Sprenkel, et al. "Extent of Bilateral Neuronal Network Reorganization and Functional Recovery in Relation to Stroke Severity". J. Neurosci. 2012. 32(13): 4495–4507. 10.1523/JNEUROSCI.3662-11.2012.

64. V. Labat-gest, S. Tomasi. "Photothrombotic ischemia: a minimally invasive and reproducible photochemical cortical lesion model for mouse stroke studies". J. Vis. Exp. 2013. 76(e50370): 1–6. 10.3791/50370.

65. O. Mărgăritescu, L. Mogoantă, I. Pirici, D. Pirici, D. Cernea, C. Mărgăritescu. "Histopathological changes in acute ischemic stroke." Rom. J. Morphol. Embryol. 2009. 50(3): 327–339.

66. S. Caine, M.J. Hackett, H. Hou, S. Kumar, J. Maley, Z. Ivanishvili, et al. "A novel multi-modal platform to image molecular and elemental alterations in ischemic stroke". Neurobiol. Dis. Elsevier Inc., 2016. 91: 132–142. 10.1016/j.nbd.2016.03.006.

67. M.J. Hackett, J. Lee, F. El-Assaad, J.A. McQuillan, E.A. Carter, G.E. Grau, et al. "FTIR imaging of brain tissue reveals crystalline creatine deposits are an ex vivo marker of localized ischemia during murine cerebral malaria: General implications for disease neurochemistry". ACS Chem. Neurosci. 2012. 3(12): 1017–1024. 10.1021/cn300093g.

68. M.J. Hackett, J.B. Aitken, F. El-Assaad, J. a McQuillan, E. a Carter, H.J. Ball, et al. "Mechanisms of murine cerebral malaria: Multimodal imaging of altered cerebral

metabolism and protein oxidation at hemorrhage sites." Sci. Adv. 2015. 1(11): e1500911. 10.1126/sciadv.1500911.

69. M.J. Hackett, C.J. Britz, P.G. Paterson, H. Nichol, I.J. Pickering, G.N. George. "In situ biospectroscopic investigation of rapid ischemic and postmortem induced biochemical alterations in the rat brain". ACS Chem. Neurosci. 2015. 6(2): 226–238. 10.1021/cn500157j.

70. M.J. Hackett, F. Borondics, D. Brown, C. Hirschmugl, S.E. Smith, P.G. Paterson, et al. "Subcellular Biochemical Investigation of Purkinje Neurons Using Synchrotron Radiation Fourier Transform Infrared Spectroscopic Imaging with a Focal Plane Array Detector BT - ACS Chemical Neuroscience". 2013.

71. M.Z. Kastyak, M. Szczerbowska-Boruchowska, D. Adamek, B. Tomik, M. Lankosz, K.M. Gough. "Pigmented creatine deposits in Amyotrophic Lateral Sclerosis central nervous system tissues identified by synchrotron Fourier Transform Infrared microspectroscopy and X-ray fluorescence spectromicroscopy". Neuroscience. Elsevier Inc., 2010. 166(4): 1119–1128. 10.1016/j.neuroscience.2010.01.017.

72. M.J. Hackett, S. Caine, X. Liu, T.E. May, F. Borondics. "Development of single-beam wide-field infrared imaging to study sub-cellular neuron biochemistry". Vib. Spectrosc. 2015. 77: 51–59. 10.1016/j.vibspec.2014.12.004.

73. M.J. Hackett, M. Desouza, S. Caine, B. Bewer, H. Nichol, P.G. Paterson, et al. "A new method to image heme-Fe, total Fe, and aggregated protein levels after intracerebral hemorrhage". ACS Chem. Neurosci. 2015. 6(5): 761–770. 10.1021/acschemneuro.5b00037.

74. D. Ehgartner, P. Sagmeister, T. Langemann, A. Meitz, W. Lubitz, C. Herwig. "A novel method to recover inclusion body protein from recombinant E. coli fed-batch processes based on phage ΦX174-derived lysis protein E". Appl. Microbiol. Biotechnol. Applied Microbiology and Biotechnology, 2017. 101(14): 5603–5614. 10.1007/s00253-017-8281-x.

75. F. Rueda, O. Cano-Garrido, U. Mamat, K. Wilke, J. Seras-Franzoso, E. Garcia-Fruitos, et al. "Production of functional inclusion bodies in endotoxin-free Escherichia coli". Appl. Microbiol. Biotechnol. 2014. 98(22): 9229–9238. 10.1007/s00253-014-6008-9.

76. U. Rinas, E. Garcia-Fruitos, J.L. Corchero, E. Vazquez, J. Seras-Franzoso, A. Villaverde. "Bacterial Inclusion Bodies: Discovering Their Better Half". Trends Biochem. Sci. Elsevier Ltd, 2017. 42(9): 726–737. 10.1016/j.tibs.2017.01.005.

77. D. Ami, L. Bonecchi, S. Calì, G. Orsini, G. Tonon, S.M. Doglia. "FT-IR study of heterologous protein expression in recombinant Escherichia coli strains". Biochim. Biophys. Acta - Gen. Subj. 2003. 1624(1–3): 6–10. 10.1016/j.bbagen.2003.09.008.

78. L.M. Miller, M.W. Bourassa, R.J. Smith. "FTIR spectroscopic imaging of protein aggregation in living cells." Biochim. Biophys. Acta. Elsevier B.V., 2013. 1828(10): 2339–46. 10.1016/j.bbamem.2013.01.014.

79. H.F. Kaiser. "The application of electronic computers to factor analysis". Measurement. 1960. XX(1): 141–151.

80. I.T. Jolliffe. Principal Component Analysis, Second Edition. Encyclopedia of Statistics in Behavioral Science. 2002. 10.2307/1270093.

81. P. Lasch, W. Haensch, D. Naumann, M. Diem. "Imaging of colorectal adenocarcinoma using FT-IR microspectroscopy and cluster analysis". Biochim. Biophys. Acta - Mol. Basis Dis. 2004. 1688(2): 176–186. 10.1016/j.bbadis.2003.12.006.

82. P.-N. Tan, M. Steinbach, V. Kumar. Introduction to Data Mining. First Edit. Addison-Wesley Longman Publishing Co., Inc., Boston, MA, USA, 2005.

83. D. Steinley. "K-means clustering: a half-century synthesis". Br. J. Math. Stat. Psychol. 2006. 59(Pt 1): 1–34. 10.1348/000711005X48266.

84. J. Macqueen. "Some methods for classification and analysis of multivariate observations". Proc. Fifth Berkeley Symp. Math. Stat. Probab. 1967. 1(233): 281–297. citeulike-article-id:6083430.

85. R.G. Brereton, G.R. Lloyd. "Partial least squares discriminant analysis : taking the magic away". J. Chemom. 2014. (28): 213–225. 10.1002/cem.2609.

86. A. Pinto, S. Pereira, H. Dinis, C.A. Silva, D.M.L.D. Rasteiro. "Random decision forests for automatic brain tumor segmentation on multi-modal MRI images". Proc. - 2015 IEEE 4th Port. Meet. Bioeng. ENBENG 2015. 2015. 10.1109/ENBENG.2015.7088842.

87. N. Vogler, S. Heuke, T.W. Bocklitz, M. Schmitt, J. Popp. "Multimodal Imaging Spectroscopy of Tissue." Annu. Rev. Anal. Chem. (Palo Alto. Calif). 2015. 8(May): 359–87. 10.1146/annurev-anchem-071114-040352.

88. H. Lohninger, J. Ofner. "Multisensor hyperspectral imaging as a versatile tool for image-based chemical structure determination". Spectrosc. Eur. 2014. 26(5): 6–10.

89. D. Perez-Guaita, K. Kochan, M. Martin, D.W. Andrew, P. Heraud, J.S. Richards, et al. "Multimodal vibrational imaging of cells". Vib. Spectrosc. 2017. 91: 46–58. 10.1016/j.vibspec.2016.07.017.

90. A. Balbekova, H. Lohninger, G.A.F. van Tilborg, R.M. Dijkhuizen, M. Bonta, A. Limbeck, et al. "Fourier Transform Infrared (FT-IR) and Laser Ablation Inductively Coupled Plasma – Mass Spectrometry (LA-ICP-MS) Imaging of Cerebral Ischemia: Combined Analysis of Rat Brain Thin Cuts Toward Improved Tissue Classification". Appl. Spectrosc. 2017. (1): 1–21. 10.1177/0003702817734618.

91. R. Bhargava. "Towards a practical Fourier transform infrared chemical imaging protocol for cancer histopathology." Anal. Bioanal. Chem. 2007. 389(4): 1155–69. 10.1007/s00216-007-1511-9.

92. K.L. Andrew Chan, S.G. Kazarian. "Attenuated total reflection Fourier-transform infrared (ATR-FTIR) imaging of tissues and live cells". Chem. Soc. Rev. Royal Society of Chemistry, 2015. 45: 1850–1864. 10.1039/C5CS00515A.

93. J.D. Pallua, W. Recheis, R. Pöder, K. Pfaller, C. Pezzei, H. Hahn, et al. "Morphological and tissue characterization of the medicinal fungus Hericium coralloides by a structural and molecular imaging platform". Analyst. 2012. 137(7): 1584–1595. 10.1039/C1AN15615B.

94. J. Kneipp, P. Lasch, E. Baldauf, M. Beekes, D. Naumann. "Detection of pathological molecular alterations in scrapie-infected hamster brain by Fourier transform infrared (FT-IR) spectroscopy". Biochim. Biophys. Acta - Mol. Basis Dis. 2000. 1501(2–3): 189–199. 10.1016/S0925-4439(00)00021-1.

95. V. Sablinskas, V. Urboniene, J. Ceponkus, A. Laurinavicius, D. Dasevicius, F. Jankevicius, et al. "Infrared spectroscopic imaging of renal tumor tissue". J. Biomed. Opt. 2011. 16(9): 96006. 10.1117/1.3622292.

96. C. Krafft, S.B. Sobottka, K.D. Geiger, G. Schackert, R. Salzer. "Classification of malignant gliomas by infrared spectroscopic imaging and linear discriminant analysis". Anal. Bioanal. Chem. 2007. 387(5): 1669–1677. 10.1007/s00216-006-0892-5.

97. K. Wehbe, R. Pineau, S. Eimer, A. Vital, H. Loiseau, G. Déléris. "Differentiation between normal and tumor vasculature of animal and human glioma by FTIR imaging". Analyst. 2010. 135(12): 3052. 10.1039/c0an00513d.

98. N. Bergner, B.F.M. Romeike, R. Reichart, R. Kalff, C. Krafft, J. Popp. "Tumor margin identification and prediction of the primary tumor from brain metastases using FTIR

imaging and support vector machines". Analyst. 2013. 138(14): 3983. 10.1039/c3an00326d.

99. N. Amharref, A. Beljebbar, S. Dukic, L. Venteo, L. Schneider, M. Pluot, et al. "Brain tissue characterisation by infrared imaging in a rat glioma model." Biochim. Biophys. Acta. 2006. 1758(7): 892–899. 10.1016/j.bbamem.2006.05.003.

100. R. Noreen, C.C. Chien, M. Delugin, S. Yao, R. Pineau, Y. Hwu, et al. "Detection of collagens in brain tumors based on FTIR imaging and chemometrics". Anal. Bioanal. Chem. 2011. 401(3): 845–852. 10.1007/s00216-011-4899-1.

101. H. D'inca, J. Namur, S.H. Ghegediban, M. Wassef, F. Pascale, A. Laurent, et al. "Automated Quantification of Tumor Viability in a Rabbit Liver Tumor Model after Chemoembolization Using Infrared Imaging." Am. J. Pathol. American Society for Investigative Pathology, 2015. 185(7): 1877–1888. 10.1016/j.ajpath.2015.03.023.

102. E. Gazi, J. Dwyer, N. Lockyer, P. Gardner, J.C. Vickerman, J. Miyan, et al. "The combined application of FTIR microspectroscopy and ToF-SIMS imaging in the study of prostate cancer." Faraday Discuss. 2004. 126: 41–59. 10.1039/b304883g.

103. N. Wald, N. Bordry, P.G. Foukas, D.E. Speiser, E. Goormaghtigh. "Identification of melanoma cells and lymphocyte subpopulations in lymph node metastases by FTIR imaging histopathology". Biochim. Biophys. Acta - Mol. Basis Dis. 2016. 1862(2): 202–212. 10.1016/j.bbadis.2015.11.008.

104. I. Amenabar, S. Poly, W. Nuansing, E.H. Hubrich, A.A. Govyadinov, F. Huth, et al. "Structural analysis and mapping of individual protein complexes by infrared nanospectroscopy." Nat. Commun. Nature Publishing Group, 2013. 4: 2890. 10.1038/ncomms3890.

105. F.S. Ruggeri, G. Longo, S. Faggiano, E. Lipiec, a Pastore, G. Dietler. "Infrared nanospectroscopy characterization of oligomeric and fibrillar aggregates during amyloid formation." Nat. Commun. Nature Publishing Group, 2015. 6: 7831. 10.1038/ncomms8831.

106. F.S. Ruggeri, S. Vieweg, U. Cendrowska, G. Longo, A. Chiki, H.A. Lashuel, et al. "Nanoscale studies link amyloid maturity with polyglutamine diseases onset". Sci. Rep. Nature Publishing Group, 2016. 6(1): 31155. 10.1038/srep31155.

107. M. Jin, F. Lu, M.A. Belkin. "High-sensitivity infrared vibrational nanospectroscopy in water". Nat. Publ. Gr. Nature Publishing Group, 2017. (May). 10.1038/lsa.2017.96.

108. S. Berweger, D.M. Nguyen, E.A. Muller, H.A. Bechtel, T.T. Perkins, M.B. Raschke. "Nano-Chemical Infrared Imaging of Membrane Proteins in Lipid Bilayers". 2013. 18292–18295.

109. E. Kennedy, R. Al-Majmaie, M. Al-Rubeai, D. Zerulla, J.H. Rice. "Quantifying nanoscale biochemical heterogeneity in human epithelial cancer cells using combined AFM and PTIR absorption nanoimaging." J. Biophotonics. 2015. 8(1–2): 133–41. 10.1002/jbio.201300138.

110. I. Amenabar, S. Poly, M. Goikoetxea, W. Nuansing, P. Lasch, R. Hillenbrand. "Hyperspectral infrared nanoimaging of organic samples based on Fourier transform infrared nanospectroscopy". Nat. Commun. 2017. 8: 14402. 10.1038/ncomms14402.

111. D. Perez-Guaita, K. Kochan, M. Martin, D.W. Andrew, P. Heraud, J.S. Richards, et al. "Multimodal vibrational imaging of cells". Vib. Spectrosc. Elsevier B.V., 2016. 91(July 2017): 46–58. 10.1016/j.vibspec.2016.07.017.

112. P. Lasch, I. Noda. "Two-Dimensional Correlation Spectroscopy for Multimodal Analysis of FT-IR, Raman, and MALDI-TOF MS Hyperspectral Images with Hamster Brain Tissue". Anal. Chem. 2017. 89: 5008–5016. 10.1021/acs.analchem.7b00332.

113. J. Ofner, F. Brenner, K. Wieland, E. Eitenberger, C. Eisenmenger-sittner, S. Török, et al. "Image-Based Chemical Structure Determination". Sci. Rep. 2017. 7(June): 1–11. 10.1038/s41598-017-07041-x.

114. B. Eggenreich, M. Willim, D.J. Wurm, C. Herwig, O. Spadiut. "Production strategies for active heme-containing peroxidases from E. coli inclusion bodies - A review". Biotechnol. Reports. Elsevier B.V., 2016. 10: 75–83. 10.1016/j.btre.2016.03.005.

115. M.H.M. Ali, K. Al-saad, A. Popelka, G. Van Tilborg. "Application of Fourier Transform Infrared (FTIR) Spectroscopy and Atomic Force Microscopy in Stroke- Affected Brain Tissue ." J. Med. Med. Sci. 2016. 2(2): 11–24.

116. G. Ramer, A. Balbekova, A. Schwaighofer, B. Lendl. "Method for time-resolved monitoring of a solid state biological film using photothermal infrared nanoscopy on the example of poly-L-lysine". Anal. Chem. 2015. 87(8): 4415–4420. 10.1021/acs.analchem.5b00241.

117. M. Bonta, B. Hegedus, A. Limbeck. "Application of dried-droplets deposited on pre-cut filter paper disks for quantitative LA-ICP-MS imaging of biologically relevant minor and trace elements in tissue samples". Anal. Chim. Acta. Elsevier Ltd, 2016. 908: 54–62. 10.1016/j.aca.2015.12.048.

118. Y.S. Lo, N.D. Huefner, W.S. Chan, P. Dryden, B. Hagenhoff, T.P. Beebe. "Organic and inorganic contamination on commercial AFM cantilevers". Langmuir. 1999. 15(19): 6522–6526. 10.1021/la990371x.

119. Stephen G. Lipson, L. Henry, S. David. Optical Physics. Cambridge University Press, 1995.

120. A. Lehmann, L. Schumann, K. Hubner. "Optical Phonons in Amorphous Silicon Oxides". Phys. Status Solidi. 1983. 117(I): 689. 10.1002/pssb.2221170231.

121. V.G. Kravets, C. Meier, D. Konjhodzic, A. Lorke, H. Wiggers. "Infrared properties of silicon nanoparticles". J. Appl. Phys. 2005. 97(8): 1–5. 10.1063/1.1866475.

122. A. Dazzi. "Theoretical study of an absorbing sample in infrared near-field spectromicroscopy". Opt. Commun. 2004. 235(4–6): 351–360. 10.1016/j.optcom.2004.02.084.

123. C. Saulou, F. Jamme, L. Girbal, C. Maranges, I. Fourquaux, M. Cocaign-Bousquet, et al. "Synchrotron FTIR microspectroscopy of Escherichia coli at single-cell scale under silver-induced stress conditions". Anal. Bioanal. Chem. 2013. 405(8): 2685–2697. 10.1007/s00216-013-6725-4.

124. C. Sandt, C. Madoulet, A. Kohler, P. Allouch, C. De Champs, M. Manfait, et al. "FT-IR microspectroscopy for early identification of some clinically relevant pathogens". J. Appl. Microbiol. 2006. 101(4): 785–797. 10.1111/j.1365-2672.2006.02969.x.

125. M.M. Quiroz, G. Khanal, D. Pappas. "Apoptosis (Programed Cell Death) Studied by Fluorescence Spectroscopy". Encycl. Anal. Chem. 2000. 1–15. 10.1002/9780470027318.a9351.

126. A. Balbekova, M. Bonta, S. Török, J. Ofner, A. Limbeck, B. Lendl. "FTIR-spectroscopic and LA-ICP-MS imaging for combined hyperspectral image analysis of tumor models". Anal. Methods. 2017. 9: 5464–5471. 10.1039/C7AY01369H.

127. D. Katsman, J. Zheng, K. Spinelli, S.T. Carmichael. "Tissue Microenvironments Within Functional Cortical Subdivisions Adjacent to Focal Stroke". J. Cereb. Blood Flow Metab. 2003. 997–1009. 10.1097/01.WCB.0000084252.20114.BE.

128. P. Lipton. "Ischemic cell death in brain neurons." Physiol. Rev. 1999. 79(4): 1431–1568. 10.1016/j.shpsa.2008.02.001.

129. P. Bassan, A. Sachdeva, A. Kohler, C. Hughes, A. Henderson, J. Boyle, et al. "FTIR

microscopy of biological cells and tissue: data analysis using resonant Mie scattering (RMieS) EMSC algorithm." Analyst. 2012. 137(6): 1370–7. 10.1039/c2an16088a.

130. P. Bassan, A. Kohler, H. Martens, J. Lee, H.J. Byrne, P. Dumas, et al. "Resonant Mie scattering (RMieS) correction of infrared spectra from highly scattering biological samples." Analyst. 2010. 135(2): 268–77. 10.1039/b921056c.

Publications

Publication I

"Method for Time-Resolved Monitoring of a Solid State Biological Film Using Photothermal Infrared Nanoscopy on the Example of Poly-L-lysine"

G. Ramer, A. Balbekova, A. Schwaighofer, B. Lendl.

ABSTRACT: We report time-resolved photothermal infrared nanoscopy measurements across a spectral range of more than 100 cm^{-1} (1565 cm^{-1} to 1729 cm^{-1}) at nanoscale spatial resolution. This is achieved through a custom-built system using broadly tunable external cavity quantum cascade lasers in combination with a commercially available atomic force microscope. The new system is applied to the analysis of conformational changes of a polypeptide (poly-L-lysine) film upon temperature-induced changes of the humidity in the film. Changes of the secondary structure from β-sheet to α-helix could be monitored at a time resolution of 15 s per spectrum. The time-resolved spectra are well comparable to reference measurements acquired with conventional Fourier transform infrared microscopy.

Publication II

"FTIR-spectroscopic and LA-ICP-MS Imaging for Combined Hyperspectral Image Analysis of Tumor Models"

A. Balbekova, M. Bonta, S. Török, J. Ofner, B. Döme, A. Limbeck and B. Lendl.

ABSTRACT: Modern chemical imaging techniques provide spatially resolved information on the molecular and elemental composition of samples with both high spatial and spectral resolution. Over the past few decades these techniques, in particular, Fourier transform infrared (FTIR) spectroscopy and laser ablation inductively coupled plasma mass spectrometry (LA-ICP-MS) have been successfully applied in histopathological research. This work demonstrates that the multivariate analysis of combined FTIR and LA-ICP-MS microscopy hyperspectral images can bring additional knowledge to biomedical research. The concept of such analysis was demonstrated while investigating two different tumor samples subjected to anticancer therapy. Combined analysis has revealed a correlation between the lateral distribution of analytes and sample properties within the different techniques. Correlations between alterations in the average protein secondary structure and platinum distribution were found, as well as between changes in the cell nuclear morphology and a reduction of physiologically relevant trace elements. The results of combined analysis suggested different degrees of tumor viability. Univariate analysis and k-

means clustering successfully discriminated dead tumor regions and supported the results of combined analysis.

Publication III

"Fourier Transform Infrared and Laser Ablation Inductively Coupled Plasma Mass Spectrometry Imaging of Cerebral Ischemia: Combined Analysis of Rat Brain Thin Cuts Towards Improved Tissue Classification"

A. Balbekova, H. Lohninger, G. Tilborg, R. Dijkhuizen, M. Bonta, A. Limbeck, B. Lendl, K. Al-Saad, M. Ali, M. Celikic, J. Ofner

ABSTRACT: Microspectroscopic techniques are widely used to complement histological studies. Due to recent developments in the field of chemical imaging, combined chemical analysis has become attractive. This technique facilitates a deepened analysis compared to single techniques or side-by-side analysis. In this study, rat brains harvested one week after induction of photothrombotic stroke were investigated. Adjacent thin cuts from rats' brains were imaged using Fourier transform infrared (FT-IR) microspectroscopy and laser ablation inductively coupled plasma mass spectrometry (LA-ICP-MS). The LA-ICP-MS datawere normalized using an internal standard (a thin gold layer). The acquired hyperspectral data cubes were fused and subjected to multivariate analysis. Brain regions affected by stroke as well as unaffected gray and white matter were identified and classified using a model based on either partial least squares discriminant analysis (PLS-DA) or random decision forest (RDF) algorithms. The RDF algorithm demonstrated the best results for classification. Improved classifi- cation was observed in the case of fused data in comparison to individual data sets (either FT-IR or LA-ICP-MS). Variable importance analysis demonstrated that both molecular and elemental content contribute to the improved RDF classifi- cation. Univariate spectral analysis identified biochemical properties of the assigned tissue types. Classification of multi-sensor hyperspectral data sets using an RDF algorithm allows access to a novel and in-depth understanding of biochemical processes and solid chemical allocation of different brain regions.

Here we provide the results of the quality control spectra acquired at a clean gold substrate before and after each chemical mapping.
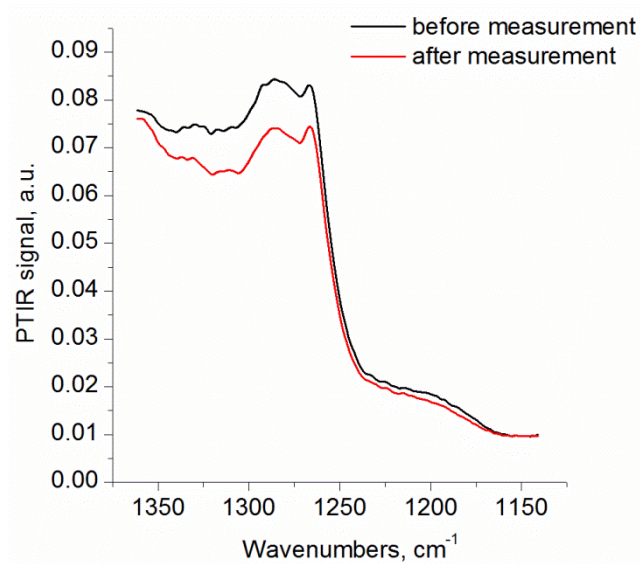

Figure A1. PTIR spectra of a clean gold substrate recorded before and after PTIR measurements of *E. Coli* bacterium control (A) and with IBs (B).
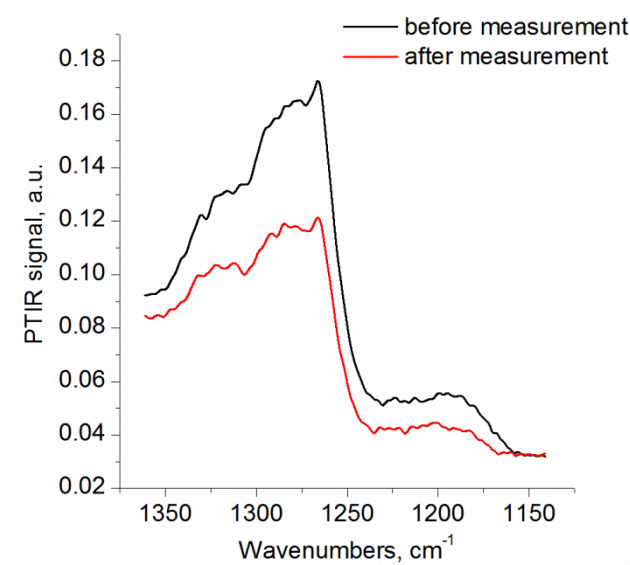

Figure A2. PTIR spectra of a clean gold substrate recorded before and after PTIR measurements of a control HAP1 EAP cell.
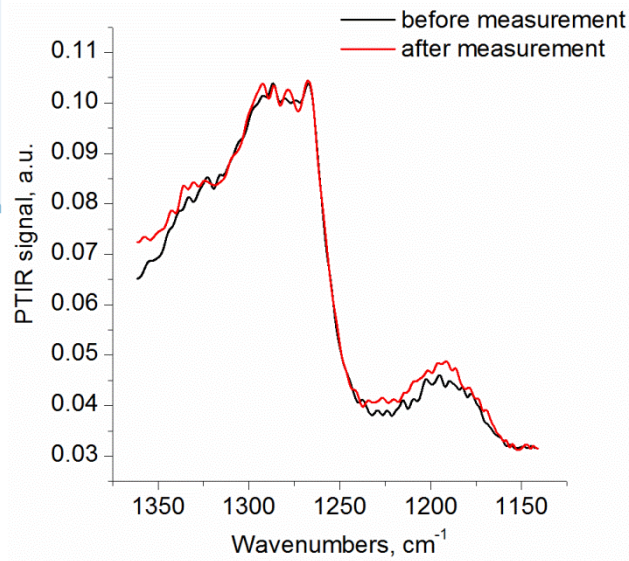
Figure A3. PTIR spectra of a clean gold substrate recorded before and after PTIR measurements of an apoptotic HAP1 EAP cell.
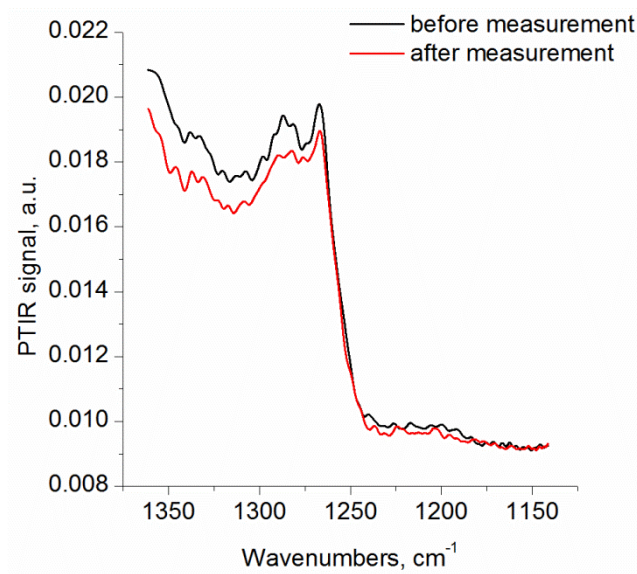

Figure A4. PTIR spectra of a clean gold substrate recorded before and after PTIR measurements of an apoptotic HAP1 EAP cell.